Master Thesis

A semi-anthropomorphic photoacoustic breast phantom

Rianne van Dommelen

University of Twente

Biomedical Photonic Imaging Group

Exam committee

Prof. Dr. S. Manohar

M. Dantuma, MSc.

Prof. Dr. Ir. C.L. de Korte

Dr. Ir. F.J. Siepel

11 July 2018

UNIVERSITY OF TWENTE.

BMPI Biomedical Photonic Imaging

Summary:

Anthropomorphic breast phantoms are needed to validate and improve photoacoustic imaging systems for breast cancer detection. A first step to achieve this is by fabricating a semi-anthropomorphic photoaoustic breast phantom, having less complex than but comparable structures to tissue. In order to do this, first the acoustic and optical properties of the breast tissues fat, fibroglandular, skin and blood vessels were obtained from literature. Then an inventarisation of available materials and fabrication techniques to mimic these tissue types was done. By scoring these available materials on a set of requirements, three candidate materials for mimicking breast tissue were remaining. These materials were acoustically characterised, which resulted in custom poly (vinyl chloride) plastisol (PVCP) to be most suitable as phantom material for this application.

The breast phantom was developed using 3D printed moulds. The phantom consists of a silicone skin outer layer, a fat layer and a fibroglandular region in the center. The irregular boundary between fat and fibroglandular tissue mimicking materials (TMM) is based on a 3D model of a cauliflower. Two tumors and a blood vessel were inserted in the phantom. Fat, fibroglandular and tumor/blood TMM were all fabricated using different compositions of PVCP, the basis of which consists of the plasticizers di(2-ethylhexyl) adipate (DEHA) and benzyl butyl phthalate (BBP), calcium-zinc heat stabilizer and PVC resin. Additives to induce acoustic speckle, optical scattering and optical absorption are glass beads, titanium oxide (TiO_2) and black plastic colouring (BPC), respectively.

An adapted insertion technique was used for acoustic characterisation of the phantom materials. The speed of sound (SoS) values of fat, fibroglandular and blood TMM are respectively 1447, 1511 and 1511 m/s. Power law fits of acoustic attenuation (AA) are resulting in 0.42, 0.55 and 0.90 dB/cm at 1 MHz for these materials. Acoustic impedances of the three tissue types are 1.24, 1.61 and 1.82 MRayls. The fat and fibroglandular TMMs both have fully developed acoustic speckle. The inverse adding doubling (IAD) method was used to obtain the optical absorption (μ_a) and reduced scattering coefficients (μ_s') of all four tissue types at 785 nm. This results in values for μ_a of 2.75, 1.60, 7.11 and 0.39 cm^{-1} for fat, fibroglandular, blood and skin respectively. For these tissue types μ_s' is 0.1, 10.9, 0 and 84.7 cm^{-1}.

Magnetic resonance imaging (MRI), ultrasound (US) B-mode imaging and photoacoustic tomography (PAT) were used to validate the phantom. The boundary between fat and fibroglandular tissue is found in both MRI and US images. Absorbing structures can be seen with all imaging modalities. The acoustic properties of the PVCP materials were well tuned to tissue literature values, resulting in US images comparable to real tissue images. The optical properties of skin and fat were not well tuned for tissue values. μ_s' of skin is higher than tissue values, while μ_a of skin is lower at 785 nm and is therefore not showing up on PAT images. The scattering of the fat material is lower than the aimed value.

A semi-anthropomorphic photoacoustic it is developed consisting of acoustically and optically characterised materials. The phantom does not perfectly mimic breast tissue, but the phantom can be further improved using the protocol that was formed.

Samenvatting:

Anthropomorphische borstfantomen zijn nodig voor validatie en verbetering van fotoakoestische beeldvormende systemen voor de detectie van borstkanker. Een eerste stap hierin is het fabriceren van een semi-anthropomorphisch fotoakoestisch borstfantoom, welke minder complexe, maar toch vergelijkbare structuren als weefsel bevat. Om dit te bereiken zijn eerst de akoestische en optische eigenschappen van de borstweefsels vet, klierweefsel, huid en bloed vanuit de literatuur bepaald. Daarna is er een inventarisatie van beschikbare fantoommaterialen en fabricatietechnieken gemaakt. De beschikbare materialen zijn gewaardeerd op basis van opgestelde eisen, waarna drie mogelijke materialen overbleven. Na akoestische karakterisatie van deze materialen, lijkt poly (vinyl chloride) plastisol (PVCP) het meest geschikte fantoommateriaal voor deze toepassing.

Het borstfantoom is ontwikkeld door gebruik te maken van 3D-geprinte mallen. Het fantoom bestaat uit een siliconen huid, een vetlaag en klierweefsel in het midden. De onregelmatige overgang tussen vet en klierweefsel is gebaseerd op een bloemkool. Twee tumoren en een bloedvat zijn aangebracht in het fantoom. Vet, klierweefsel en tumor/bloed zijn allen gemaakt door gebruik te maken van verschillende verhoudingen PVCP, wat in de basis bestaan uit de weekmakers di(2-ethylhexyl)adipaat (DEHA) and benzylbutylftalaat (BBP), een calcium-zink warmte stabilisator en PVC resin. Hieraan kunnen glasdeeltjes, titanium oxide (TiO_2) en zwarte plastic kleurstof worden toegevoegd om respectievelijk akoestische scattering, optische scattering of optische absorptie te induceren.

Een aangepaste invoegingstechniek is gebruikt om de materialen akoestisch te karakteriseren. De geluidssnelheid van vet, klierweefsel en bloed gelijkende materialen is respectievelijk 1447, 1511 en 1511 m/s. Voor dezelfde materialen geven machtsfuncties die door de akoestische attenuatie datapunten geplot zijn waardes van 0.42, 0.55 en 0.90 dB/cm bij 1 MHz. Akoestische impedanties van de materialen zijn 1.24, 1.61 en 1.82 MRayls. Het vet en klierweefsel hebben beide volledig ontwikkelde akoestische speckle. De inverse adding doubling method is gebruikt om de optische absorptiecoëfficiënt (μ_a) en gereduceerde verstrooiingscoeëfficiënt (μ_s') voor alle vier de weefseltypes te bepalen bij 785 nm. Dit resulteert in μ_a waardes van 2.75, 1.60, 7.11 en 0.39 cm^{-1} voor vet, klierweefsel, bloed en huid respectievelijk. Voor dezelfde weefseltypes μ_s' is 0.1, 10.9, 0 en 84.7 cm^{-1}.

Magnetische resonantie beeldvorming (MRI), ultrasound (US) B-mode beeldvorming en fotoakoestische tomography (PAT) zijn gebruikt om het fantoom te valideren. The overgang tussen vet en klierweefsel was te zien in zowel MRI als US beelden. De absorberende structuren waren met alle technieken te zien. De akoestische eigenschappen van de PVCP materialen waren goed afgestemd op weefselwaarden, wat resulteert in US beelden die vergelijkaar zijn met beelden van echt weefsel. De optische eigenschappen van huid en vet waren niet goed afgestemd op weefselwaarden, aangezien μ_s' van huid hoger is dan weefsel en μ_a van huid lager is dan weefsel bij 785 nm. De huid is daarom niet zichtbaar op de PAT beelden. De verstrooiing van het vet gelijkende materiaal is lager dan de literatuurwaarden waar op gemikt werd.

Een semi-anthropomorphisch fotoakoestisch fantoom is ontwikkeld, welke materialen bevat die akoestisch en optisch gekarakteriseerd zijn. Het fantoom bootst de borst niet perfect na, maar verbeteringen kunnen nog verder doorgevoerd worden op basis van het ontwikkelde protocol en de opgedane ervaringen.

Preface:

Dear reader,

From september 2017 to July 2018 I worked on my Master thesis at the Biomedical Photonic Imaging group at the University of twente. The assignment was to fabricate a well-characterised photoacoustic breast phantom. This report is the result of months of effort in doing research regarding this topic. I have enjoyed my period at BMPI a lot, joining in a lot of activities. The period of my graduation project was not all good however, since the last months of the project coincided with challenges on personal level. I would like to thank a few people for supporting me in this period.

First of all, I would like to give many thanks to my daily supervisor, Maura Dantuma. As we already knew each other from the honours programme contact was good right from te start. She was available for support whenever needed and together we found many solutions to each time another problem. I would also like to thank my second supervisor, and committee chairman, Srirang Manohar. He has been very supportive and really wants to be involved in the project. Further on, I would like to thank all people who helped me during some stage of the project, especially Wilma, David, Vincent and Françoise. Many thanks also to all the students of ZH268, with whom I had a lot of fun but could have serious conversations regarding one of our assignments. I would also like to thank all other BMPI members for giving me such a good time at the group.

I would like to give special thanks to my family, who supported me throughout the whole period and especially in these last couple of months. Finally, the biggest support during this period came from Pieter. Sometimes he had to suffer from my high demands, but he never complained and always kept helping me. Thank you for all of this.

Rianne van Dommelen
Enschede, 4th of July 2018

Contents

Acronyms:

BI-RADS	Breast Imaging Reporting and Data System
BMPI	Biomedical Photonic Imaging group
BPC	Black Plastic Colouring
BSC	Backscattering Coefficient
CE-MR	Contrast-Enhanced Magnetic Resonance
Gd	Gadolinium
GP	General Practitioner
Hb	Hemoglobin
LIUS	Laser Induced Ultrasound
MCDM	Multiple-Criteria Decision making Matrix
MRI	Magnetic Resonance Imaging
MST	Medisch Spectrum Twente
PAT	Photoacoustic Tomography
PDMS	Polydimethylsiloxane
PVA	Polyvinyl Alcohol
PVCP	Polyvinyl Chloride Plastisol
qPAI	quantitative Photoacoustic Imaging
RAM	Robotics and Mechantronics
RPLab	Rapid Prototyping Lab
SLS	Synthetic Laser Sintering
SNR	Signal-to-Noise Ratio
SoS	Speed of Sound
TMM	Tissue Mimicking Material
US	Ultrasound
US-CT	Ultrasound Computed Tomography
UT	University of Twente

1 Introduction

In this chapter the problem description is given in section 1.1. From this the research aim and research questions are extracted in section 1.2. To have an overview of the project the context of the resarch is given in section 1.3 and finally the structure of this report is explained in section 1.4.

1.1 Problem definition

Breast cancer impacts over 1.5 million women worldwide every year. [1] The five-year survival rate of early stage breast cancers is up to 80-90% in countries with advanced medical care. However this number drops to 20-30% for advanced stage breast cancers. [2] Early detection and correct diagnosis are therefore critical for the survival chances of breast cancer patients.

The current process of screening and diagnosing breast cancer in the hospital Medisch Spectrum Twente (MST) in Enschede is visualised in figure 1.1. Screening is performed on women within the age group of 50 to 75 years. Every two years they receive an invitation to have an x-ray mammogram made. Depending on the results of this mammogram women are forwarded to the diagnostic trajectory or are sent back home. Other patients in the diagnostic trajectory are forwarded by the General Practitioner (GP), because abnormalities were found by either self-detection or by regular check-up.

The first step of diagnosis is performed by both x-ray mammography and ultrasound (US). If the results are suspicious, corresponding to a BI-RADS (Breast Imaging Reporting and Data System) classification 3-5, a biopsy is taken, which is seen as the golden standard in breast cancer diagnosis. If more information on the tumor is needed, magnetic resonance imaging (MRI) is done.

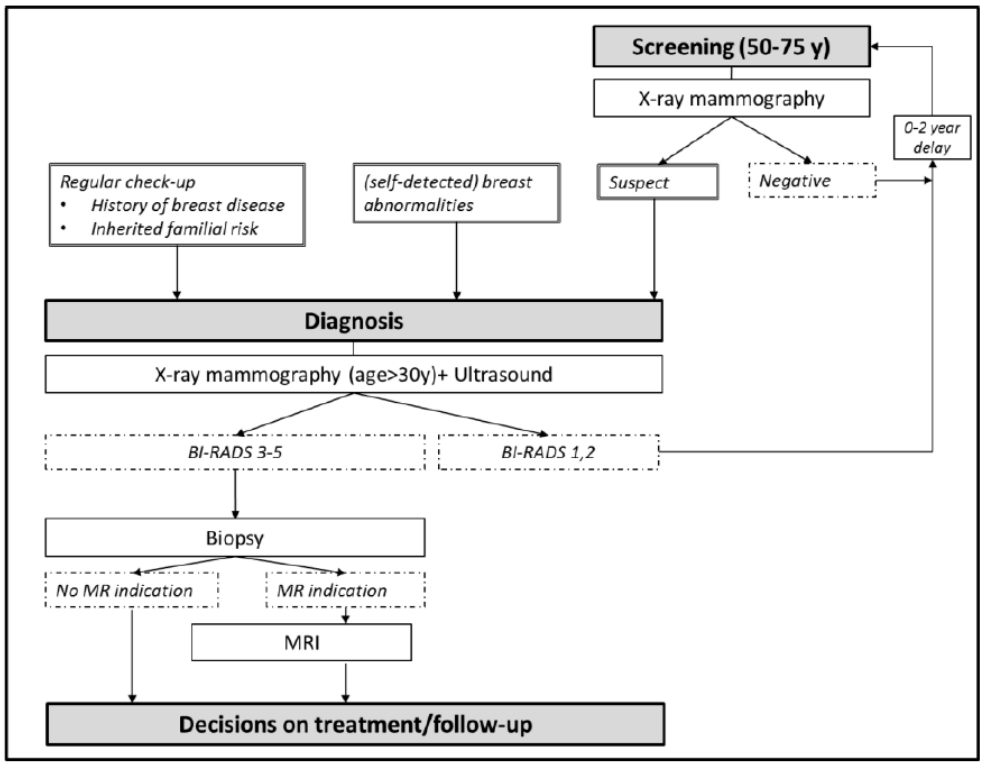

Figure 1.1: Flow diagram of breast imaging in the MST in the Netherlands, showing the most common pathways. Screening and diagnosis have a different function; therefore the requirements for the technologies acting in these regimes are different. Screening is performed with x-ray mammography only, while diagnosis consists of often x-ray mammography, ultrasound and if needed a biopsy and MRI. (Reproduced from [3])

These four techniques all have their own characteristics, advantages and disadvantages:

- **X-ray mammography**. This technique is based on the difference in x-ray absorption between different breast tissue types. Mainly due to its high specificity x-ray mammography is the only breast cancer screening method. Besides it is well able to detect microcalicifications, making early detection more feasible. A major disadvantage of x-ray mammography is the low sensitivity for tumor detection in women with dense breasts, carrying high amounts of fibroglandular tissue. These are women before menopause and generally younger women. Other disadvantages are the discomfort caused in women receiving a mammogram and the exposure to ionizing radiation. [4, 5]

- **Ultrasonography**. Ultrasound is complementary to x-ray mammography in the diagnosis of cancer in dense breasts and it can check on the presence of cysts, but it cannot detect microcalcifications. It is also used to check on abnormalities in the lymph node in the armpit and to perform US guided core needle biopsies (CNB). A major disadvantage of the currently in clinic available techniques is the operator dependency, causing the specificity to drop and unnessecary biopsies to be taken due to low sensitivity. [4–6]

- **Biopsy**. There are three types of biospies: fine needle aspiration, core needle biopsy and excisional biopsy. The most often used technique is core needle biopsy, in which a small sample of suspicious tissue is removed from the breast. It often uses ultrasound for guidance during the procedure. The sample is analysed in the lab by a pathologist. Biopsies are seen as the golden standard in breast cancer diagnosis. Disadvantages of biopsies are that the procedure is invasive and only a small volume of tissue is investigated. [5]
- **Magnetic Resonance Imaging**. High resolution images containing information on the anatomical and physiological structure of the breast can be obtained by MRI, thereby increasing diagnostic accuracy. With MRI the contrast agent gadolinium (Gd) is injected to highlight specific regions. Main drawbacks of the technique are the long measuring times, high costs and lack of availability in all hospitals. Besides a contrast agent is needed to obtain more detailed information on for example vasculature. [4, 5]

In order to overcome some of the disadvantages in these techniques and simplify the diagnosis trajectory, new or improved imaging modalities for breast cancer detection are under development. All techniques make use of certain tumor characteristics to give a diagnosis. One of these characteristics in malignant tumors is angiogenesis. Angiogenesis, also called neovascularization, is the proliferation of new blood vessels. By supplying the tumor with more oxygen and nutrients these new blood vessels are crucial in the growth of a tumor. [7] The process of angiogenesis in a tumor is visible in figure 1.2. The *in situ* tumor is in a steady state in size (A). Due to insufficient oxygen the tumor cannot grow larger than about 1-2 mm^3 without cells in the middle dying. [8] When angiogenesis is turned on by releasing protein growth factors (B) the tumor starts to grow into a malignant type which is able to induce metastases (C).

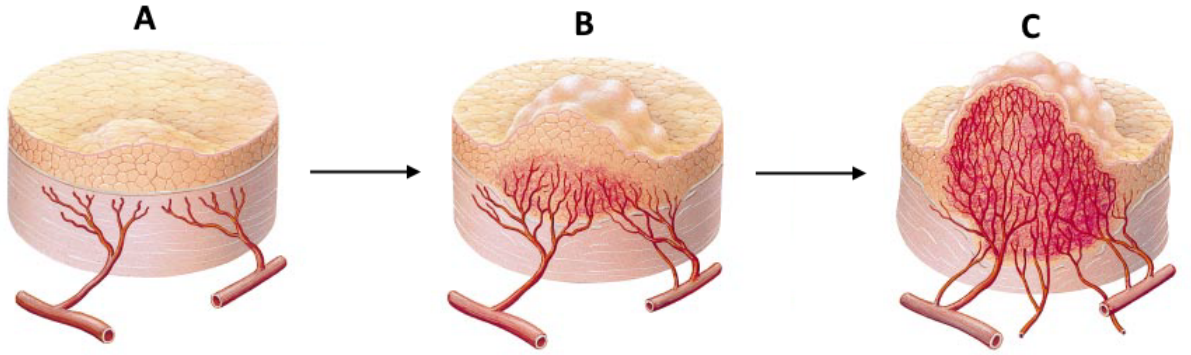

Figure 1.2: The process of angiogenesis visualised. (A) The *in situ* tumor is in a steady state due to insufficient oxygen until (B) growth factors are released, causing angiogenesis to begin and the tumor to start growing. (C) This growth continues, eventually causing metastases. [7]

The presence of hemoglobin (Hb) in blood causes it to absorb light a lot stronger than surrounding tissue at certain wavelengths, creating the potential to detect tumor vascularity by making use of this high absorption of light by blood. One of the breast imaging

modalities that makes use of this principle to obtain contrast and detect breast tumors by analysing the blood vessel density is photoacoustic tomography (PAT). With PAT it becomes possible to form a 3D-map of the blood vessel structure inside the breast.

The underlying principle behind this technique is the photoacoustic (PA) effect [9], which is exploited to combine optical excitation with acoustic detection. Because ultrasound is scattered weaker than light in tissue, PAT provides high resolution in relatively large tissue volumes. [10] The principle is explained in figure 1.3. This is a schematic overview of the PAMMOTH system, which is a PAT system for breast cancer detection and is being developed at the University of Twente (UT). The breast is pendant in a tank filled with water for acoustic coupling. When the breast is illuminated by a pulsed laser beam, a part of this light will be absorbed by chromophores in the tissue (A). The laser has a pulse length shorter than the tissue's thermal and stress relaxation times, to provide thermal and stress confinement inside the absorber. [9] This causes a local temperature rise and thermoelastic expansion of this part of the tissue. Due to this thermoelastic expansion (B) a pressure is built up, which results in the release of an ultrasound wave. The US wave can then be detected by ultrasound transducers (C). The positions of the absorbers can be derived by making use of image reconstruction algorithms, the simples of which backprojects the recorded signals into image space using the tissues speed of sound (SoS). The photoacoustic wave generation and propagation under both thermal and stress confinement is described by the photoacoustic equation [11]:

$$(\nabla^2 - \frac{1}{c_s^2}\frac{\delta^2}{\delta t^2})p(\mathbf{r},t) = -\frac{\beta}{C_P^2}\frac{\delta H(\mathbf{r},t)}{\delta t} \tag{1.1}$$

In which ∇^2 is the Laplace operator, c_s the speed of sound, $p(\mathbf{r},t)$ the acoustic pressure as function of location $\mathbf{r}$ and time t, β the coefficient of thermal expansion, C_P the heat capacity at constant pressure and H the heating function defined as the thermal energy converted per unit volume and per unit time. It is related to the optical absorption coefficient μ_a and fluence rate ϕ by: $H = \mu_a\phi$. [11]

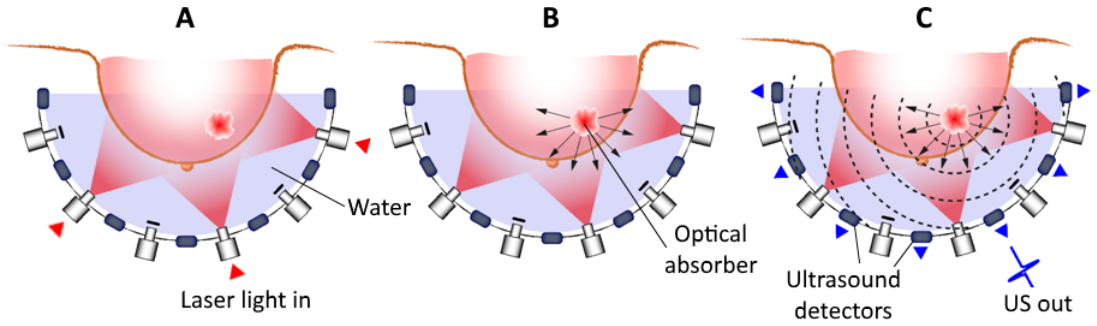

Figure 1.3: Schematic overview of photoacoustic tomography for breast imaging in which (A) the breast is illuminated with pulsed laser light, (B) chromophores in blood vessels highly absorb the laser light causing thermal expansion in these local spots. (C) The resulting pressure buildup induces the formation of an ultrasound wave, which can be detected by ultrasound transducers.

Photoacoustic tomographic breast imaging systems are currently not approved for clinical use, although a number of systems is being developed and tested on patients. [12] One of the main problems in introducing the systems into the clinic is the prediction of *in vivo* performance. More knowledge is needed on complex tissue interactions with light and ultrasound to overcome this problem. A possibility for enhancing the knowledge level can be found by looking at the system development process. Figure 1.4 shows an expected flow diagram of this process. It concerns an estimation, which is not based on literature directly. The thickness of the arrows is an indication for the amount of devices flowing from one block to another. On the left side the current situation and on the right the desired new situation can be seen. In the right side of this image the light blue arrows indicate no changes, while the dark blue arrows indicate changes in flow.

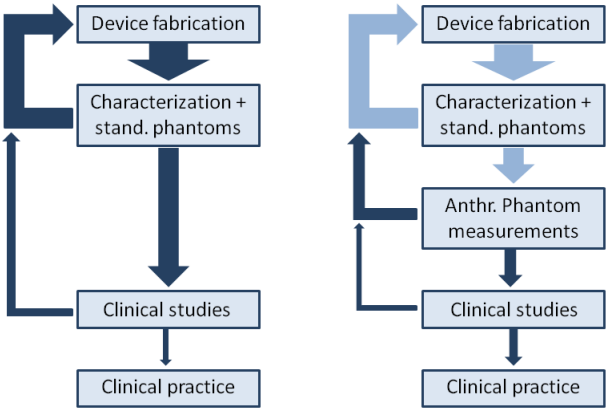

Figure 1.4: A flow diagram of the estimated development process of photoacoustic systems in the current situation and the proposed new situation with the intermediate step of testing on anthropomorphic phantoms

The cycle is started with initial prototype fabrication, of which the design is often supported by computer simulations. Once this is completed the prototype is characterised on standardised phantoms, which have a homogeneous background mimicking healthy breast tissue and evaluate the effect of a single parameter on the image quality. Often single absorbers are inserted in an homogeneous background by which i.e. the resolution, imaging depth and contrast of the system is determined. An example of such a phantom can be found in the study performed by Bohndiek *et al.*. [13] After optimising the measurement device and image reconstruction algorithms based on these standardised phantoms measurements and computer simulations, clinical studies and healthy volunteer measurements may be performed to test *in vivo* performance.

However, until now these clinical studies have not resulted in clinical acceptance of PAT systems, although time and financial investments have been made. This might be explained by the large step between testing on homogeneous phantoms and the clinical performance on highly heterogeneous breast tissue, composed of a variety of tissue types. Since the acoustic and optical properties of these tissue types differ significantly, see chapter 2, one can question whether the homogeneous phantoms mimic the complex structured breast tissue sufficiently. To diminish this gap between testing on homogeneous phantoms

and performing clinical studies an intermediate step of testing on anthropomorphic (= having human form) phantoms is suggested, which is implemented on the right side of figure 1.4. These anthropomorphic phantoms can be used to mimic *in vivo* photoacoustic behaviour in an earlier stage with less time and financial investments in order to improve image quality and the clinical acceptance of PAT systems.

It is especially important to accurately mimic breast tissue to be able to reach the ultimate goal of quantitative photoacoustic imaging (qPAI). qPAI has the potential to provide *in vivo* images of chromophore concentrations, like ratio of oxy- and deoxyhemoglobin, the oxygen saturation, which offers information on the pathology and functioning of tissue. [14] From the photoacoustic equation (eq. 1.1) it is seen that the photoacoustic signal is dependent on the local light fluence and optical absorption. Due to the large number of unknowns, as the light fluence is dependent on the optical absorption and optical scattering, extracting chromophore concentrations remains a challenge. [15]. While iterative model based algorithms are being developed and tested on numerical phantoms, the true validation will have to be performed on a realistic phantom with accurate simulation of optical and acoustic properties of breast tissue. The use of anthropomorphic phantoms with well-defined acoustic and optical properties may form a basis in developing methodologies for solving these problems and extracting chromophore concentrations.

1.2 Research questions

Fabricating complex 3D anthropomorphic breast phantoms is the ultimate goal in mimicking female breasts for improving breast cancer detection and diagnostic systems. Currently, no such phantoms exist for photoacoustic applications. The availability of photoacoustic breast phantoms is limited to homogeneous phantoms or 2D heterogeneous phantoms without having the shape of a breast. An intermediate step in fabricating a 3D anthropomorphic breast phantom is therefore to develop a 3D semi-anthropomorphic breast phantom, in which the structures are not as complex as in real tissue. This results in the aim of this research which is to fabricate a 3D semi-anthropomorphic photoacoustic breast phantom, to characterise its acoustic and optical properties and test its performance to mimic the female breast, resulting into the following research question:

How is a semi-anthropomorphic breast phantom for photoacoustic applications fabricated?

A number of sub research questions should be answered before the main goal of the research can be accomplished. These questions are listed below:

1. What are the acoustic and optical properties of the female breast?
2. What are potential materials to use in fabricating the phantom?
3. What are potential fabrication techniques to use for fabricating the phantom?
4. Which material is most suitable to use as phantom material?
5. How can this material be optimised for the acoustic and optical properties?
6. How can a semi-anthropomorphic breast phantom be designed?
7. What is the performance of the photoacoustic breast phantom?

1.3 Context of research

This research is part of the PAMMOTH project at the Biomedical Photonic Imaging Group (BMPI) at the (UT). PAMMOTH is a Horizon 2020 project and started in January 2017. The aim of this project is to develop a system for breast cancer diagnosis which combines ultrasound computed tomography (US-CT) with PAT. The photoacoustic tomographic system that will be constructed is the third photoacoustic breast imaging system developed at the UT. The second system is currently used in a clinical trial study. Many partners are part of the PAMMOTH consortium, each having its own responsibilities (figure 1.5). The device will be built at the UT, which also is responsible for the implementation and optimisation of PA imaging and laser-induced ultrasound imaging (LIUS), and system characterisation. Phantom fabrication to test and characterise the system is performed by the University of Bern. However since multiple materials are available for PA phantoms (see chapter 3) parallel research on phantom fabrication using different materials is performed at the UT.

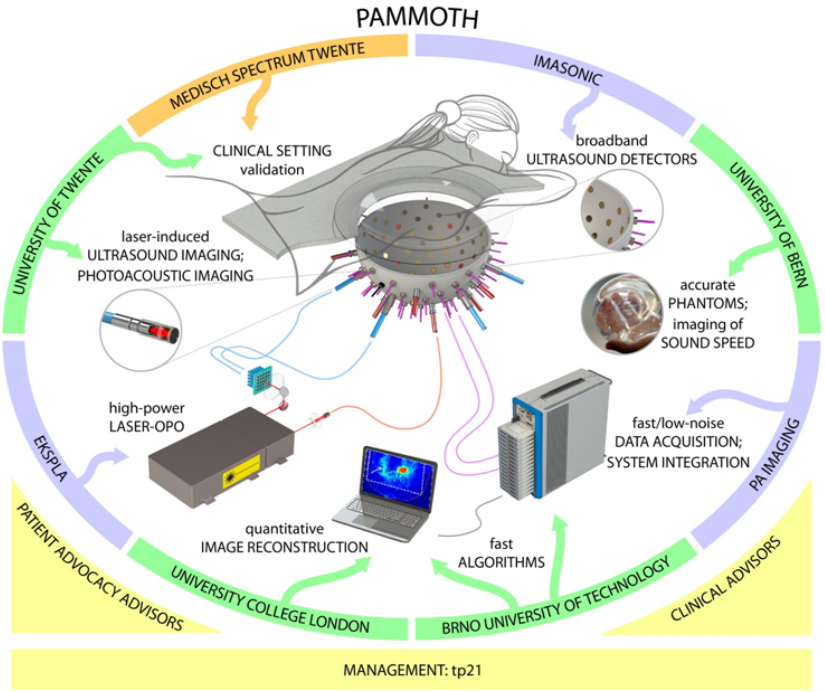

Figure 1.5: Overview of the PAMMOTH project with responsible partners in the consortium

1.4 Structure

The structure in this thesis follows all steps needed to fabricate the 3D semi-anthropomorphic photoacoustic breast phantom. It is important to know what needs to be mimicked by the phantom, which begins with giving an overview of the breast anatomy in chapter 2. In this chapter the acoustic and optical properties of relevant breast tissue types are given

as well. In chapter 3 an overview of in literature available phantom materials and fabriquation techniques is given. Candidate materials are found by scoring all these materials based on a set of requirements and wishes that is composed. These candidate materials are acoustically characterised in chapter 4, resulting in one material combined that is most suitable to use as a phantom material. In chapter 5 this materials is optimised for its acoustic and optical properties. After this, attention is paid to the design and fabrication process of the phantom in chapter 6. The actual photoacoustic phantom is fabricated, characterised and imaged in that chapter as well. Finally, some conclusions and recommendations are given.

2 | Breast tissue

In this chapter the first research question is answered: *What are the acoustic and optical properties of a female breast?* In order to find an answer to this question first an overview of the breast anatomy is given in section 2.1. Then based on an available 3D digital phantom described in section 2.2 he main tissue types relevant for photoacoustic imaging are extracted. Of these tissue types an overview of the acoustic and optical properties is given in section 2.3, such that it is known to what properties the phantom should be tuned to mimic female breast tissue.

2.1 Breast anatomy

The breasts, also called mammary glands, have as function to produce milk for feeding the newborn infant. They are located on the anterior and lateral parts of the chest, overlaying the pectoral muscle in the chest wall. [16] The breast consists primarily of three types of tissue: adipose tissue (breast fat), glandular tissue and fibrous connective tissue. [17] Figure 2.1 shows adipose tissue to be found at the outer part of the breast, while glandular and connective tissue together form the fibroglandular tissue in the center of the breast. The ratio of fibroglandular versus adipose tissue defines the breast density and differs from individual to individual, and depends largely on a woman's age and hormonal status such like menstruation, pregnancy, lactation, hormone therapy and menopause. [16]

In figure 2.1 b) and c) two MR images of different breast densities are shown. [18] The mammary gland is covered by a skin layer and a ring of pigmented skin (areola) surrounding the nipple slightly below the center of the breast. The glandular tissue consists of 15 to 25 lobes, which are separated from each other by fibrous connective tissue and fat. The lobes consists of smaller lobules, which contain alveoli that actually produce the milk when a woman is lactating. The lactiferous ducts transport the milk from the alveoli to the nipple. The function of fibrous connective tissue is to maintain the inner structure of the breast and to support connection to the chest wall, while adipose tissue is connective tissue and determines the breast size. [19] Furthermore the breast contains a network of blood vessels and lymphatic vessels. The latter draining fluid to the lymph nodes in the armpit and behind the sternum.

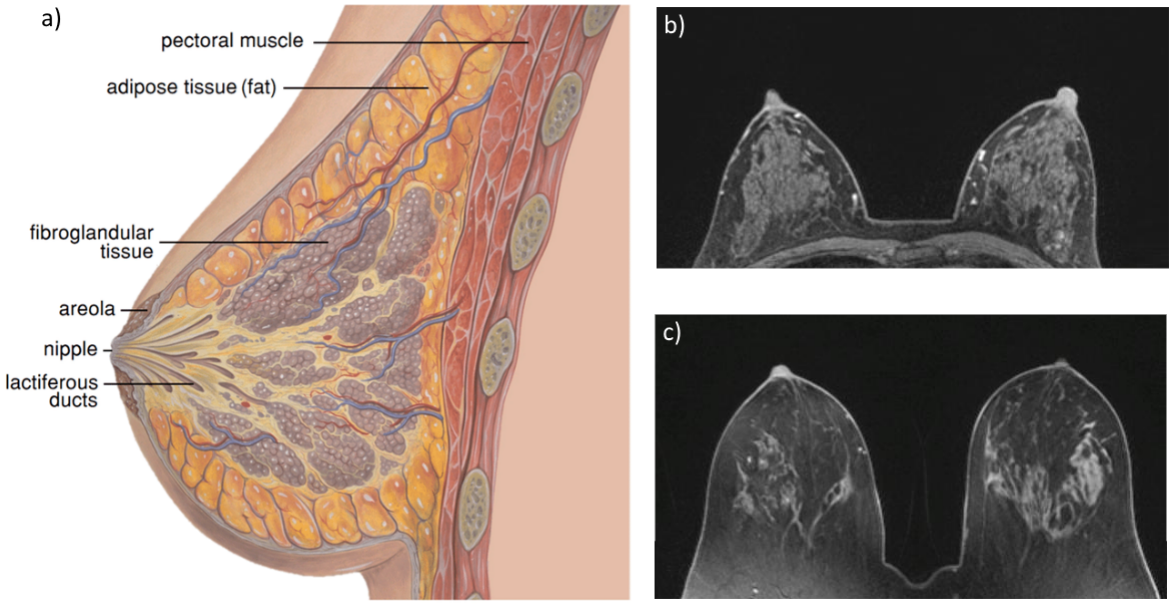

Figure 2.1: The anatomy of the female breast with different tissue types visible. (a) A schematic representation with different tissue types indicated, (b) and (c) two MR images showing different breast densities. Higher intensity indicates fibroglandular tissue located more centrally, lower intensity shows adipose tissue located on the outside and in between fibroglandular tissue. [16, 18]

2.2 Digital phantom

A few 3D digital breast phantom segmented from MRI data are available in literature. [20] The phantoms consist of four tissue types: fat, fibroglandular tissue, skin and blood vessels. An extensive explanation on the generation of the digital phantom can be found in Lou *et al. (2017)* [20]. Briefly, the numerical breast phantoms are constructed from clinical contrast-enhanced magnetic resonance (CE-MR) data by using segmentation methods for extracting the four tissue types. Within normal MR images skin, fat and fibroglandular tissue can be identified well, contrast agents help in extracting blood vessels from the CE-MR image as well. The fat-suppressed MR images were made with the patient lying in prone position, which is comparable to the position patients take in the photoacoustic mammoscope. Generating the numerical phantom is done by first identifying the breast volume in the image. Then the vessels are extracted by using the pre- and postcontrast data. Thirdly the skin is segmented by using its high intensity compared to background and fat in the outer part of the breast. Once that is done, the fat and fibroglandular tissues can be extracted by making use of their difference in MR intensity. Lastly, the actual digital phantom is generated by assigning a tissue type to each voxel within the breast volume. By adding appropriate acoustic and optical properties of each tissue type a numerical photoacoustic breast phantom is generated.

With the methodology as described above three different breast phantoms were generated, each from a different healthy volunteer. The voxel size of the phantoms is 0.2 x 0.2 x 0.2

mm. All three phantoms were generated from images of the left breast. The sizes and breast densities vary among the three phantoms [20]:

- *Neg07* consists of scattered fibroglandular breast tissue and has dimensions 12.3 x 9.7 x 14.4 cm, background included.
- *Neg35* consists of heterogeneously dense breast tissue and has dimensions 5.7 x 8.2 x 14.4 cm, background included.
- *Neg47* consists of extreme dense breast tissue and has dimensions 9.9 x 12.3 x 15.0 cm, background included.

The complex anatomy of the female breast as was seen in the previous section, is also well visible in these digital phantoms. In figure 2.2 images of the smallest breast *Neg35* are presented. Each of the four tissue types is visualised separately, in which especially the complexity of adipose and fibroglandular tissue is evident. This digital phantom will be the basis for the 3D semi-anthropomorphic phantom generated in this research its small dimensions cause the phantom to be less expensive to experiment with. Since fat and fibroglandular tissue form the majority of breast tissue, these tissue types are most important in fabricating the phantom. The complexity of these tissue types will be elaborated upon in chapter 3.

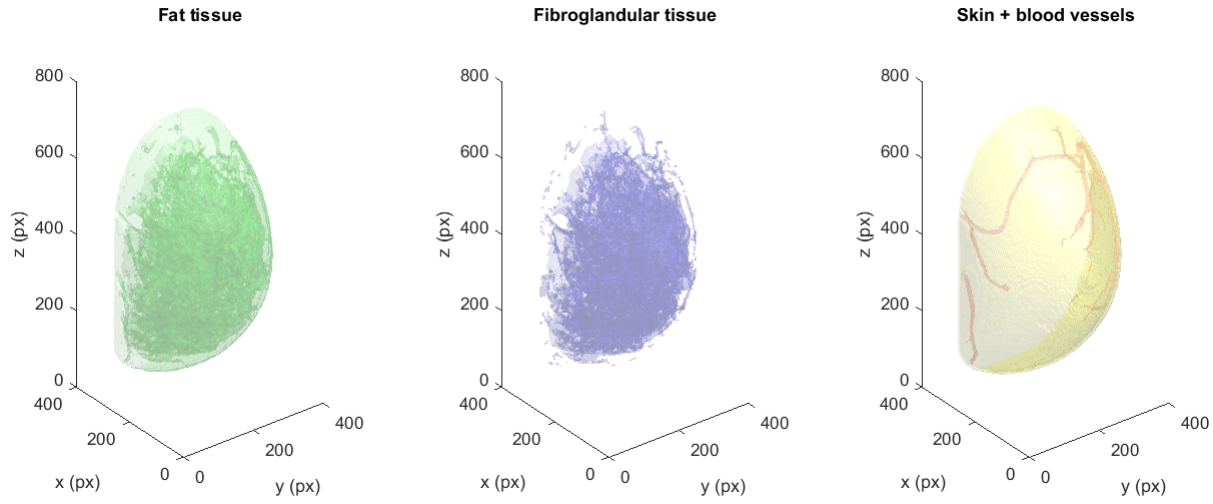

Figure 2.2: 3-D numerical breast phantom of *Neg35* which consists of heterogeneously dense breast tissue and has dimensions 284 x 411 x 722 pixels (5.7 x 8.2 x 14.4 cm). In the left image the segmented fat tissue, in the middle fibroglandular tissue and in the right image skin and blood vessels are presented. [20]

2.3 Acoustic and optical properties

To fabricate a realistic photoacoustic phantom with the four tissue types mentioned in the previous section (fat, fibroglandular tissue, skin and blood vessels) the acoustic and optical properties of *in vivo* breast tissue need to be known. Therefore a literature study

has been performed to obtain the appropriate values. This literature study has been divided into an acoustic and optical part.

2.3.1 Acoustic properties

The acoustic properties of tissue are obtained in this section. First an overview and definitions of relevant properties are given.

Definitions

In photoacoustics we are dealing with longitudinal sound waves, which means a back-and-forth motion of particles is formed as the sound wavel travels through an elastic medium. [21] The displacement of these particles from their equilibrium position causes a small pressure disturbance, which represents the acoustic wave. This is described by the acoustic wave equation (eq. 2.1), which can also be recognized in the photoacoustic equation (eq. 1.1).

$$\nabla^2 p(\mathbf{r},t) - \frac{1}{c_s^2}\frac{\delta^2 p(\mathbf{r},t)}{\delta t^2} = 0 \tag{2.1}$$

In which ∇^2 is the Laplace operator, $p(\mathbf{r},t)$ the acoustic pressure at location $\mathbf{r}$ and time t, and c_s the speed of sound. The propagation of the acoustic wave through a medium depends on a number of material properties, namely: speed of sound (SoS), acoustic impedance (Z), acoustic attenuation (AA), backscattering coefficient (μ_{bs}) and non-linearity parameter (B/A). Some definitions of these properties are given.

The speed of sound of a sample (c_s) is defined as the distance the acoustic wave travels through an elastic medium along its propagation direction per unit of time. It depends on both the bulk modulus K and the density ρ by [21]:

$$c_s = \sqrt{\frac{K}{\rho}} \tag{2.2}$$

The acoustic impedance is related to the speed of sound and mass density (eq. 2.3). The difference in acoustic impedance between two materials at a boundary influences the amount of energy that is transmitted or reflected. A large acoustic impedance mismatch leads to a high reflection coefficient.

$$Z = \rho c_s \tag{2.3}$$

Acoustic attenuation is defined as the losses the energy the pressure wave loses while travelling through a medium. The attenuation is often expressed in decibels per centimeter (dB/cm) and is defined as [21]:

$$AA = \frac{20 \log(A/A_0)}{l} \tag{2.4}$$

With AA the attenuation of the acoustic wave in dB/cm by travelling through a certain medium, A the amplitude of the pressure wave after travelling through a medium of length l and A_0 the amplitude of the pressure wave before travelling through the medium.

The backscattering coefficent is a measure of the differential scattering cross section per unit volume. [22] It is difficult to measure accurately, with large variations occuring between different measurement techniques. [23] Finally nonlinearity is a property of a medium by which the shape and amplitude of a signal at a location are no longer proprotional to the input excitation. [21] The nonlinearity parameter (B/A) is a measure for this. The values A and B in this parameter are the coefficients of the first and second order terms of the Taylor series expansion of the equation relating the pressure inside a material to the material's density. Because the nonlinear effects of tissue are small it is difficult to measure this accurately. [22]

Of these properties the speed of sound and acoustic attenuation are most important to control in the phantom. [24] The speed of sound influences the image reconstruction, while the attenuation has an effect on the amplitude of the signal. Besides, acoustic impedances should be similar to those in tissue, such that the reflection and transmission coefficients of the boundaries are similar. Since it is difficult to accurately measure the backscattering coefficient this property is not tuned. However the speckle formation is optimised by ensuring fully developed speckle resulting in pure diffusive scattering. [25] The nonlinearity parameter is not tuned since the effects on the generated signal are negligible.

Tissue properties

Now the above acoustic properties of breast tissue are analysed for the desired tissue types; fat, fibroglandular, skin and blood vessels. In appendix A an overview of all found data in literature is given. A summary of these values is given in table 2.1 below.

Table 2.1: Acoustic properties of four breast tissue types at different frequencies, extracted from reported literature values. [21, 26–39]

Tissue type	**SoS [m/s]**	**AA [dB /cm /MHz]**	$\boldsymbol{\rho}$ $[\boldsymbol{kg/m^3}]$	**Z [MRayls]**	$\boldsymbol{\mu_{bs}}$ $[\boldsymbol{Sr^{-1}cm^{-1}}]$
Skin	1607 ± 32 (1580-1650)	1.22 ± 0.83 (0.28-1.84)	1150	1.85	$1.6 * 10^{-6}$
Fibroglandular	1524 ± 27 (1487-1549)	2-2.7	1040	1.59	$1.26 * 10^{-2}$
Fat	1440 ± 19.9 (1400-1481)	1-1.8	911	1.31	$3.2 * 10^{-3}$
Blood	1582 ± 5 (1575-1586)	0.15 ± 0.01 (0.14-0.15)	1058 ± 3 (1055-1060)	1.67	10^{-5}

Multiple references on the speed of sound of the four tissue types exist, which made it possible to present average values and standard deviations. The values for fibroglandular, fat and blood are from measurements performed at 37 °C of which the measurements on fat and fibroglandular tissue were mostly performed *in vivo*. The temperatures of skin SoS measurements varied among different experiments. This may be one of the reasons why such a large variance is seen in the skin values. Another reason could be due to differences in SoS at different skin locations. [40] Overall our SoS values are similar to those used in previous phantoms studies by Vogt *et al.* [24] and Lou *et al.* [20], although the difference in SoS between fat and fibroglandular tissue is larger due to the inclusion of more literature.

The acoustic attenuation for skin and blood was also found by taking the average of multiple values in literature. For fat and fibroglandular tissue little data was available, so values from Vogt *et al.* [24] were used together with the few values given in the table in the appendix. The skin AA values were determined at frequencies ranging from 2.9 to 10.3 MHz, whereas attenuation values for fat and fibroglandular tissue were retrieved from experiments with a range of 1 to 10 MHz. The density of blood was again averaged over multiple available literature reported values. The density values for the other tissue types were obtained by using data from Lou *et al.* [20]. The acoustic impedances were calculated from the average SoS and densities. Finally, the backscattering coefficient is determined by taking the average from the few values available in literature.

2.3.2 Optical properties

The optical properties of tissue are obtained in this section. First an overview and definitions of relevant properties are given.

Definitions

In photoacoustic a pulsed laser is used to illuminate tissue, in which this light can be absorbed after which an acoustic wave is generated. The initial pressure generated at a certain location is dependent on the intensity of the light that reaches this spot. The intensity of the light depends on certain tissue optical parameters, namely the absorption coefficient (μ_a), reduced scattering coefficient (μ_s'), scattering anisotropy (g) and refractive index (n). The meaning of these properties is explained.

When a light beam travels through a medium the light is attenuated due to two loss mechanisms, absorption and scattering, which is described by:

$$\mu_{att} = \mu_a + \mu_s \tag{2.5}$$

Absorption is the principle of the uptake of energy of a photon by the electrons of atoms in matter. Absorption is material- and wavelength-specific and is described by the absorption coefficient with unit m^{-1}. The absorption coefficient has as definition the probability of photon absorption by a medium per unit path length. [41]

Another mechanism that causes attenuation of light is scattering. In scattering the electromagnetic wave undergoes a change of direction due to interaction with local non-uniformities in the medium. [42] The scattering coefficient (μ_s) describes the losses due to these interactions and is defined as the probability of photon scattering by a medium per unit path length. [41] When the direction of scattering is also taken into account by means of the scattering anisotropy one finds the reduced scattering coefficient (equation 2.6), which describes the scattering efficiency. Scattering is forward directed when $g = 1$, backward directed when $g = -1$ and isotropic scattering occurs in the case of $g = 0$. In tissue the anisotropy is approximately 0.9.

$$\mu_s' = \mu_s(1 - g) \tag{2.6}$$

Finally, the refractive index describes the behaviour of light at a boundary between two media. Based on Snell's law the angle of refraction can be determined and the Fresnel equation gives the fraction of light that is transmitted or reflected. [42] The refractive index is the ratio between light speed in vacuum (c) and light speed in the medium (v):

$$n = \frac{c}{v} \tag{2.7}$$

Of these properties μ_a and μ_s' are most important to control in the phantom, because with these two parameters the fluence of light at a certain location in tissue can be described

best. The refractive index is important to describe specular reflectance which is primarily of influence only on the boundary background-tissue. The reduced scattering coefficient is chosen above the scattering coefficient, because it takes direction into account.

Literature values

The absorption and reduced scattering coefficient of the four tissue types (skin, fat, fibroglandular and blood) were analysed. In table 2.2 a summary of the from literature extracted optical properties of breast tissue is given. A more detailed table can be found in appendix B.

Table 2.2: Optical properties of four breast tissue types at 785 nm, extracted from reported literature values. [43–46]

Tissue type	$\mu_a[cm^{-1}]$	$\mu_s'[cm^{-1}]$	**g**	**n**
Skin	0.3 ± 0.2 (0.1-0.5)	16.1 ± 8.0 (6.8-24.2)	0.99	1.40
Fibroglandular	0.06	11.6 ± 0.6 (11.2-12.2)	0.96	1.40
Fat	0.03	8.8 ± 0.7 (8.2-9.3)	0.98	1.40
Blood	6.6 ± 3.3 (4.3-9.0)	9.1 ± 6.3 (4.5-16.3)	0.975	1.38

The wavelengths of the PAMMOTH project are not set yet, but at least one of the wavelengths will be in the range of 750-800 nm. Therefore for tuning the photoacoustic phantom it was decided to use a wavelength in this range and for which the optical properties were well defined in literature. Therefore it was decided to tune the optical properties for a wavelength of 785 nm. The values for μ_a and μ_s' of fat and fibroglandular tissue are measured at 785 nm, with the latter being averaged over multiple literature values. [44, 46] These optical properties for skin are measured at 800 nm. [43] The optical proeprties of blood was averaged over values available for 760 and 785 nm. Anisotropy of fat and fibroglandular tissue were averaged over literature values for 850 and 760 nm, while these values for skin and blood were found at 760 nm only. [20, 44, 45] The refractive indices of all tissue types were found at 760 nm. [20]

As with the acoustic properties again variations are seen in literature values. This depends of course on the wavelength used to find the optical properties, but also on the methodology used and on variations between patients. Especially in optical absorption large differences (even up to a 10-fold difference) were seen. It was decided to use the values from Brooksby *et al.* [46] for μ_a of fat and fibroglandular tissue since these measurements were performed *in vivo*, while those of Peters *et al.* [45] are obtained from *in vitro* experiments. μ_a of skin is an average of the values measured by Sandell *et al.* [43] and values calculated using a MATLAB script available online. [44, 47] This script was also used to calculate the μ_a of blood, combined with values from Lou *et al.* [20]. The absorption coefficient of blood is however variable, since the oxygen saturation of blood strongly influences the absorption spectrum.

2.4 Conclusions

In this chapter all information required to answer the question *What are the acoustic and optical properties of a female breast?* is discussed. First the anatomy of female breasts was described, which resulted in an overview of the most important tissue types one can find within the breast; adipose, glandular and fibrous connective tissue. Besides the breast is surrounded by skin and contains blood and lymphatic vessels. The online available digital phantom that was also described in this chapter contains four of these tissue types; skin, fat, fibroglandular tissue and blood vessels. Due to the presence of blood vessels this phantom is suitable for photoacoustic applications and its great detail based on MR data of actual female breasts makes it a good basis for our semi-anthropomorphic phantom. The four tissue types were characterised by the properties most important for the purpose of this research, being speed of sound, acoustic attenuation, optical absorption coefficient and reduced scattering coefficient.

3 | Possibilities for phantom fabrication

This chapter elaborates on the possibilities for fabricating the semi-anthropomorphic breast phantoms. Fabrication consists of two main choices that need to be made, that are summarized in the second and third sub-research questions: *What are potential materials to use in fabricating the photoacoustic phantom?* and *What are potential fabrication techniques to use for fabricating the photoacoustic phantom?* In order to find an answer to these questions, first the requirements the phantom should fulfill are set up in section 3.1. Then a literature study on available materials for photoacoustic applications in literature is given in section 3.2. After this, in section 3.3, possible fabrication techniques are extracted from the literature available on phantoms for both photoacoustic and other imaging modalities. In section 3.4 the materials in combination with fabrication techniques are evaluated on the requirements the phantom should fulfill, after which concepts are generated. Finally answers to the research questions are formulated to remain with one or more materials and fabrication techniques suitable for fabricating the photoacoustic breast phantom.

3.1 Phantom requirements

A list of requirements and wishes was made by evaluating literature [13, 14, 48] and determining the needs for the PAMMOTH project. Each requirement/wish is described generally, after which quantitative values were assigned to them. Besides each requirement/wish is given a value of importance, ranging from 1-5 with 1 being least important, and 5 being most important. Some features were subdivided into a requirement and a wish, with the wish being more restricted but having a lower importance than the requirement.

The most important requirements are the correct ranges of acoustic and optical properties, speckle formation and the realistic architecture. The phantom has to consist of at least two layers of fat and fibroglandular tissue, with the appropriate acoustic and optical properties as were found in the previous chapter. Ideally these properties can be tuned even further to also mimic the skin and blood vessels. The speckle formation is important for using the phantom in imaging systems combining both photoacoustic with ultrasound imaging, since speckle and backscattering provides contrast in US imaging. Further on, the availibility of recipes in literature to tune the phantom materials is desirable, since this spares a lot of time of having to characterise it for different material compositions, and provides security of knowing the material is tunable to a certain extent. Long-term stability together with reproducability, ease of fabrication and price is important since one wants to have a phantom that can be used multiple times to characterise and test the imaging system such that the properties stay the same, time and financial investment keep low. The price is based on the price of commercially available acoustic phantoms.

Regarding safety it is important that the materials are non-toxic in both fabricating and handling the phantom. Finally, the architecture as described before should at least consist of two layers of fat and fibroglandular tissue, but ideally it is mimicking the digital phantom in both the number of tissues and its resolution.

Table 3.1: An overview of the requirements and wishes the phantom should fulfill according to literature and demands for the PAMMOTH project. Quantitative values were assigned to each requirement/wish, which were given score of importance as well.

General description	**Specification**	**Requirement / Wish**	**Importance**
Correct range of acoustic properties (section 2.3.1)	SoS: 1440-1530 m/s, AA: < 1dB/cm @ 1 MHz	Requirement	5
	SoS: 1440-1600 m/s, AA: <0.2 dB/cm @ 1 MHz	Wish	2
Correct range of optical properties (section 2.3.2)	μ_a : $0.03 - 0.06cm^{-}1$, μ_s' : $8 - 12cm^{-}1$	Requirement	5
	μ_a : $0.03 - 9cm^{-}1$, μ_s' : $8 - 16cm^{-}1$	Wish	2
Tunability of acoustic properties	Recipes available in literature to tune for the required ranges	Wish	4
Tunability of optical properties	Recipes available in literature to tune for the required ranges	Wish	4
Speckle formation	Fully developed [25]	Requirement	5
Long-term stability [14]	> 6 months with usage	Requirement	4
	Indefinite	Wish	2
Reproducability [14]	Deviations when repeating protocol within tissue realistic ranges	Requirement	4
Ease of fabrication	Straightforward	Wish	2
	Within 1 day	Wish	2
Price	< 1000 euros	Requirement	3
	<100 euros	Wish	1
Safety	Non-toxic in fabrication and handling	Wish	1
Realistic architecture	Fat and fibroglandular layers	Requirement	5
	Mimicking digital phantom in number of tissues and resolution	Wish	2

3.2 Potential materials

Phantoms are composed of tissue-mimicking materials (TMMs) that are mimicking essential tissue properties for the imaging modality it is intended for. These phantoms are both commercially available and for research purposes only, with the majority being simple phantoms. Simple phantoms consist of a homogeneous base material with targets embedded inside to perform characterization measurements. When a phantom consists of more heterogeneous structures that are more accurately mimicking the organ, it is called an anthropomorphic phantom. [22] Again a certain material forms the basis of these phantoms, however multiple material compositions are used to mimic different tissue types arranged in a more complex geometry. Based on these base materials the phantoms reported in literature are subdivided several categories which are discussed below. Only materials having the most potential for fabricating photoacoustic breast phantoms and are therefore also most commonly used in this field of research, are discussed. For a view on other materials one is referred to the reviews by Culjat *et al.* [22] and Pogue and Patterson [49] on acoustic and optical phantom materials, respectively. In general it is more challenging to find a base material with appropriate acoustic properties than tuning the optical properties of the TMM by adding some extra ingredients. In this section the focus lies therefore on the acoustic properties mainly, accompanied by other advantages and disadvantages of each material type.

3.2.1 Gelatin-based tissue substitutes

Gelatin is a homogeneous colloid gel, which is derived from collagen in animal tissues. General protocol for preparing gelatin phantoms is to heat an aqueous gelatin solution to a temperature that it becomes liquid (35-40 °C for animal gelatin), add additives to increase absorption or scattering and cool it down to cause cross-linking among collagen fibers such that the gelatin mixture solidifies. To prevent the formation of air bubbles the solution is degassed during the process. [50] To increase the speed of sound often alcohol is added before heating, while preservatives can be added to protect against bacterial invasion. With such a protocol speed of sound values between 1480 and 1650 m/s could be achieved. Acoustic attenuation was reported as a range between 0.2 and 1.5 dB/cm at 1 MHz. [50–54] Acoustic attenuation can be increased by increasing the number of scattering particles. Optical properties can be tuned by adding the correct amount of additives. The advantages and disadvantages of gelatin as TMM are given below:

- Advantages gelatin
  - High stability over a period of four months when stored properly [22]
  - Low costs [52]
  - Straightforward fabrication protocol [52]
  - Largely optically transparent [14]
  - Can be non-toxic depending on additives used [22]
- Disadvantages gelatin
  - Not possible to obtain SoS values lower than SoS water
  - Difficulty in achieving uniform distribution of scatterers [22]

  - Susceptible to microbial invasion [22]
  - Instability with temperature variations [22]
  - Limited re-use capability [14]
  - May suffer from dehydratation [22]
  - Water-soluble dyes need encapsulation [13]

3.2.2 Agar-based tissue substitutes

According to litearture, agar-based materials are most widely used to fabricate tissue mimicking phantoms. Agar is a polysaccharide gel that is obtained from algae. Typically the process of fabrications consists of mixing water with propanol and heating this mixture, after which agarose is added. At this point additives such as evaporated milk for attenuation and preservative are heated seperately and added to the mixture. [22] This mixture can then be poured into a mould, where it can solidify upon cooling. Another possibility is for all components to be mixed together, after which it is heated and finally poured into the mould. This is the procedure used by Cannon *et al.* [55] who characterised the acoustic properties of different compositions of the material. This results in a speed of sound range of 1490 to 1570 m/s and attenuation coefficient from 0.1 to 0.9 dB/cm/MHz. The availability of such a detailed recipe for acoustically tuning the phantom is one of the main advantages of agar as TMM. Besides, the phantom can be tuned for the optical properties as well.

- Advantages agar
  - Well characterised acoustic properties for different TMM compositions [55]
  - Ease of fabrication [22]
  - Largely optically transparent [14]
  - Can be non-toxic depending on additives used [22]
- Disadvantages agar
  - Not possible to obtain SoS values lower than SoS of water
  - Susceptible to microbial invasion [22]
  - Limited re-use capability [14]
  - May suffer from dehydratation [14]
  - Water-soluble dyes need encapsulation [13]

3.2.3 Oil gel-based tissue substitutes

Oil gel-based materials are relatively new as phantom materials. As the name suggests it consists of a mixture of some kind of oil with a gelatin-type material. Kondo *et al.* [56] fabricted two types of TMM with different oil-gelatin proportion, resulting in SoS values of 1480 and 1580 m/s, and attenuation coefficients 0.4 and 1.8 dB/cm/MHz. In another study by Madsen *et al.* [57] a TMM was produced which consists of dispersions of oil droplets in solid aqueous gelatin. In this procedure an emulsion of hot liquid aqueous gelatin with safflower oil and surfactant is fabricated, after which cross-linking formaldehyde is added and the emulsion is cooled and can be poured into a mould to solidify. Recipes of different materials for mimicking certain breast tissue types are given

and those materials are acoustically characterised. SoS values range from 1490-1560 m/s and attenuation from 0.1-0.5 dB/cm/MHz. Long-term stability (15 months) on the properties has been reported. [57] It is however not known what materials for optically tuning the TMM are available.

- Advantages oil-gel
  - Well tunable acoustic properties [57]
  - Recipes available for producing TMMs mimicking different breast tissues [57]
  - Stability over a 15-month period [57]
  - Immunity to bacterial infection [22]
- Disadvantages oil-gel
  - More complex protocol for fabrication
  - Less information available in literature compared to other TMM base materials
  - Not known if SoS values lower than that of water are possible to obtain

3.2.4 Polyvinyl alcohol-based tissue substitutes

Polyvinyl alcohol (PVA) is a synthetic polymer and has been used as a TMM within BMPI [58, 59], but was also used by other groups. [60–62] Preparation of the PVA hydrogel requires a number of freeze-thaw cycles applied to a PVA-water solution to enhance cross-linking between the polymer chains. The phantom properties depend on specifications of the hydrogel fabrication process, like PVA concentration in the solution, number of freeze-thaw cycles, duration of freeze-thaw cycles and additives added to the solution. [58, 63] Using the protocol reported by Kharine *et al.* [59] breast tissue mimicking acoustic and optical properties were obtained, with a speed of sound ranging between 1560-1580 m/s and acoustic attenuation between 0.1-0.6 dB/cm/MHz. [58, 59, 62] Whilst optical properties and acoustic attenuation could be tuned by adding additives to the base material, this tuning possibility for speed of sound values is not well known. By altering the water content in the solution the SOS could be lowered to values closer to that of water, but this range is limited. This presents a first disadvantage of PVA as TMM for the heterogeneous phantom. Other advantages and disadvantages of the material are:

- Advantages polyvinyl alcohol (PVA)
  - Tunable intrinsic μ_s', by changing number of freeze-thaw cycles
  - Greater longevity and structural rigidity than agar and gelatin phantoms [14]
  - Low costs [22]
  - Can be non-toxic depending on additives used [60]
- Disadvantages polyvinyl alcohol (PVA)
  - Long preperation time, multiple 24-h freeze-thaw cycles
  - Small range of SOS values
  - Sensitive to humidity [22]
  - Inhomogeneities due to differential heating and cooling rates [58]

3.2.5 Silicone polymer-based tissue substitutes

Silicone materials have been suggested as TMM for soft tissues, mainly due to its high stability and durability against rough handling. [22, 64] Besides it can easily be shaped into an arbitrary solid. One of the silicon materials used in fabricating phantoms is polydimethylsiloxane (PDMS), which can be moulded by soft lithography. Main disadvantages of silicon materials, and thus also for PDMS are the relatively low speed of sound and high acoustic attenuation coefficient. PDMS SoS values were reported as 1300 m/s [64], while another study showed a two-component silicone to have a speed of sound of 1030 m/s and acoustic attenuation being 2-3 dB/cm/MHz [62]. Optical properties of the PDMS are well tunable. [64]

- Advantages silicone
  - High stability [22]
  - High durability against rough handling [64]
  - Easily shaped into 3D solids [62,64]
  - Well-tunable optical properties [64]
  - Non-toxic during preparation and application [62]
  - Ease of fabrication
  - Insoluble in water [14]
- Disadvantages silicone
  - Low SoS values [22]
  - High acoustic attenuation [22]

3.2.6 Polyvinyl chloride plastisol-based tissue substitutes

Commercial polyvinyl chloride plastisol (PVCP) is a plastic commonly used for making fishing lures. It is a white opaque oil-based liquid consisting of monomeres that polymerizes while heated to 190°C, becoming an optically transparent liquid gel. It solidifies when it is allowed to cool. [65] Commercial PVCP is provided into multiple stiffnesses, with softeners and hardeners available to alter the material's stiffness. It was first characterised by Spirou *et al.* [65] and later also by Hungr *et al.* [66] and Fonseca *et al.* [14]. The last two characterizing different PVCP stiffnesses. Hungr *et al.* [66] presented a large range of SoS values for the different materials, being between 1360 and 1580 m/s, while others measured a speed of sound of around 1400 m/s. Acoustic attenuation is reported to be within the range of 0.5-2 dB/cm/MHz. [14,65] In other studies conducted by Vogt *et al.* [12, 24] a slightly different approach to fabricate PVCP phantoms was taken. PVCP was custom-made by resolving PVC resin into a mixture of plasticizers and heat stabilizer. After this, similar as in the protocol described earlier [65] additives may be added and the material is heated, after which it is poured into the mould to solidify. Due to extra steps of adequate mixing and degassing this process takes longer and is more expensive due to higher costs of plasticizers compared to commercial PVCP components. It is however very well characterised for multiple compositions of the material [24] and recipes for obtaining certain breast tissue mimicking materials are given. [12] SoS values obtained range from 1380 to 1570 m/s, while acoustic attenuation is reported

as 0.2-7 dB/cm/MHz depending on frequency and exact composition. Optical absorption is in all these studies increased by adding black plastic colouring (BPC), while acoustic backscattering and optical scattering is induced by adding glass microspheres and TiO_2 respectively.

- Advantages PVCP
  - High stability [24,65]
  - Well-tunable optical properties [24]
  - Non-toxic commercial material [65]
  - Insoluble in water [65]
  - Well tunable and high range of acoustic properties [24]
- Disadvantages PVCP
  - Toxic plasticizers in custom material
  - Slightly higher acoustic attenuation than tissue [14]
  - Non trivial preparation [14]
  - High temperatures needed (190 °C) [65]
  - More expensive custom material

In section 3.4 all these materials are scored on the requirements and wishes that were defined earlier in section 3.1.

3.3 Potential fabrication techniques

The fabrication technique determines the complexity that can be reached regarding the phantom. Therefore, an overview of interesting techniques is given which may present some opportunities for fabricating the photoacoustic breast phantom. This section is subdivided into multiple subsections, each discussing a method for fabrication, reaching from basic casting techniques to newer methodologies of 3D printing or dissolving moulds. [13,67] It is important to note that not all materials mentioned in section 3.2 can be used in combination with all fabrication techniques.

3.3.1 Casting in moulds

Several studies reported on the usage of moulds to shape a TMM. [12,13,57,64,66,68–70] The complexity of the mould depends of course on the complexity and shape of the phantom. Moulds can be made from a wide variety of different materials, but have to be suitable to use together with the TMM. They range from simple trays to very complex blood vessel structures. Different moulding-pouring techniques are discussed below based on phantoms described in literature.

Casting in basic moulds

Basic phantoms consisting of one or more layers of a material in a straightforward geometry are made by using one basic outer mould. These moulds are often used for fabricating

test objects to acquire the imaging system's characteristics or are used to fabricate homogeneous phantoms that mimic tissue in a simplified way. [13, 54, 64] With these basic moulds it is often also possible to pour in multiple layers of TMM, which gives the possibilty to insert targets at a specific location in the phantom or to produce multi-layered phantoms. [13]

Using negative moulding to shape phantom

This type of moulds has an increased complexity over the basic moulds described in the previous paragraph. To produce a phantom using negative moulding two moulds are needed: an outer and an inner (negative) mould. The material is poured in between the outer and inner moulds such that the material adopts the shape of both moulds. It is also possible to make a multi-layered phantom with this method by pouring a second material inside the first material once the inner mould is released. This principle is schematically visualised in figure 3.1.

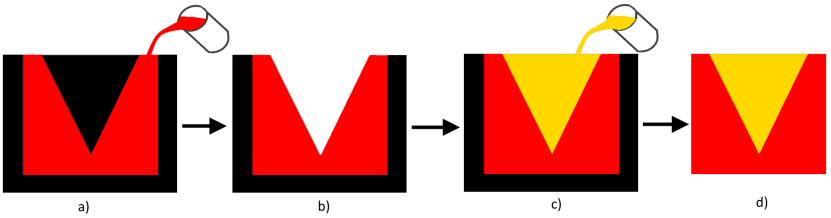

Figure 3.1: Principle of negative moulding visualised. In black the moulds are indicated and in red and yellow the two phantom materials are visualised. a) The first material is poured in the gap between inner and outer mould. b) The inner mould is released once the first material has solidified. c) The second material is poured into the hole in the first material. d) The two-layered phantom is released from the outer mould.

Examples of such negative moulding systems are found in multiple studies. [12, 57, 66, 68–70] The negative mould can consist of a layer mimicking the shape of the boundary between different tissue types [12,57,68] or the phantom mimicks a volume in which a fluid is present, making the contour of the mould the boundary of this liquid filled volume. [70] Another possibility is for an inner phantom structure to be fabricated, which acts as negative mould for the surrounding TMM. [66, 69] Madsen *et al.* [57] and Jia *et al.* [12] have fabricated two phantoms mimicking breast tissue. Both these studies mimicked the boundary of fat and fibroglandular tissue by using a negative mould with a bubbly shape. The first used polyethylene sheets which were formed in the correct 3D geometry (figure 3.2a-b), while the second used an undulating plate to fabricate a two-layer box-shaped phantom (figure 3.2c-d).

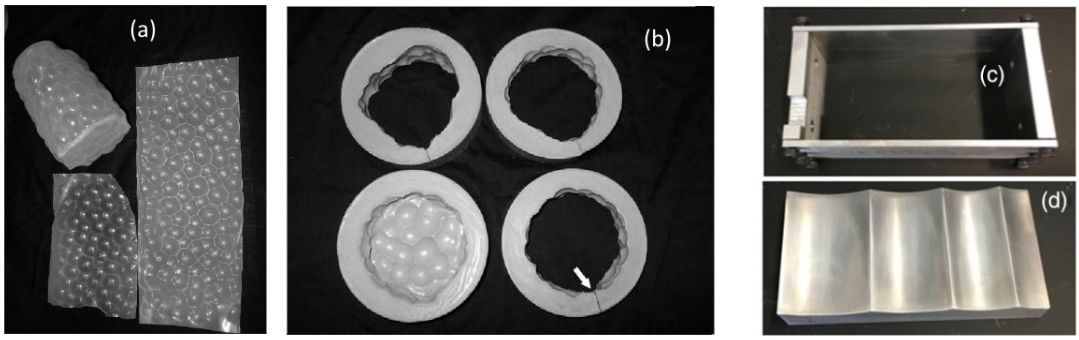

Figure 3.2: Examples of negative moulding systems. (a) and (b) silicone mould sections and polyethylene sheets to fabricate a two-layered 3D breast phantom [57]. (c) and (d) aluminium mould with undulating plate to fabricate two-layered heteregeneous phantoms [12]

3D printing more complex moulds

In recent years 3D printing has gained an increased popularity, which is also seen in the fabrication of phantom moulds. The technique has a large freedom in designing specific structures, with high reproducability and the possibility to share these designs electronically. A few examples of using 3D printed structures as mould for fabricating phantoms are available in recent studies. [68, 70, 71] 3D printing is used by Arconada-Alvarez *et al.* [71] to design a mould for a homogeneous phantom with fluid filled tubes in it, while Maneas *et al.* [70] uses the technique for negative moulding to create a more complex phantom. Further on, our collaborators from the Robotics and Mechatronics RAM group at the UT have designed a 3D printed breast mould set to fabricate a two-layered phantom with an outer skin mimicking stif layer and an inner general breast tissue mimicking volume.

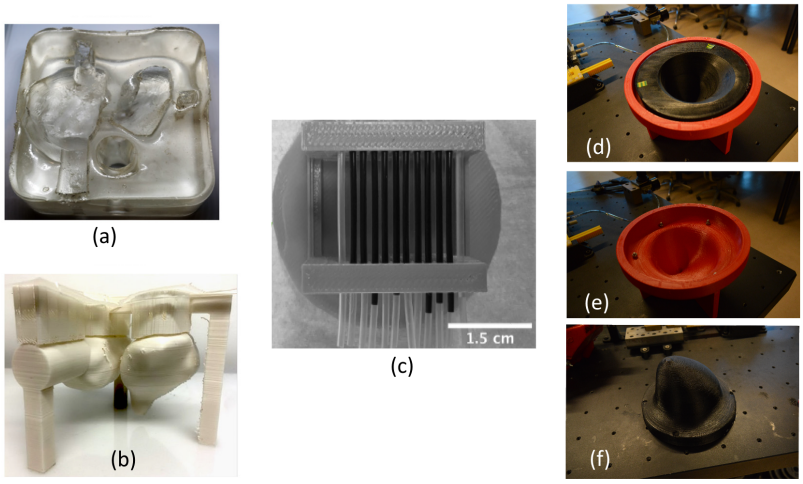

Figure 3.3: Example of 3D printed moulds to fabricate more complex phantoms. (a) and (b) are respectively a cardiac phantom and its inner mould [70]. (c) is a 3D printed mould for fabricating a phantom with tubing [71]. (d), (e) and (f) show a set of inner and outer mould for fabricating a two-layered breast phantom, produced at RAM

3.3.2 Releasing phantom from mould(s)

One of the problems regarding the application of more complex geometries in TMMs is releasing it from the mould. Some solve the problem by creating multiple moulding parts that can be attached to each other while pouring, and are released after the material has solidified. [57, 68] This methodology is however limit to the phantom complexity, since highly anthropomorphic phantoms would require too many components, making the process too complex and time-consuming. Another solution to remove the mould from the phantom is by dissolving it in a solution that does not harm the TMM or by melting the material. [72] With the latter one has to take into account the highest temperature the TMM can be exposed to. For problem-solving strategies like these suitable materials could be soluble 3D-printable materials like polyvinyl alcohol (PVA).

3.3.3 3D printing phantom

One of the newest developments in the field of tissue mimicking phantoms is 3D printing the phantoms themselves, differing from the previous paragraph in which the phantom was made of a pourable material and the moulds were 3D printed. 3D printing the phantom has been used for other imaging modalities, like x-ray imaging systems [67, 73] and microwave tomography. [74, 75] No (photo)acoustic 3D printed TMMs exist yet and the acoustic and optical properties of 3D printed materials have not been reported either. Available 3D printed phantoms differ from relatively simple to being highly anthropomorphic with resolutions $< 200\mu m$ [67, 73–75], producing a phantom as shown in figure 3.4. Main disadvantages of the technology are however the high costs when printing large volumes and small choice of materials to tune the acoustic and optical properties.

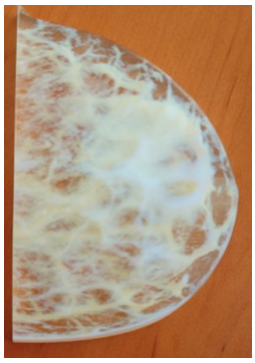

Figure 3.4: A 3D printed sliced breast phantom suitable for x-ray imaging systems. It was printed using an Objet350 Connex printer from Stratasys, which cana print two materials simultaneously. [67]

3.4 Conceptualisation

Three concepts are developed for the process of fabricating a semi-anthropomorphic phantom without blood vessels. They are extracted from the described fabrication techniques.

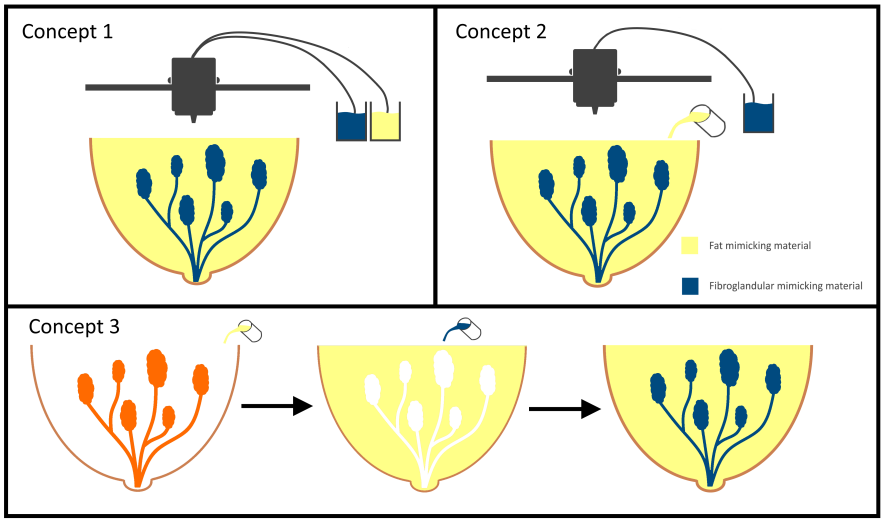

Figure 3.5: Schematic representation of the three developed concepts. Concept 1 consists of only 3D printing the phantom, in concept 2 a combination of 3D printing and pouring the phantom is used and in concept 3 the phantom is fabricated by pouring only. The blue colour indicates fibroglandular tissue, while the yellow indicates adipose tissue. These materials are surrounded by a skin mimicking layer

In figure 3.5 the three concepts are schematically visualised. The first concept is based on fully 3D printing the phantom using a printer that can print a variety of material

compositions in order to tune the properties as described in subsection 3.3.3 . In the second concept a combination of 3D printed and pourable materials is designed. Finally, the third concept consists of 3D printed moulds which are used to shape one of the pourable materials described previously.

The categories of materials that were discussed in section 3.2 are given a score from 1 to 5 on all requirements/wishes. 1 is indicating the requirement/wish is not fulfilled at all, while a 5 shows complete fullfilling of the requirement/wish. NA indicates that the information is not available. For each type of material a total score is given which is defined by the summation of all multiplications of weight with score. If a *not available (NA)* is given as score, a 3 is used to make the calculation for total score.

Table 3.2: Mutiple-Criteria Decision-making Matrix (MCDM) used to score the possible phantom materials on the requirements/wishes that the phantom should fulfill. NA stands for non-available and is assigned a score of 3 for calculating the total score.

Requirement (R) / Wish (W)	**Weight**	**Gelatin**	**Agar**	**Oil-gel**	**PVA**	**Silicone**	**PVCP**	**3D print.**
Range acoust. prop. (R)	5	1	1	4	1	1	5	NA
Range acoust. prop. (W)	2	1	1	2	1	1	2	NA
Range opt. prop. (R)	5	5	5	NA	2	4	4	NA
Range opt. prop. (W)	2	5	5	NA	2	4	4	NA
Recipes acoust. prop. (W)	4	3	5	5	3	1	5	1
Recipes opt. prop. (W)	4	2	2	1	3	2	5	1
Speckles (R)	5	5	5	NA	5	NA	5	1
Stability (R)	4	3	1	5	5	5	5	5
Stability (W)	2	1	1	3	5	5	3	5
Reproducability (R)	4	5	5	3	5	5	5	5
Fabrication: ease	2	5	5	4	4	5	3	5
Fabrication: length	2	5	5	5	1	5	5	2
Price (R)	3	5	5	5	5	5	5	5
Price (W)	1	5	5	5	5	5	3	1
Safety (W)	1	5	5	5	5	5	3	5
2 Layers possible (R)	5	3	3	5	1	5	5	5
Anthropomorphic (W)	2	1	1	2	1	2	2	5
Total Score		**173**	**171**	**185**	**151**	**183**	**219**	**168**

From this table it can be seen that PVCP scores highest of all materials, mainly due to its good scores on tunability and correct acoustic and optical ranges. Oil-gelatin based materials have the second highest score, however there are some characteristics unknown. Silicone scores high mainly due to its ease of fabrication, but the acoustic properties are not in the desired ranges, making it in third place. PVA is in last place, primarily due to its small ranges of acoustic properties and its complex fabrication process. 3D printable materials are the only category of materials that is not pourable, making it unique for its possibilities in reaching high complexities. The acoustic and optical properties of these

materials are however unknown.

3.5 Conclusions

In this chapter the aim was to answer the sub questions: *What are potential materials to use in fabricating the phantom?* and *What are potential fabrication techniques to use for fabricating the phantom?* To answer these question first several requirements/wishes the phantom should fulfill were listed. With these kept in mind an overview of the most common in literature available phantom materials was given. This resulted in six categories for pourable materials: gelatin, agar, oil-gel, PVA, silicone and PVCP, and 3D printable materials. Besides, potential techniques for the fabrication process that were discussed, are generally divided into using moulds to shape the pourable material and 3D printing the phantom. Additional to this some information on techniques on removing the phantom from the mould was provided.

Combining the available materials and techniques results in three concepts for making the anthropomorphic phantoms, either by pouring, 3D printing or a combination of both. Choosing the most suitable concept depends however mostly on the materials available, therefore each group of materials was given a score on the requirements and wishes connected to the end goal of a photoacoustic breast phantom. The material PVCP reached by far the highest score, mainly due to its excellently tunable acoustic and optical properties. Therefore PVCP will be investigated further as TMM for this project. PVCP is subdivided into two types, commercial and custom-made PVCP. Commercial PVCP has the advantage of being cheaper, safer and easier to fabricate. The exact recipe and characterisation of custom PVCP is however further developed. Therefore both types will be tested for their suitability as phantom material.

Although 3D printable materials scored relatively low on the requirements/wishes, these will be investigated as phantom material as well. Using these materials for the first or second concept the complexity that can be reached is a lot higher than by using pourable materials only for the third concept. Besides, since the optical and acoustic properties of these materials are not known yet, this offers the possibility for new and interesting developments. All in all the research question is answered by concluding that one of the three concepts as presented will be used in combination with either the materials commercial PVCP, custom PVCP or 3D printable materials. The ultimate choice depends on the characterisation of the acoustic properties of these three material types.

4 | Acoustic characterisation of candidate materials

From the previous chapter three candidate materials are left: 3D printable materials, commercial PVCP and custom PVCP. In this chapter the acoustic properties of these materials are acquired and evaluated to anser the fourth research question: *Which material is most suitable to use as phantom material?* The chapter starts in section 4.1 with explaining the measurement techniques for determing the acoustic properties of interest. Then the three materials are analysed consecutively in sections 4.2, 4.3 and 4.4, after which the most suitable material is chosen.

4.1 Measuring techniques

The acoustic properties that are characterised of each material are speed of sound, acoustic attenuation, acoustic impedance and speckle formation. The meaurement techniques to obtain these characteristics are described in this section.

4.1.1 Speed of sound & acoustic attenuation

To measure speed of sound (SoS) and acoustic attenuation (AA) a modified insertion technique is used. [76]

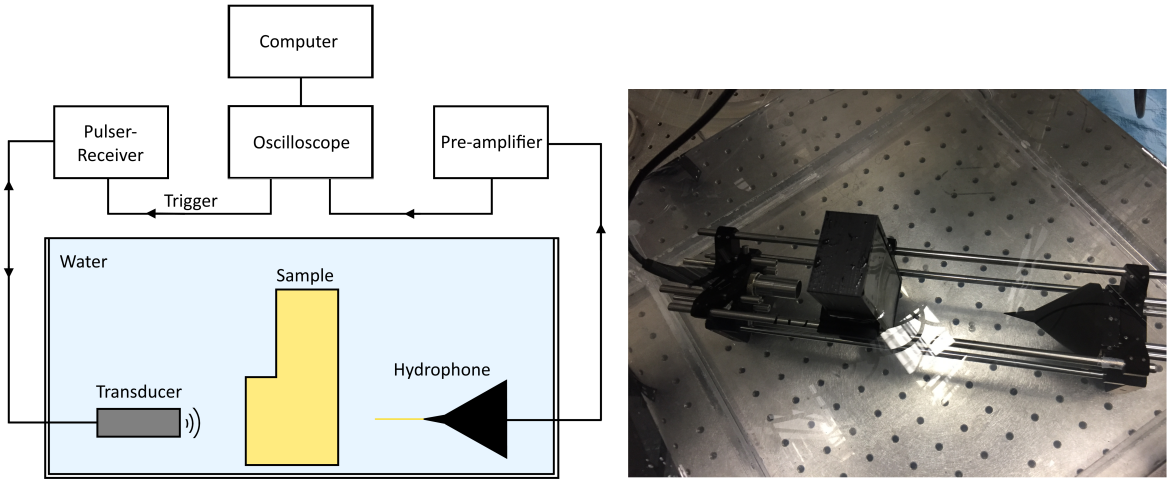

Figure 4.1: Schematic representation and photograph of the setup used to acquire the speed of sound and acoustic attenuation. It consists of a transmitting transducer, receiving hydrophone and a sample with two thicknesses in between. The transducer is driven by a pulser-receiver, while the hydrophone is connected to a pre-amplifier and a scope on the computer.

A schematic representation and a photoagraph of the setup can be found in figure 4.1a and b, respectively. It consist of a transmitting ultrasound transducer, a sample and a receiving needle hydrophone in a water tank. A mercury thermometer was used to measure the water temperature. The transducer is driven by a pulser-receiver, which is connected to the computer for triggering. Three transducers were used; unfocused 1.0 and 2.25 MHz transducers and a focused 5.0 MHz transducer (Panametrics). Two types of hydrophones were used, a 1 mm thick needle hydrophone and a fibre-optic hydrophone (Precision Acoustics). The needle hydrophone was used for measurements on 3D printed materials and was connected to a pre-amplifier (Precision Acoustics). The fibre-optic hydrophone was used for measurements on both types of PVCP and was connected to a fibre-optic hydrophone system such that data could be gathered. In our case the oscilloscope runs on the computer.

The sample has two parts, having different thicknesses to cancel the effects of the acoustic transmission at the boundaries of water-sample and sample-water on the signal's amplitude. This results into equation 4.1 for SoS and equation 4.2 for AA calculations. The symbols in these equations are visualised in figure 4.2.

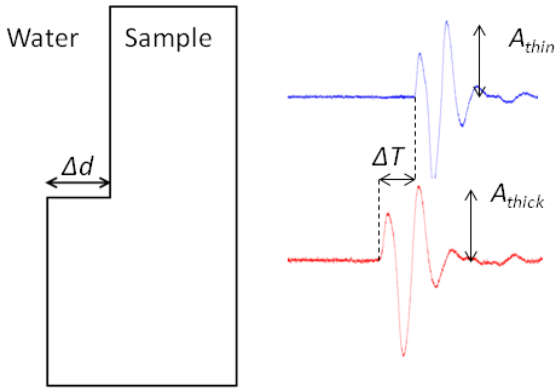

Figure 4.2: Schematic representation of the measured signals and symbols for SoS and AA calculations.

The SoS of the sample (C_s) is calculated using the difference in time-of-flight (TOF, ΔT) between the two signals, the difference in thickness (Δd) between the two parts of the sample and the SoS of water (C_w) at the measured temperature [77]. Because speed of sound is frequency independent, its value is averaged for the SoS acquired using the three transducers.

$$C_s = \frac{\Delta d}{\Delta T + \frac{\Delta d}{C_w}} \tag{4.1}$$

The AA in dB/cm as function of frequency is calculated by using the ratio of amplitudes of both signals in frequency domain ($A_{thick}(\omega)/A_{thin}(\omega)$) and the thickness ($\Delta d$) between the two parts of the sample. The AA of water (α_w) is neglible since it is small compared to the attenuation of the sample. [78]

$$\alpha_s(\omega) = 20\frac{\log(\frac{A_{thick}(\omega)}{A_{thin}(\omega)})}{\Delta d} + \alpha_w(\omega) \tag{4.2}$$

4.1.2 Acoustic impedance

Acoustic impedance (Z) is calculated using equation 4.3. The density (ρ) is determined by dividing the samples weight by its volume. The weight was measured with a balance (M-power, Sartorius) and the volume was determined by measuring the dimensions with a vernier caliper. The SoS is determined through the method described in the previous section.

$$Z = \rho C_s \tag{4.3}$$

4.1.3 Signal analysis

The raw time-signals obtained from the measurements as described before are processed for SoS and AA calculations. To calculate SoS values and from that the impedances, a 6th order Butterworth low-pass filter is applied to the time domain signals (figure 4.3a). The cut-off frequencies are 3, 5 and 10 MHz for the 1.0, 2.25 and 5.0 MHz transducers respectively. With this fiilter frequencies below the cut-off frequency are 100% transmitted, making sure no relevant frequency information is lost. The two times corresponding to the maximum amplitude values in the filtered time signals from the thick and thin sample, are subtracted to end with the difference in TOF. The SoS values of the three transducers are averaged to find the final SoS.

From the raw signal in a time window the fourier transform is taken to find the frequency spectrum. From these spectra the -6 dB bandwidth is determined (figure 4.3b), such that for this frequency range the AA is calculated. This was done for all three transducers. As acoustic attenuation as function of frequency can be described by a power law function (eq. 4.4), this is fitted through the data.

$$AA(f) = af^b \tag{4.4}$$

In which a and b are parameters of the fit and f is the frequency.

An example of these signals in time and frequency domain of a 3D printed sample is given in figure 4.3. Both in time and in frequency domain it is visible that the the acoustic pulse that travelled through the thick part has lower amplitude when detected than the pulse travelling through the thin part. Besides, it can be seen that the speed of sound of this material is higher than that of water, since the pulse travelling through the thick part arrived at the detector earlier than the pulse travelling through the thin part.

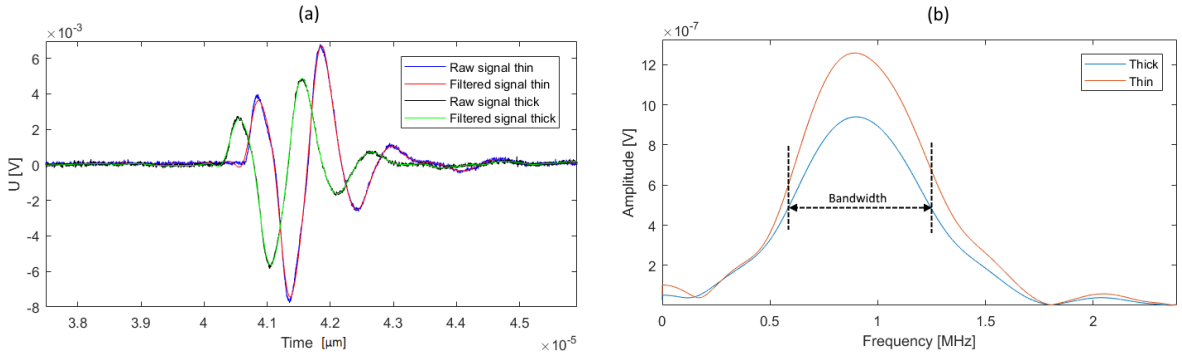

Figure 4.3: Signals from test block FLX9070 in time and frequency domain. (a) Raw and filtered time signals of the pulses travelling through the thick and thin part of the test block. (b) Frequency spectra of pulses travelling through thick and thin part of the test block.

Errors on the SoS values are given by calculating the standard deviation of the SoS measurements for the three different transducers. Standard deviations of the power law fits are also given. Errors in acoustic impedance are the result of both errors in SoS and density.

4.1.4 Validation

To validate the measurement techniques for acquiring the acoustic properties as described above, measurements on perspex (also called acrylic plastic or PMMA) are performed. The results of these measurements and reference values from literature are given in table 4.1.

Table 4.1: Measured and reported values for several acoustic properties of perspex. Literature values were obtained from [76]

Acoustic property	**@ 1 MHz**	**@ 2.25 MHz**	**Literature value**
Speed of Sound [m/s]	2754 ± 23	2761 ± 23	2757
Acoustic Attenuation [dB/cm/MHz]	2.11 ± 0.50	1.38 ± 0.1	1.64
Density $[g/cm^3]$	1.17 ± 0.04	1.17 ± 0.04	1.20
Impedance [MRayls]	3.2 ± 0.3	3.2 ± 0.3	3.27

The measured values shown in this table are comparable to values reported in literature. It can therefore be said that with the described techniques the acoustic properties of materials can be determined accurately.

4.2 3D printable materials

In chapter 3 it was mentioned that 3D printable materials have a potential as phantom material, because of the possibilities to produce highly complex structures using

3D printing. However, the acoustic properties of these materials are not available yet, therefore it is not known what its potential as photoacoustic phantom material is. In this section some materials, printed with the Objet 260 Connex 3, are acoustically characterised. This printer is in the possession of the Robotics and Mechatronics (RAM) group at the UT. The printer has shown its ability to print high resolution heterogeneous breast phantoms. [67] Besides, it is able to print multiple materials consisting of different ratios of two base materials, which opens up possibilities for tuning the acoustic and optical properties within a certain range.

4.2.1 Materials & Methods

The Objet 260 Connex 3 printer makes use of the PolyJet technology. This technology uses printhead nozzles to deposit droplets of a liquid photopolymer onto a build tray and instantly cures them by exposion to UV light. The 3D printer can build volumes with maximum size of 255x252x200 mm and resolutions of 42x42x16 μm. [79]. The materials that can be used in this printer are subdivided into four categories: rigid opaque, rigid transparent, rubber-like and simulated polypropylene. Combinations of these materials can be made to achieve a certain stiffness, colour or transparency. At RAM the following materials are available: VeroWhitePlus (rigid opaque), VeroClear (rigid transparent), TangoBlackPlus (rubber-like) and Agilus (rubber-like). Combinations of these materials were made to perform acoustic characterisation:

- VeroWhitePlus
- RGD8720 (VeroClear and TangoBlackPlus)
- RGD8520 (VeroWhitePlus and TangoBlackPlus)
- FLX9870 (TangoBlackPlus and VeroWhitePlus)
- FLX9070 (TangoBlackPlus and VeroClear)
- TangoBlackPlus
- Agilus

The exact ratios of the primary and secondary materials (between brackets) are not available, because of commercial reasons of the manufacturer.

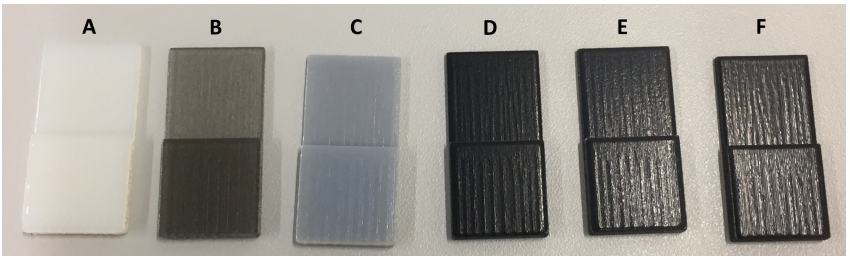

Figure 4.4: 3D printed test blocks for acoustic characterisation. The test blocks have a thick part with dimensions 20x20x4 mm and a thin part having dimensions 20x20x2 mm. **A** VeroWhitePlus, **B** RGD8720, **C** RGD8520, **D** FLX9870, **E** FLX9070 and **F** TangoBlackPlus.

To characterise these materials, test blocks as shown in figure 4.4 were printed. In this figure the Agilus sample is not shown. These test blocks have a thick part with dimensions 20x20x4 mm and a thin part having dimensions 20x20x2 mm. The samples were kept small to keep the amount of material and time needed to print the samples low. From these samples the speed of sound, acoustic attenuation and acoustic impedance were determined.

4.2.2 Results

AA was acquired over a spectral range by using the frequency spectra of the bandwidth of both thick and thin signals, making use of the method described in section 4.1.3. Power law functions were fitted through these data points. The results are shown in figure 4.5. The data is plotted using dots, but show up as a thick line due to the high number of data points. The thin lines are the power law fits through the data. At the 1 MHz transducer frequency region large deviations from power law fit can be seen at the materials VeroWhitePlus, RGD8720 and RGD8520.

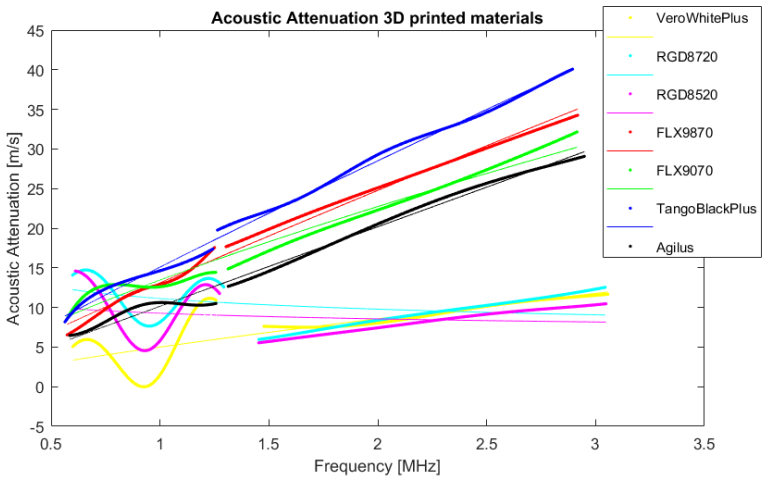

Figure 4.5: Acoustic attenuation with fitted power law functions as function of frequency for seven 3D printed materials.

All the acoustic properties are placed in table 4.2 for an overview. This consists of the average speed of sounds for both frequencies, the variables of the power law functions and the calculated impedances.

Table 4.2: Acoustic properties of seven 3D printed materials.

Material	**SoS**	**Power law function**		**Impedance**
	[m/s]	**a**	**b**	**[MRayls]**
VeroWhitePlus	2579 ± 127	5.00 ± 0.07	0.780 ± 0.017	3.08 ± 0.70
RGD8720	2320 ± 163	11.13 ± 0.05	-0.186 ± 0.010	2.77 ± 0.75
RGD8520	2541 ± 73	9.27 ± 0.06	-0.116 ± 0.014	3.04 ± 0.53
FLX9870	1865 ± 19	13.11 ± 0.02	0.919 ± 0.001	2.23 ± 0.25
FLX9070	1892 ± 40	13.47 ± 0.03	0.756 ± 0.003	2.26 ± 0.34
TangoBlackPlus	1843 ± 5	15.09 ± 0.2	0.918 ± 0.001	2.20 ± 0.15
Agilus	2010 ± 46	10.15 ± 0.02	0.992 ± 0.004	2.40 ± 0.38

4.2.3 Discussion

The speed of sound values measured for all materials are a lot higher than those reported for breast tissue in chapter 2. Besides, acoustic attenuation is also measured being a lot higher than those observed in tissue. However, large variations and disturbances in these results can be seen. Large variations in speed of sound measurements can be seen at different frequencies, although SoS is not highly frequency dependent. Besides, the acoustic attenuation of materials VeroWhitePlus, RGD8720 and RGD8520 determined with the 1 MHz transducer show large variations. One explanation of these fluctuations may be the relatively low signal-to-noise ratio (SNR) measured with the 1 MHz transducer. Another explanation to the variation in SoS and AA may be the setup and dimensions of the test block. The thick and thin parts of the test sample have dimensions only slightly larger than the diameter of the transducer, with the 1 MHz transducer having a larger diameter than the 2.25 MHz transducer. This may have resulted in the ultrasound beam not passing through the sample completely, therefore disturbing the measured signal. Another problem of this small sized sample was the difficulty in placing the sample in the setup. The test block was easily moved, making the travel distance through the material longer and causing discrepancies in calculating the acoustic properties. The more flexible materials (Agilus, TangoBlackPlus, FLX9070 and FLX9870) were more easily placed in the setup due to the fact that they are somewhat sticky.

4.2.4 Conclusion

Despite the large variations and insecurities in the SoS and AA measurements of seven 3D printable materials, there can be concluded that these materials are unsuitable for our goal. The SoS and AA values are a lot higher than reported values in breast tissue.

4.3 Commercial PVCP

In chapter 3 it was seen that PVCP scored highest of all potential phantom materials. Two types of PVCP are available; commercial and custom. Commercial PVCP is easier and cheaper to fabricate, but there are contradictions seen in the reported SoS values of this material. [24,66] The acoustic properties of different compositions of this commercial PVCP are therefore acquired in this section.

4.3.1 Materials & methods

PVCP is commercially available in several (online) fishing stores and in a variety of types. In this research PVCP soft and PVCP firm (Lure Factors) were used to determine the acoustic properties. Softeners or hardeners can be added to the base material to change the material's stiffness, but these were not used. The test blocks that were formed to acquire the acoustic properties of PVCP commercial are PVCP firm and PVCP soft (shown in figure 4.7):

The protocol for fabricating bubble-free test blocks was optimised, based on the procedure described by Bohndiek *et al.* [13] and is described in detail in appendix C. Briefly, PVCP is heated in an au-bain-marie way, by submerging a glass beaker filled with PVCP into heat transfer fluid (HTF) which is kept at 180-190 °C. Under regular stirring PVCP is heated such that first a transition occurs from a white liquid to translucent gel structure (after about 10 minutes) and then a second transition occurs from this gel structure to a translucent viscous fluid (after another 10 minutes). Then the glass beaker with PVCP is placed in a vacuum dessicator to degas for 5-8 minutes. After this, PVCP is reheated to increase the liquidity again such that it can be poured into the mould.

4.3.2 Mould and holder

The test blocks for both commercial and custom PVCP can be made only by pouring these materials in a predefined mould. The test blocks consist of two parts; a thick and a thin part. The mould should also have these two parts and besides it should be possible to release the test block from the mould. It is therefore decided to design an open cage system, which is transformed to a mould by clamping and glueing stainless steel plates to the sides, such that the plates can be removed after the material has solidified, see figure 4.6. For glueing liquid rubber glue (Bison) is used, which is heat resistant and easy to remove. The design consists of an extra space on top to prevent shrinkage of the material in the measurement volume. The plates can be taken off when the material has solidified to take the test block from the mould. This can then be placed in a 3D printed holder, which can be placed into the setup as was shown in figure 4.1. This holder can be placed in the setup in two ways, such that a measurement is performed through the middle of the thin and thick parts of the sample. The dimensions of the test blocks were set to 14 cm in height, 5 cm in width and 3 and 4 cm in thickness for respectively thin and thick

part. With these dimensions the test blocks remain stable while in upright position in the holder and the samples are still thin enough for sufficient SNR in the acoustic signals.

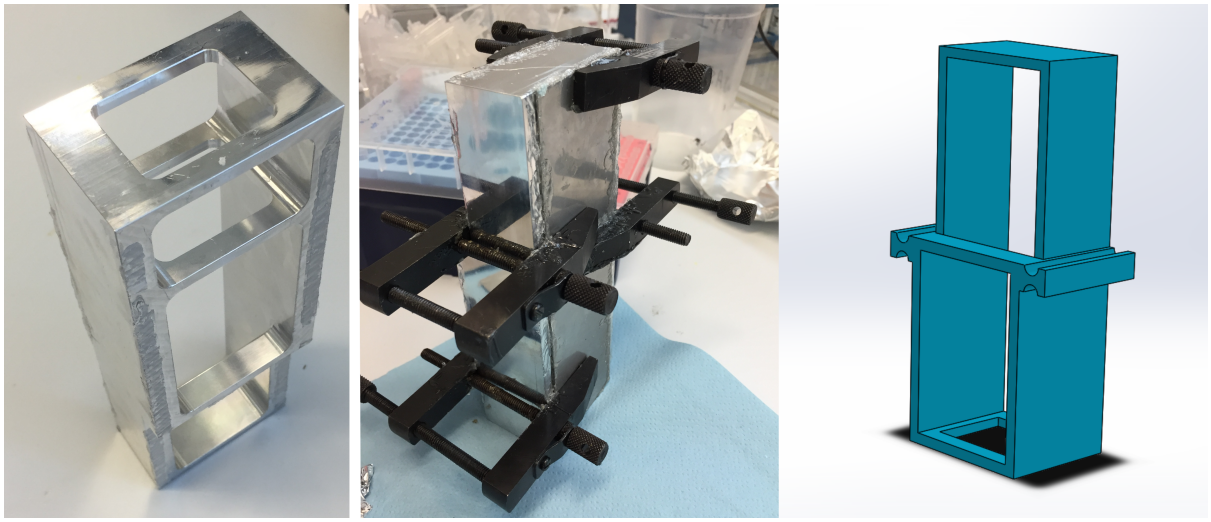

Figure 4.6: Mould and holder for test blocks for acoustic characterization. Left: Mould without plates, Middle: Mould with plates, Right: 3D model for holder

The two test blocks PVCP soft and firm fabricated using the mould are seen in figure 4.7. One of these blocks is positioned in the holder for performing characterisation measurements.

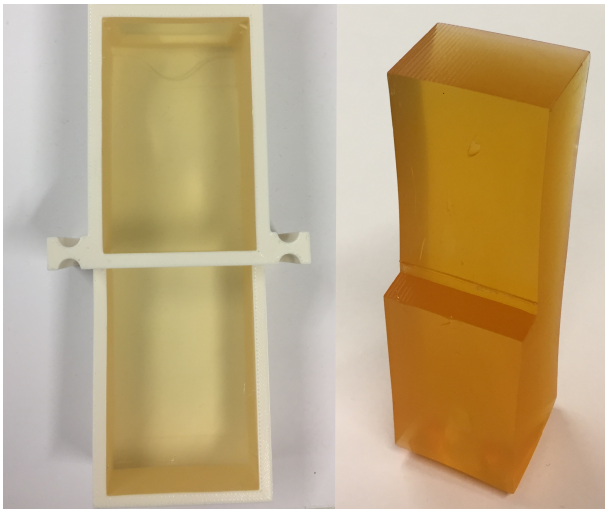

Figure 4.7: Commercial PVCP test blocks soft and firm

4.3.3 Results

In figure 4.8 the measured acoustic attenuations with fitted power law functions of PVCP soft and firm are plotted against frequency. The AA of firm PVCP is a bit higher than

that of soft PVCP. The power law fits follow the data of transducer 2.25 and 5 MHz nicely, while the 1 MHz data are slightly off.

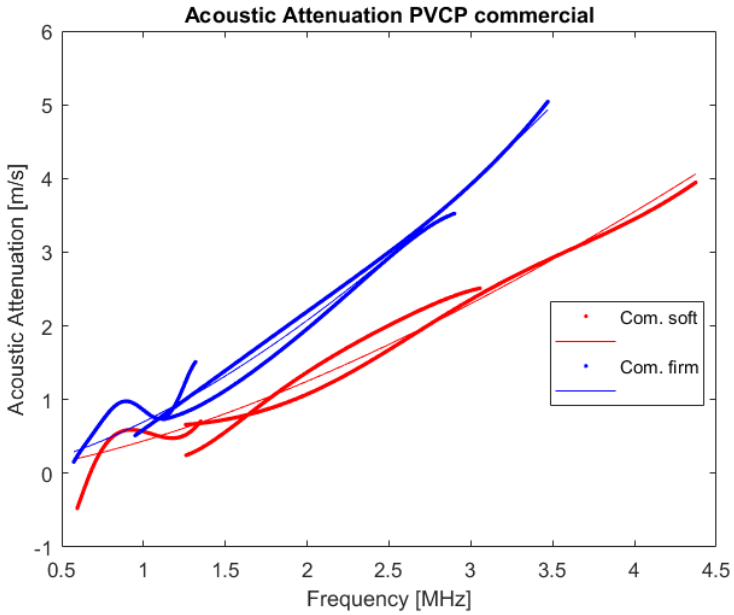

Figure 4.8: Acoustic attenuation with fitted power law functions as function of frequency for two types of commercial PVCP.

In table 4.3 the acoustic properties of the two types of commercial PVCP are summarized. This includes the average SoS values, power law functions fitted to the AA data and the impedances calculated from the density and SoS.

Table 4.3: Acoustic properties of custom PVCP test blocks.

Material	**SoS**	**Power law function**		**Impedance**
	[m/s]	**a**	**b**	**[MRayls]**
Soft	1396 ± 2	0.44 ± 0.01	1.51 ± 0.01	1.39 ± 0.52
Firm	1403 ± 3	0.70 ± 0.07	1.57 ± 0.01	1.42 ± 0.54

4.3.4 Discussion

As can be seen in figure 4.7 the firm test block turned out quite yellow/orange. This means the material burned during preparation. The heating of this test block took a lot longer than usually needed according to the protocol. Besides, the material was more firm than earlier processed firm PVCP samples. This is probably, because this test block was fabricated from the last bit present in the bottle in which it is stored. This bottle needs to be shaken very well before processing the material. It is possible this shaking was not always done properly and more firm material sank to the bottom. This is also one of the problems in using PVCP commercial, since the material composition does not remain exactly the same when using different volumes of the bottle.

4.3.5 Conclusion

The acoustic attenuation values of this commercial PVCP are suitable for mimicking tissue, since it is low enough and possibilities to add additives are available. However, the speed of sound is not comparable to tissue values. The values lie around 1400 m/s which is lower than breast tissue. Since both soft and firm materials have similar SoS, it seems not possible to tune this value using the commercial materials used. Other commercially available PVCP may have slightly different acoustic properties. Besides, it could be possible to tune these properties further by adding plasticizers to the base PVCP. However, tuning will not be possbile over very large SoS ranges.

4.4 Custom PVCP

In this section the other type of PVCP, custom PVCP, is characterised. The fabrication protocol of this material is more complex than commercial PVCP, but it is well-characterised in literature. [12, 24]. Based on these reported recipes and characteristics the different compositions of PVCP are investigated.

4.4.1 Materials & methods

Custom PVCP is a solution of PVC resin and a (combination of) plasticizer(s). Vogt *et al.* [24] tested different plasticizers, concentrations of PVC resin and glass microspheres on their effect on the acoustic properties. Combining that study with the acoustic properties of the female breast it is decided to use PVC resin (Geon 121A, Mexichem Specialty Resins), benzyl butyl phthalate (BBP, Sigma-Aldrich), di(2-ethylhexyl) adipate (DEHA, Sigma-Aldrich) and glass beads (unwashed, $< 106\mu$m, Sigma-Aldrich) for fabricating custom PVCP test blocks. The plasticizer combination of BBP and DEHA is well characterised and able to achieve a wide range of SoS values within the range of breast tissue values.

The test blocks that are fabricated to characterise custom PVCP are chosen to acoustically mimic fat and fibroglandular breast tissue using the compositions as given in table 4.4:

Table 4.4: Compositions of acoustic test blocks for characterization of custom PVCP.

Sample	**DEHA v/v**	**BBP v/v**	**Heat stabilizer v/v**	**PVC resin m/m**
Fat	57.4%	41.6%	1%	8.4%
Fibroglandular	-	99%	1%	10%

To fabricate a custom PVCP test block a detailed protocol is given in appendix D. Briefly, a PVCP solution is prepared by mixing a plasticizer (mix) with 1% v/v calcium-zinc heat stabilizer (M-F Manufacturing Co.). Then PVC resin is added and dissolved by first manually stirring and then magnetic stirring for 30 minutes. After this the solution

is degassed for 60 minutes. Then PVCP is heated similarly as for commercial PVCP, after which it is poured into the mould.

4.4.2 Results

The measured AA for both test blocks is plotted against frequency in figure 4.9. Power law fits are plotted with these data points. The AA of the material with fibroglandular material is higher than that of the fat mimicking material. Especially with the latter, the data points do not follow the fit that well.

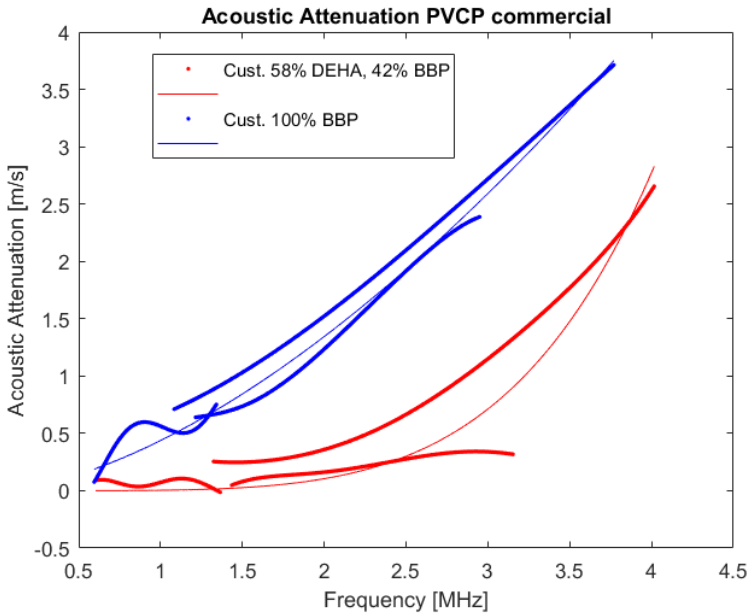

Figure 4.9: Acoustic attenuation with fitted power law functions as function of frequency for two types of custom PVCP.

In table 4.5 the acoustic properties of the two types of custom PVCP are summarized. This includes the average SoS values, power law functions fitted to the AA data and the impedances calculated from the density and SoS. The SoS of the material with BBP only is around 1510 m/s, while the value of the material with both plasticizers is a lot lower, lying between 1430-1440 m/s.

Table 4.5: Acoustic properties of custom PVCP test blocks.

Material	**SoS**	**Power law function**		**Impedance**
	[m/s]	**a**	**b**	**[MRayls]**
Fat	1433 ± 3	0.004 ± 0.0004	4.73 ± 0.09	1.59 ± 0.09
Fibroglandular	1508 ± 1	0.44 ± 0.004	1.62 ± 0.01	1.76 ± 0.07

4.4.3 Discussion

The acoustic attenuation of the fat mimicking material is that low at low frequencies that it is difficult to fit an accurate power law function through this data. This may be due to the SNR that became too low in these low-frequency signals to accurately determine the AA for these frequencies. Using a more sensitive detector or larger difference in sample thickness may overcome these problems for future characterisation.

4.4.4 Conclusion

The materials with these SoS and AA are well suitable for mimicking different breast tissues. The AA is low enough such that additives can be added to tune these values to tissue realistic values. The SoS results show that the material is well tunable and suitable to mimic fat and fibroglandular breast tissue.

4.5 Conclusions

In this chapter the following research question is answered: *Which material is most suitable to use as phantom materials?* The candidate materials, 3D printable materials, commercial PVCP and custom PVCP are acoustically characterised for the properties speed of sound, attenuation and impedance. These characteristics showed that 3D printed materials are not suitable for mimicking breast tissue in photoacoustic imaging since both the SoS and AA are too high. Commercial PVCP shows usable AA values, but the SoS is too low and probably not tunable towards tissue realistic values. This leaves custom PVCP, which has well tunable SoS properties in the range of breast tissue and AA values that are low enough to add additives to tune it towards desired values. Therefore, custom PVCP with plasticizers BBP and DEHA is further tuned towards materials that are mimicking fat and fibroglandular tissue on both acoustic and optical properties. From these materials, the photoacoustic breast phantom is then fabricated.

5 | Optimising material properties for PAT

In this chapter the fifth research question is answered: *How can this material be optimised for the acoustic and optical properties?* From the previous chapter it was concluded that PVCP custom is most suitable to use for the photoacoustic phantom. Optimisation of this material is described in this chapter. This consists mainly of adding additives to tune the acoustic and optical properties towards tissue realistic values. Acoustic optimisation is described in section 5.1 and optical optimisation is explained in section 5.2.

5.1 Acoustic optimisation

In the previous chapter the acoustic properties of the base material of PVCP were acquired. Compared to literature values, both SoS and AA are lower in these samples. Besides, acoustic speckle still needs to be added to the material.

A higher SoS is obtained when the ratio of BBP/DEHA and/or when the PVC resin concentration is increased. Since these values also influence the AA, a balance on the correct concentrations should be found. [24]

Acoustic speckle occurs due to constructive and destructive interference of US signals by sub-resolution sized scatterers. When speckle is fully developed, pure diffusive scattering takes place, which decreases image resolution and contrast. [80] Acoustic speckle is fully developed when at least 5 scatterers per resolution voxel are present in the material. The signal-to-noise ratio (SNR) at which this happens is 1.91. In this case received echo is a random signal of which the histogram of the envelope amplitude follows a Rayleigh distribution. [25] If the SNR < 1.91 speckle is not fully developed an is termed pre-Rayleigh. When amount of scatterers per resolution voxel is increased higher than five, the histogram is shifted to a Rician distribution with high SNR. [25] It is important for speckle to be fully formed in the fat and fibroglandular layers of the phantom. Glass beads (Sigma-Aldrich) are therefore added to induces acoustic speckle.

The acoustic attenuation also increases by adding US scatterers. [24] Therefore this property is also characterised based on the developed test samples in this section. The focus will however lie on inducing fully formed speckle.

5.1.1 Materials & methods

To check at what concentration glass acoustic speckle becomes fully developed, acoustic test blocks embedded with different glass beads concentrations are fabricated according to the protocols described in appendices C and D. These test blocks consist of two types: PVCP commercial and PVCP custom. Commercial PVCP blocks were made to decrease

fabrication costs and time. The compositions of the four test blocks are found in table 5.1.

Table 5.1: Compositions of acoustic test blocks for acoustic speckle analysis.

Sample	**DEHA v/v**	**BBP v/v**	**Heat stabilizer v/v**	**PVC resin m/m**	**PVCP soft v/v**	**Glass beads mg/mL**
Fat2	57.4	41.6%	1%	8.4%	-	2
Soft10	-	-	-	-	100%	10
Fibro30	-	99%	1%	10%	-	30
Soft50	-	-	-	-	100%	50

Of these test blocks reflection mode US signals were acquired using the setup as was shown in figure 4.1. Echo signals of the speckle patterns were obtained using an unfocused 2.25 MHz transducer (Panametrics). The speckle signals were acquired by taking a time window in between the first front and back reflection of the sample. The envelope of this echo was taken, after which the envelope amplitude was transformed into a histogram. A Rayleigh distribution was fitted on this data, through which it was determined if the SNR was either lower than, equal to or higher than 1.91.

To check whether the average speckle intensity in these samples is conform tissue realistic values, B-mode images were made of three samples. For these images sample Soft10, Soft50 and an extra fabricated sample Soft2 were used. An ROI within these images was taken of which the average speckle intensity was determined. Besides the average speckle intensities in two ROIs corresponding with fat and fibroglandular tissue in a B-mode image of a female breast were determined. This B-mode image was obtained from an online database. [81] Since these images and thus speckle intensities cannot be compared on to one, the ratio of fibroglandular to fat tissue is calculated, which should be comparable to the ratio of the two TMMs.

Speed of sound and acoustic attenuation of the test samples Fat2 and Fibro30 were acquired using the method described in section 4.1. The obtained values are compared with the values obtained from the test sample Fat TMM and Fibro TMM from the previous chapter, to see the effect of glass beads on SoS and AA.

5.1.2 Results

An example of the speckle echo and envelope and its histogram with fitted Rayleigh distribution is given in figure 5.1. The analysis of the speckle signal from test block Soft10 is given here. All samples have an SNR > 1.91, therefore the speckle is fully developed at all the concentrations of glass beads.

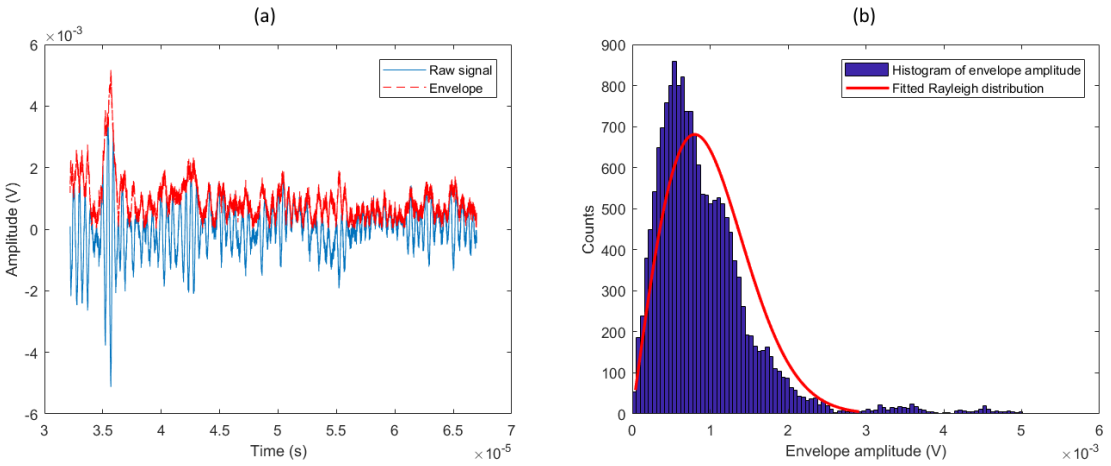

Figure 5.1: An example of the speckle analysis performed using (a) the amplitude envelope of the echo signal and (b) the histogram of this amplitude envelope compared to a fitted Rayleigh distribuiton.

The B-mode images to calculate average ROI intensities are shown in figure 5.2. In these images the ROIs used for calculation are marked with a red box. The ratio of fibroglandular to fat mean intensity is 1.44. The intensities of Soft2, Soft 10 and Soft50 are 0.27, 0.39 and 0.47 respectively. When one looks at the images by eye it seems as if speckle density in fat tissue lies in between the Soft2 and Soft 10 densities. The fibroglandular speckle density seems to lie in between Soft10 and Soft50 densities.

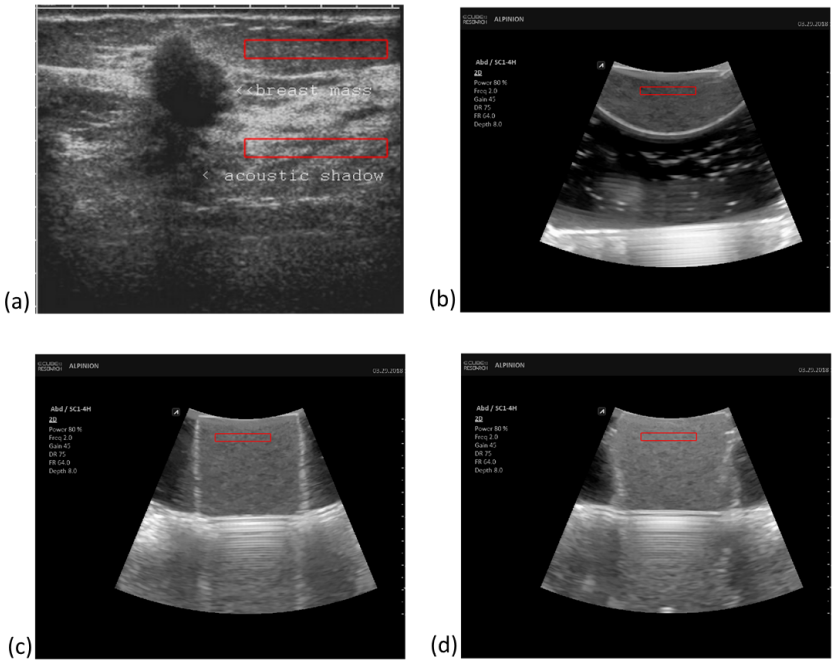

Figure 5.2: B-mode images of (a) breast tissue [81], (b) Soft2, (c) Soft10 and (d) Soft50. The ROIs used to calculate average speckle intensity are marked with a red box.

The acoustic attenuation coefficients of the custom PVCP test blocks and the test blocks from the previous chapter in which no scattering particles were present, are shown in figure 5.3. Fitted power law functions are plotted through the data. In the fat TMM no increase in AA can be seen due to addition of glass beads. However the concentration of glass beads was quite low. The AA of fibroglandular TMM does increase by adding glass beads.

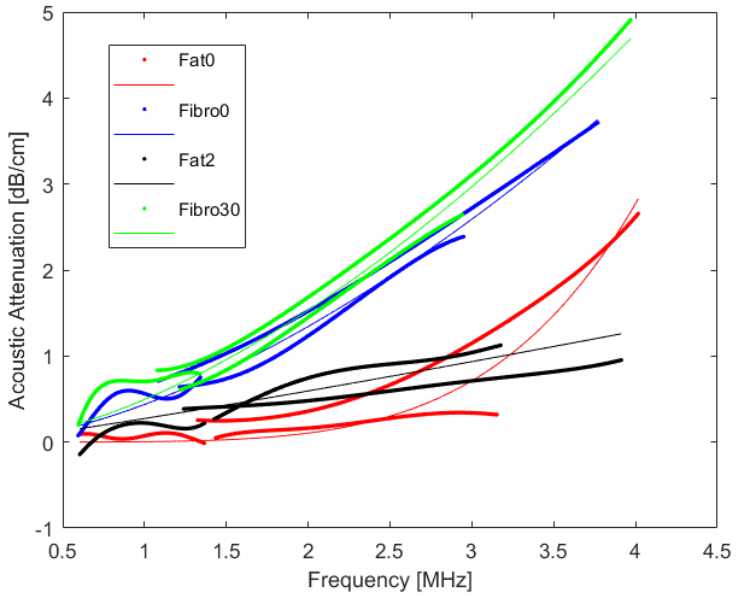

Figure 5.3: Acoustic attenuation plotted as function of frequency with power law function fitted through the data. Four test blocks are characterised, both fat with and without scattering particles.

The acoustic properties of these custom PVCP materials are given in table 5.2. The SoS is not changed much by adding glass beads, while acoustic attenuation is changed in fibroglandular TMM.

Table 5.2: Acoustic properties of custom PVCP scattering test samples.

Material	**SoS**	**Power law function**		**Impedance**
	[m/s]	**a**	**b**	**[MRayls]**
Fat0	1433 ± 3	0.004 ± 0.0004	4.73 ± 0.09	1.59 ± 0.09
Fat2	1437 ± 0	0.27 ± 0.01	1.12 ± 0.02	1.63 ± 0.07
Fibro0	1508 ± 1	0.44 ± 0.004	1.62 ± 0.01	1.76 ± 0.07
Fibro30	1509 ± 3	0.495 ± 0.005	1.63 ± 0.01	1.84 ± 0.07

5.1.3 Discussion

Interpreting the speckle signals based on their envelope amplitude histogram is sensitive to making errors in assesment of the speckle formation. Some histograms seem to lie slightly to the left of the Rayleigh distribution, but SNR values are higher than 1.91,

indicating fully developed speckle. It should also be taken into account that the glass beads may react differently in custom PVCP compared to commercial PVCP, such that direct comparison may be inaccurate.

Differences in acoustic attenuation between the scattering and non-scattering fat samples are difficult to state clearly since the error in fitting is large. For fibroglandular TMM it can be said that AA increases by addition of scattering particles. Speed of sound values do not change by adding glass beads.

5.1.4 Conclusions

For the glass beads concentrations of 2-50 mg/mL fully developed speckle was observed. Besides, the ratio of average speckle intensity in an ROI within fibroglandular and fat tissue is 1.44. Acoustic attenuation increased slightly by addition of scattering particles. The fabricated fibroglandular TMM containing 30 mg/mL glass beads takes on SoS values that are slightly lower than reported literature values, but acoustic attenuation seems to be good. The SoS and AA of fat TMM containing 2 mg/mL glass beads are both lower than literature values, therefore there is still a need to increase both values. When the concentration of 30 mg/mL is used for fibroglandular tissue this would be estimated (by interpolation) in an average speckle intensity of approximately 0.43. To obtain the contrast ratio between fibroglandular and fat tissue, an average speckle intensity of fat TMM should be 0.31 which is estimated (by interpolation) to be the average speckle intensity of a sample with 6 mg/mL glass beads.

5.2 Optical optimisation

The optical properties of PVCP were not characterised in the previous chapter. To tune optical absorption and scattering, respectively black plastic colouring (BPC) and titanium oxide (TiO_2) are added. The concentrations that need to be added to obtain values comparable to breast tissue at 785 nm are based on reported values in literature. [24] In figure 5.4 the absorption and reduced scattering coefficients are plotted against wavelength for a number of phantoms with varying BPC and TiO_2 concentrations.

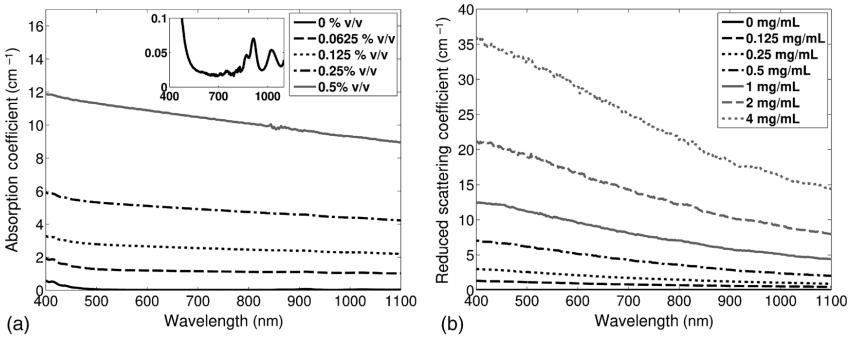

Figure 5.4: Optical properties of phantoms comprised of 75/25% v/v BBP/DEHA and 10% PVC resin according to Vogt *et al.* (a) Optical absorption coefficient versus % v/v BPC. Inset shows the 0% v/v spectrum, with axes in similar units. (b) Reduced scattering coefficient versus TiO_2 concentration. (Reproduced from ref [24])

From these graphs it can be seen that the optical absorption of PVCP is already comparable to the very low optical absorption of fat and fibroglandular tissue at 785 nm, having no need for the addition of BPC. For the same wavelength the reduced scattering coefficient has values in the range of 4-13 cm^{-1} for TiO_2 concentrations of 0.5-2 mg/mL. These μ_s' values are comparable to the values of fat and fibroglandular tissue at 785 nm.

5.2.1 Materials & methods

Measurement technique

To obtain the optical properties μ_a and μ_s' the inverse adding-doubling (IAD) method is used. This method uses an adding-doubling solution of the radiative transport equation by iterating it until the calculated values of reflection and transmission match the measured ones. [82, 83] Using a spectrophotometer with integrating sphere (Shimadzu UV2600) diffuse transmittance and reflectance measurements of PVCP slabs are made over a range of 400 to 1000 nm.

The measurement protocol is obtained from Cook *et al.* [52] Dual-beam measurements are performed in both transmittance and reflectance measurements to minimize system noise. A 2x5 mask is placed in both sample and reference arm to decrease the beam size such that the distance from beam to sample side is as small as possible. The baseline is made by having empty entrance sample and reference ports and having the barium-sulfate ($BaSO_4$) standards at the back side of both beam paths. Then the measurements can be performed according to the overview in figure 5.5. [52]

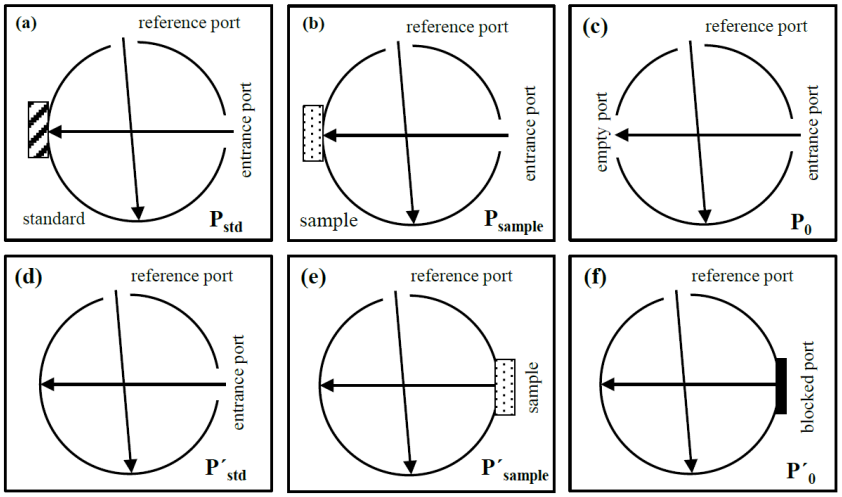

Figure 5.5: Setup and measurements performed for (a-c) total diffuse reflectance and (d-f) total diffuse transmittance measurements of samples to obtain optical absorption and reduced scattering coefficient using the IAD method. (Reproduced from ref [52])

To get the system started first a baseline measurement is performed by placing The total diffuse reflectance (R_{sam}) and transmittance (T_{sam}) are calculated using measurements on the sample (P_{sam}), the standard (P_{std}) and a dark measurement (P_0) according to equations 5.1 and 5.2. The apastrophe indicates transmittance measurements. R_{std} and T_{std} indicate the reflectivity of the $BaSO_4$ test standards which is 0.98.

$$R_{sam} = R_{std}\frac{P_{sam} - P_0}{P_{std} - P_0} \tag{5.1}$$

$$T_{sam} = T_{std}\frac{P'_{sam} - P'_0}{P'_{std} - P'_0} \tag{5.2}$$

These values of R_{sample} and T_{sample} as function of wavelength are used as input for the IAD programme. The programme also needs to have the refractive index (n) and anisotropy (g) of the sample as input. The refractive indices of BBP and DEHA are 1.540 and 1.447, respectively. [24]. The Lorentz-Lorenz mixture rule for refractive index (eq. 5.3) is used to calculate the refractive indices of the optical samples. [84] The μ'_s computed with the IAD programme is relatively insensitive to the value of g. Therefore this value is assumed to be $g = 0.7$ as was determined by Vogt *et al.* based on Mie scattering theory for homogeneous spherical particles. [24]

$$\frac{n_{12} - 1}{n_{12} + 2} = \phi_1\frac{n_1 - 1}{n_1 + 2} + \phi_2\frac{n_2 - 1}{n_2 + 2} \tag{5.3}$$

In which n is the refractive index, ϕ the fraction of a material in the mixture and the subscritps 1, 2 and 12 indicate material 1, 2 and the mixture.

An overview of all settings of the spectrophotometer to measure all optical samples and input parameters for the IAD programme is given in appendix E.

Mould and holder

To measure the optical properties using the spectrophotometer a 1 mm slab of the material is needed. To fabricate this a couple of moulds were developed using spaces in between microscope glasses. This mould can be seen in figure 5.6a. RVS spacers of 1mm in thickness were glued to one microscope glass using liquid rubber glue (Bison). Prepared PVCP could be poured onto this slide, after which a second microscope glass is placed on top and both slides are clamped together.

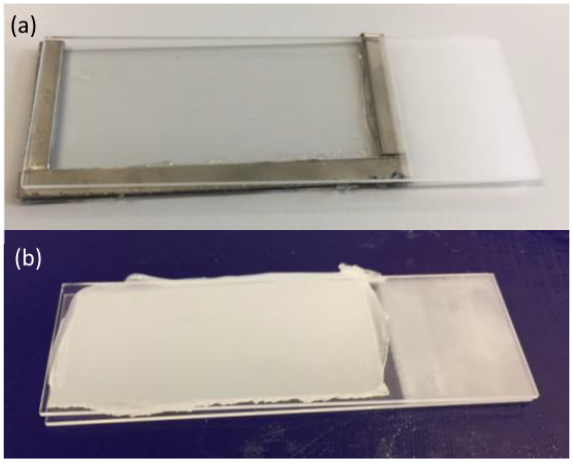

Figure 5.6: (a) Mould for optical samples with 1mm RVS spacers placed in between microscope glasses. (b) The microscope glass with these spacers is replaced by an empty microscope glass to place the sample in the spectrophotometer.

Once the sample has solidified the microscope glass with spacers is replaced by another microscope glass. The sample placed in between these two microscope glasses (figure 5.6b) is then placed in the sample arm of the spectrophotometer to perform the measurements on total diffuse reflectance (figure 5.7a) and total diffuse transmittance (figure 5.7b).

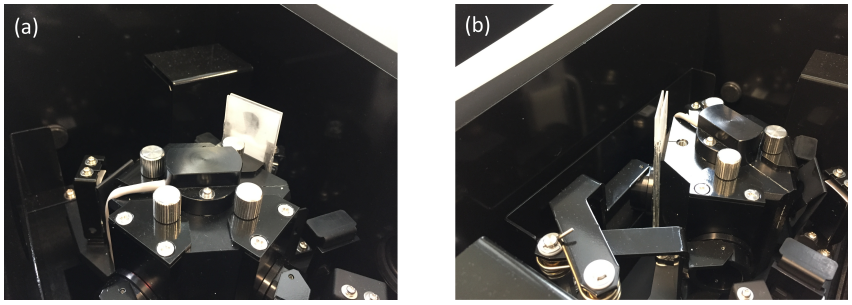

Figure 5.7: (a) Reflectance and (b) transmittance measurement of a sample in the spectrophotometer.

Validation

To validate the IAD method for acquiring optical properties, measurements on intralipid (IL) samples are performed. Two IL samples were fabricated, calculated to have a reduced scattering coefficient of 5 and 10 cm^{-1} at 785 nm. These calculations were based on reported literature values. [85] The IL samples were placed in between microscope glasses that were separated using spacers. The resulting absorption and reduced scattering coefficients are plotted as function of wavelength in figure 5.8.

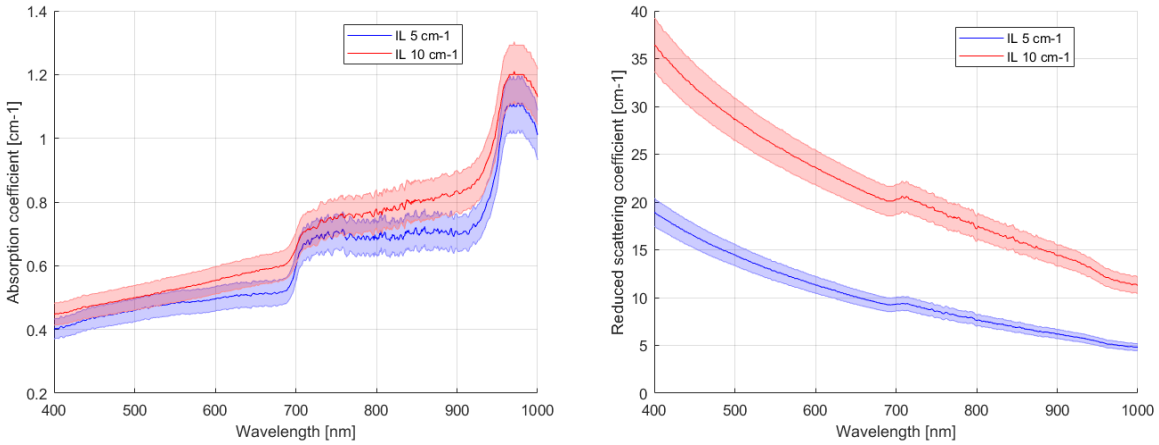

Figure 5.8: (a) Absorption and (b) reduced scattering coefficients for two Intralipid solutions.

This data shows that the IAD programme overestimates the reduced scattering coefficient of intralipid samples by a factor of approximately 1.6. It is not known if this overestimation will result in the same overestimation in the PVCP samples, since the sample holders are slightly different, as the IL holders have metal spacers between the microscope glasses. The inaccuracy in calculating the μ_s' values for intralipid should be taken into account however when the estimated optical properties of the test samples are analysed.

Sample fabrication

Fabrication of the samples is performed according to the protocol described in appendix D. The difference being that acoustic and optical additives are added to the PVCP mixture. After degassing the cold PVCP mixture TiO_2 is added and stirred for 10 minutes. After this, glass beads are also added and mixed again.

Two samples were made to check if the optical properties reported in literature [24] are conform our measured optical properties. Of each sample 100 mL PVCP was prepared. The samples have the following compositions:

Table 5.3: Compositions of two samples for optical characterization of PVCP.

Sample	DEHA v/v	BBP v/v	Heat stabilizer v/v	PVC resin m/m	Glass beads mg/mL	TiO_2 mg/mL	BPC v/v
Fat TMM	57.4& 41.6%	1%	10%	6	1	-	
Fibro TMM	-	99%	1%	10%	30	1.6	-

5.2.2 Results

The resulting optical absorption and reduced scattering coefficients are plotted as function of wavelength in figure 5.9. It can be seen that both samples scatter more strongly than they absorb, as μ_s' is 7.18 and 10 cm^{-1} and μ_a is 1.67 and 0.94 cm^{-1} at 785 nm for fat and fibroglandular tissue, respectively. A bump is seen in all spectra at around 700 nm, which is the wavelength at which the spectrophotometer switches the detector. The light regions in the graphs indicate the estimated error due to a measurement error in the thickness of the sample.

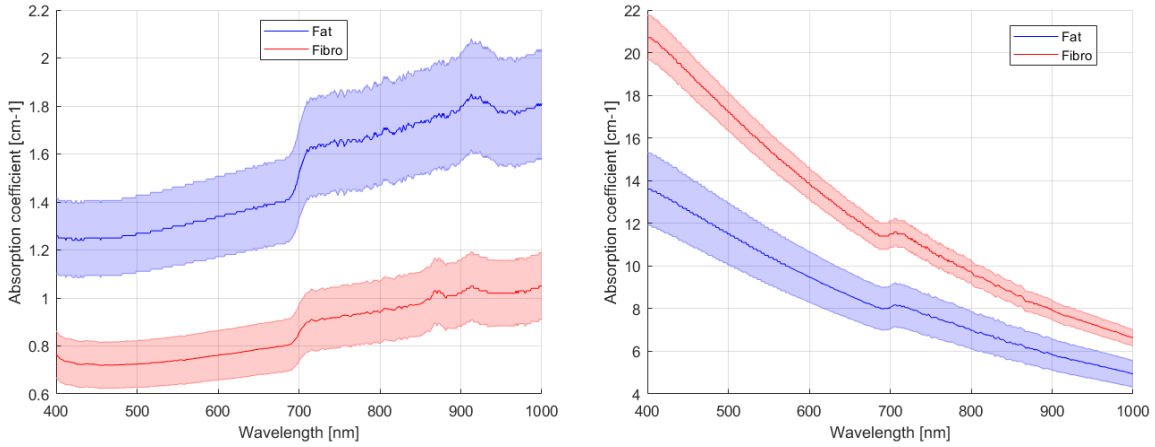

Figure 5.9: Optical spectra of fat and fibroglandular test samples. (a) Optical absorption coefficient and (b) Reduced scattering coefficient. Estimated measurement errors are given by coloured regions.

5.2.3 Discussion

The optical absorption coefficients measured hereare slightly higher than literature values on breast fat and fibroglandular tissue at 785 nm, which are 0.03 and 0.06 cm^{-1} respectively. The measured reduced scattering coefficient are comparable, but a bit lower than the literature values reported on breast tissue, being 8.8 cm^{-1} for fat and 11.6 cm^{-1} for fibroglandular tissue.

However, some errors in the calculation of the optical properties could have occurred to a couple of inaccuracies. The bump at 700 nm is one source of error, because the fit of the IAD method suffers from this transition as well. Besides, the validation on IL samples showed an overestimation of the μ_s' by a factor of 1.6, which may occur in the sample measurements as well.

First of all, the sample thickness was measured using a vernier caliper when the sample was clamped together between two microscope glasses. It could be however that this thickness was not equal at all positions. This error in optical properties due to this error in thickness is shown in the spectra by the light regions.

Then some errors in the input values for the IAD programme could have been made. This consists of errors regarding beam and port sizes. The programme assumes a circular beam and opening in integrating sphere, which is represented by diameters. Both beam and openings are however rectangular and diameters are determined by mimicking the surfaces of both beam and opening by a circle. This could have caused some errors in light loss in or at the boundaries of the sample.

5.2.4 Conclusions

The optical properties of fat and fibroglandular TMM were acquired using the IAD method. The calculated values are comparable to tissue values for fat and fibroglandular tissue. However μ_a is slightly higher and μ_s' is slightly lower than desired. These differences could be explained by errors as were described before, but they could also be the actual values in the samples. The absorption coefficients cannot be lowered, as no absorber was added to the basis PVCP. The reduced scattering coefficients could be increased by adding more TiO_2 to the samples.

5.3 Conclusions

This chapter gives an answer to the research question: *How can this material be optimised for the acoustic and optical properties?* Optimisation of custom PVCP mainly consists of the addition of acoustic speckle and both optical absorption and optical scattering. Besides, the acoustic attenuation is changed as a cause of adding acoustic scatterers. By adding glass beads, TiO_2 and BPC these properties are changed. In this chapter different PVCP samples with different glass beads concentrations were characterised for their acoustic properties. Besides, optical samples were analysed using the IAD method to find values for optical absorption and scattering at certain concentrations of optical additives. The acquired data is used to determine the composition of the different materials in the photoacoustic phantom which is fabricated in the next chapter.

6 | Breast phantom

In this chapter the transition from finding suitable material composition to actually fabricating a breast phantom is made. This requires answering the sixth and seventh research questions: *How can a semi-anthropomorphic breast phantom be designed?* and *What is the performance of the photoacoustic breast phantom?* To answer these questions first the shape of the breast phantom needs to be defined and moulds to fabricate this need to be designed, which is described in section 6.1. After this, the fabrication of an acoustic phantom using these moulds is described in section 6.2. In section 6.3 improvements made based on new insights obtained from this acoustic phantom are described. Finally, in section 6.4 the semi-anthropomorphic photoacoustic phantom is fabricated, characterised and imaged.

6.1 Shape and moulding

When looking at the MR images of female breast in section 2.1 it can be seen that the breast is mainly subdivided into an outer fat region and an inner fibroglandular region. To fabricate a semi-anthropomorphic phantom this subdivision between outer and inner layer should be present, with irregular transitions between those layers. To obtain such a two-layered geometry the experience at the RAM group was used to develop a set of moulds consisting of an inner and outer mould.

The outer mould is based on the circumference of the smallest digital breast phantom, *Neg37*, the skin of which can be seen in figure 6.1a and b. [20] The inner mould should represent the boundary between fat and fibroglandular layer. Inspiration to design this inner mould was received from literature. [12, 57] The phantoms presented there have a regular boundary between different layers. The idea of a cauliflower as irregular shape for the inner structure was found. An online purchased 3D model of a cauliflower (figure 6.1c) therefore forms the starting point of the boundary between the two phantom layers.

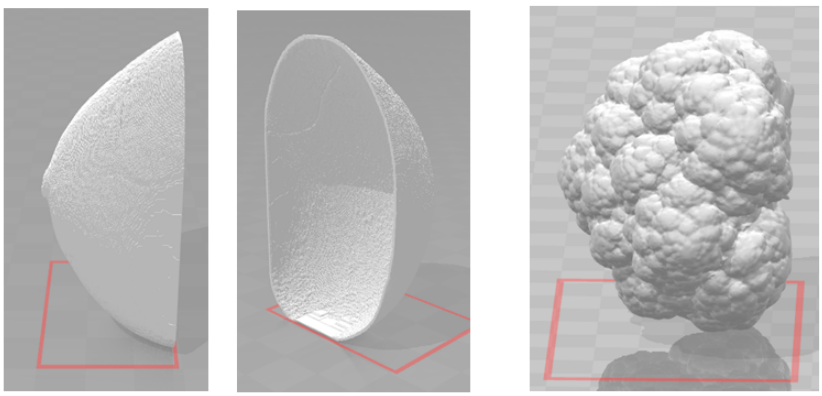

Figure 6.1: Starting shapes for inner and outer mould for breast phantom

From these models 3D printable designs were developed and printed at the Rapid Prototyping Lab (RPLab). The digital designs are shown in figure 6.2a and the actual printed moulds can be seen in figure 6.2b.The outer mould consists of the skin circumference with on top of this a rectangular elevation to make it possible to attach the phantom to a setup. It is supported by four posts, which are on stabilised by placing them on a metal plate. In the sides of the outer mould notches are made to place the inner mould at the correct position.

The inner mould is a smoothened and simplified model of the cauliflower. It still consists of irregular bumps and drops. Some clutches are connected to the cauliflower shape to place it in the notches of the outer mould.

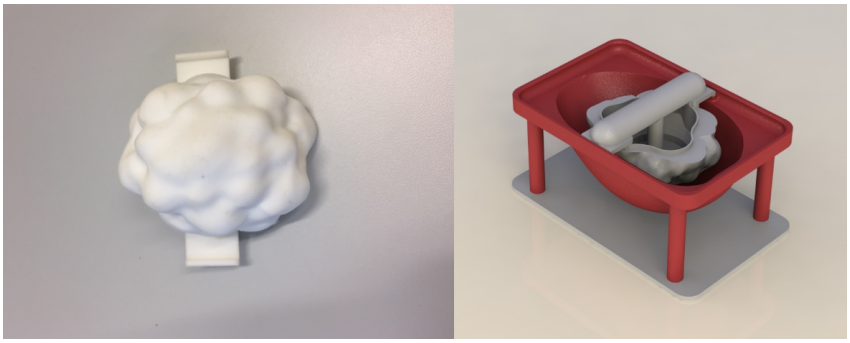

Figure 6.2: Inner mould and digital model of the 3D printed moulding system of inner and outer mould.

The moulds were printed with the material nylone (PA2200) through selective laser sintering (SLS) on the Formiga P101. With this technique a powder is layer by layer sintered such that a solid material is formed. This is done by focussing a laser on the correct spots. The moulds are built from layers of 100 microns in thickness.The melting temperature of the material is 176 °C, which is just below the temperature at which PVCP is liquid. By cooling the phantom during pouring the mould is prevented from melting.

6.2 Acoustic phantom

First an acoustically tuned breast phantom is fabricated to test the protocol and overcome possible problems.

6.2.1 Materials & methods

Fabrication

The two-layered phantom is composed of the TMMs as given in table 6.1.

Table 6.1: Compositions of the two-layered acoustically tuned phantom materials.

Sample	DEHA v/v	BBP v/v	Heat stabilizer v/v	PVC resin m/m	Glass beads mg/mL	TiO_2 mg/mL	BPC v/v
Fat TMM	57.4& 41.6%	1%	8.4%	2	-	-	
Fibro TMM	-	99%	1%	10%	30	-	-

The preparation of the materials is done as described in section **??**. Composing the phantom was done according to the following steps.

1. Preparing the mould in a bath with ice water and soil to prevent the mould from melting.

2. Pouring fat TMM in between outer and inner mould. Place something heavy on inner mould to prevent it from floating.

3. When fat TMM has completely solidified, remove material from both moulds. This had to be done by cutting it loose since the silicone mould attached too good to PVCP.

4. Pour fibroglandular TMM in remaining hole in the middle of fat TMM.

5. When fibroglandular TMM has completely solidified, top the phantom with a layer of fat TMM.

Imaging

After fabrication the phantom was imaged using a clinical US system (Ecube, Alpinion) to obtain B-mode images. Images were made by manually scanning through the phantom using an US coupling gel.

The was also taken to the University of Bern to perform SoS imaging using an ultrasound computed tomography (US-CT) setup, that can be seen in figure 6.3. Emission is done by a rectangular 1-element transducer with center frequency of 5 MHz. Detection is performed using a Verasonics transducer L7-4 having 128 elements and a 5 MHz center frequency. Images were made on two slices in the phantom, and at two moments in time to check the stability.

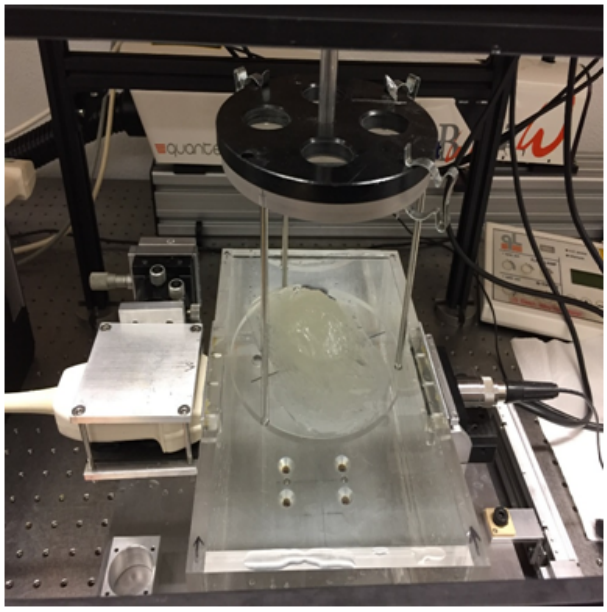

Figure 6.3: Photograph of the US-CT setup at the University of Bern to make a 3D SoS map of the acoustic phantom.

6.2.2 Results

The resulting acoustic phantom can be seen in figure 6.4. As was mentioned before, the phantom had to be cut loose from the mould, which is showing in the end result, the phantom surface being very rough. The more scattering center part can be seen nicely in the image as well.

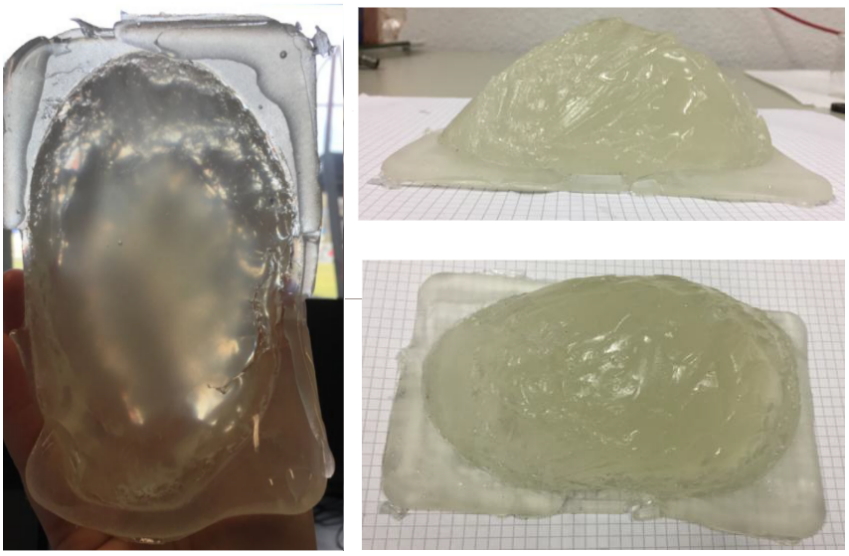

Figure 6.4: The acoustic phantom. The photograph on the left shows the more scattering inner structure. The photographs on the right show the damaged outer layer due to cutting it loose from the mould.

The acoustic properties of this phantom are summarized in table 6.2. These were determined from test blocks that were made simultaneously with the phantom. These sample are the same as samples Fat2 and Fibro30 that were described in the previous chapter.

Table 6.2: Acoustic properties of acoustic breast phantom.

Material	**SoS**	**Power law function**		**Impedance**
	[m/s]	**a**	**b**	**[MRayls]**
Fat	1437 ± 0	0.27 ± 0.01	1.12 ± 0.02	1.63 ± 0.07
Fibroglandular	1509 ± 3	0.495 ± 0.005	1.63 ± 0.01	1.84 ± 0.07

In figure 6.5 some images made with the Alpinion system are shown. On the left some part of the cauliflower structure is visible with a linear probe at 12.0 MHz. On the right image made using a spherical probe at 2.0 MHz the cauliflower shape seems to have flattened a lot. In both images a difference in speckle pattern between both layers is seen, as the speckles in the fibroglandular TMM are a lot more dense than in the fat TMM. Besides, there seems to be some boundary between both layers, with no signal coming off.

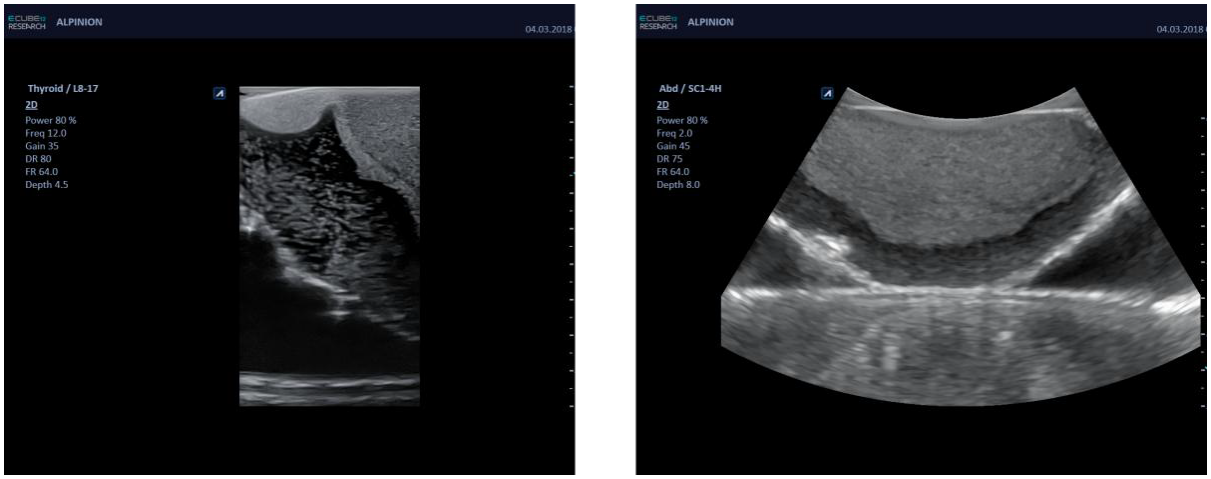

Figure 6.5: Two images of the acoustic phantom made with the Alpinion system. On the left a high-resolution image can be seen using a 12.0 MHz transducer and an linear probe. On the right a lower resolution image is seen using a spherical probe at 2.0 MHz.

In figure 6.6 some four speed of sound maps are shown made with the setup at the university of Bern. These images are made on different moments in time after fabricating the phantom and for different slices of the phantom. The exact SoS values are highly dependent on the reconstruction SoS that is taken, so these are not used for characterization. Besides, it is difficult to find a homogeneous ROI since a lot of artefacts show up in the image. What can be seen, is the drop in contrast at the image in the right lower corner. This is the part of the phantom nearest to the nipple, which means the fibroglandular TMM has a large contact surface with fat TMM. An explanation for this drop in contrast may be the diffusion of plasticizer from one layer to the other. The cauliflower shape is difficult to distinguish from these images. This might be due to the numerous artefacts in the image. Another reason may be due to the fact that the shape is not well formed due to the difficulties in releasing the phantom from the mould.

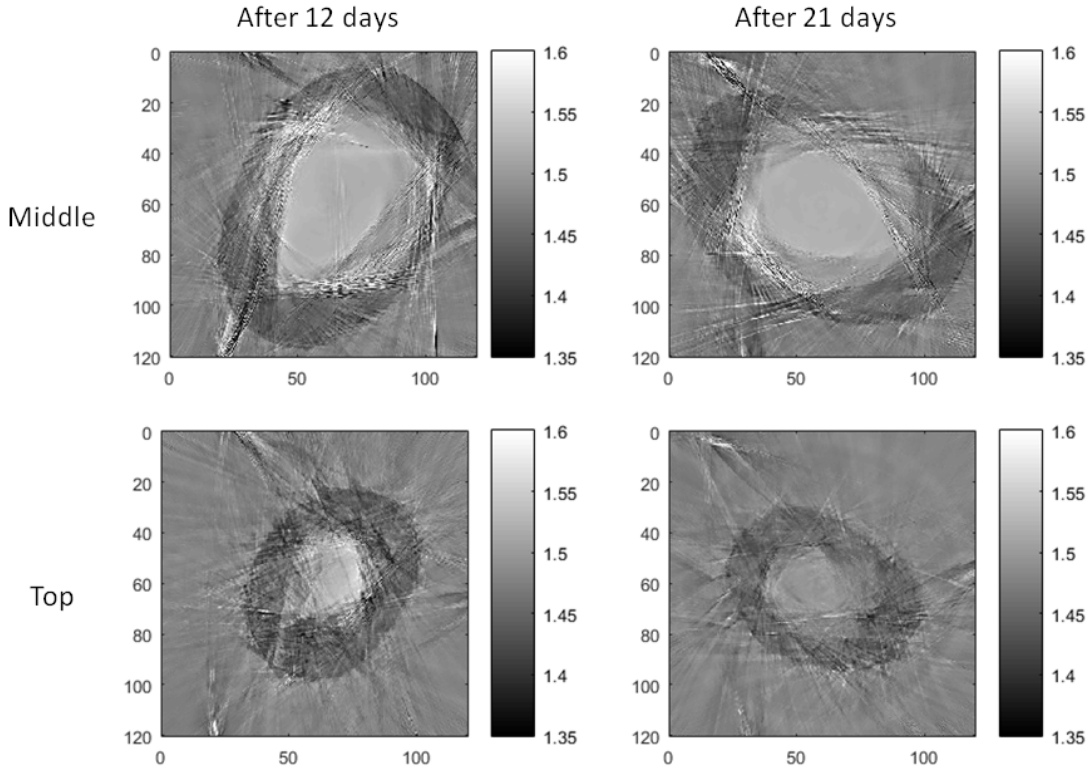

Figure 6.6: Stability measurements using the SoS imaging setup at the university of Bern

6.2.3 Discussion & conclusions

Releasing the phantom from the silicone mould showed to be one of the problems occuring in fabricating this acoustic phantom. This causes a damaged outer structure and probably the flattening of the cauliflower boundary structure inside the phantom. A solution to this releasal from both outer and inner mould should be found.

The stability images showed that contrast between both layers decreases as time passes. This is probably due to the diffusion of plasticizer. To prevent this some coating layer in between these materials should be investigated.

6.3 Improving phantom fabrication

This section describes improvements to the design of the breast phantom to overcome the problems mentioned in the previous section. The releasal of the phantom from the mould can be solved in two ways, one is applying a skin layer on the outer mould and two is using a spray to release the inner mould. The second problem was the diffusion

of plasticizer, which can be solved by applying a coating at the boundary of the two materials.

6.3.1 Skin

It was decided to fabricate a skin around the phantom to help it release from the mould, increase its appearance, increase safety when people touch the phantom, and to mimic a layer which influence primarily the light propagation due to a relatively high absorption by the skin. To mimic this skin, silicone (Shore 40, polyestershoppen.nl) is used. This material has a simple fabrication protocol and can easily be varied in colour and thickness. The composition of the materials was experimentally altered until a good ratio between components was found. The ratio of components A and B was defined by the manufacturer, the percentage of thickener was based on the thickness of the material and the percentage pigment pastes were determined by eye. The materials and composition that were used for fabricating the skin layer surrounding the photoacoustic phantom are:

- 90 % m/m silicone component A
- 9 % m/m silicone component B
- 0.5 % m/m thickener
- 0.54 % m/m white pigment paste
- 0.08 % m/m orange pigment paste

The step-by-step protocol is described in appendix **??**. Shortly, the mould is covered with a layer of releasing spray. Then components A and B are weighed off, added together in a mixing beaker and stirred. The thickener is added and stirred through the mixture. The pigment pastes are weighed off in another beaker, after which the mixture of silicone is added to this second beaker. When everything is stirred well again, a thin layer is applied to the outer mould of the breast phantom. This layer needs to solidify for six hours, after which it can be peeled off. The final result can be seen in figure 6.7.

Figure 6.7: The outer and inner surface of the silicone skin for the photoacoustic phantom.

6.3.2 Releasing from mould

To release the inner mould from the PVCP structure surrounding it a PTFE (or teflon) dry-smear spray (WD-40) is applied to the mould. This material is some sort of a dry oil that can be used for releasing moulds according the supplier. It is resistant to a

temperature of 250 °C A very thin layer of the material attaches to the mould. The material does not seem to dissolve in the poured PVCP and helps to release the mould from the PVCP perfectly.

6.3.3 Preventing diffusion

Migration of plasticizer from especially the fibroglandular PVCP takes place, since a wet layer on the surface of this material can be observed after some time. To prevent this migration the PVCP is coated with a layer of acrylic varnish, which is normally used for protecting paintings against humidity. Once the PVCP has solidified the acrylic varnish is applied by a brush in two to three layers, with each layer having a drying time of two hours.

A test sample was made to check whether plasticizer diffusion still occurs when an acrylic varnish layer is applied in between the fibroglandualr and fat layer. This sample consists of a block shaped fat TMM, with on top of that a block of fibroglandular TMM with extra added BPC and an acrylic varnish coating in between both (figure 6.8.

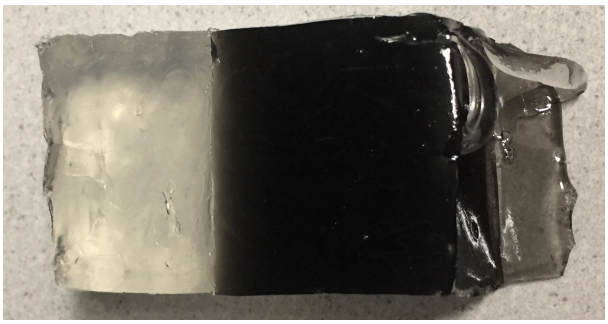

Figure 6.8: The test block to measure effect of acrylic varnish in between fat and fibroglandular TMM layers.

With the insertion method the SoS is measured at several positions in the sample. The block is placed on a translation stage, to translate the block with steps of 1 mm at a time. The speed of sound as function of position was measured for this test block at two moments in time; directly after fabrication and after five weeks. The results of these measurements are shown in figure 6.9. In measurement 1 a clear transition between both layers can be seen, while this transition is more gradually in measurement 2. It seems that nonetheless the acrylic varnish layer in between both layers, plasticizer diffusion takes place. However, two remarks on this should be made. Air was present in between both layers during measurement 2, since the fibroglandular (black) TMM released from the fat (transparent) TMM when taking it from the mould. This air resulted in distorted acoustic pulses, and less accurate SoS measurements seen by the large variations in the graph. Secondly, some difficulties in applying the acrylic varnish layer occurred. The layer did not coat the fat TMM homogeneously, and therefore still some gaps in between this layer could have been present. In this case, diffusion would still be possible. The acrylic varnish layer could still work out, however applying it should be performed well and additional tests on its ability to prevent diffusion should be performed.

In this graph errors are visualised as light regions. These errrors are based on an estimation of the error made in measuring the thickness of the material. These errors are very large, indicating that the measurement is not that accurate.

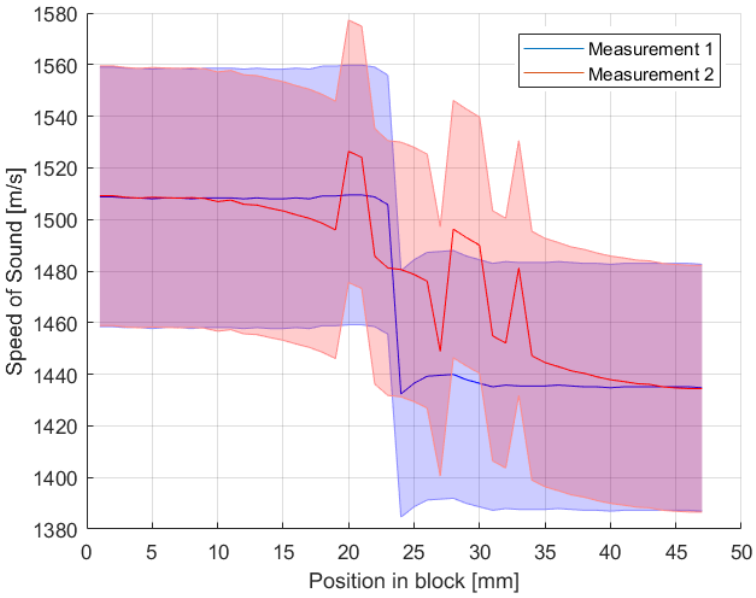

Figure 6.9: Measured speed of sound values for different positions in the acrylic varnish test block. Measurement 1 is performed one day after fabrication and measurement 2 five weeks after this.

6.4 Photoacoustic phantom

The photoacoustic phantom is the final product of this master thesis. It is a semi-anthropomorphic breast phantom consisting of four materials mimicking skin, fat, fibroglandular and tumor/blood vessels. In this section the fabrication of this phantom is described, after which results from imaging it are presented.

6.4.1 Materials & Methods

Fabrication

The fabrication of the skin of the phantom is described in the previous section. The other three TMMs are made from a composition of PVCP which is shown in table 6.3.

Table 6.3: Compositions of PVCP TMMs present in the photoacoustic phantom.

Sample	DEHA v/v	BBP v/v	Heat stabilizer v/v	PVC resin m/m	Glass beads mg/mL	TiO_2 mg/mL	BPC v/v
Fat TMM	57.4& 41.6%	1%	10%	6	1	-	
Fibro TMM	-	99%	1%	10%	30	1.6	-
Blood TMM	-	99%	1%	10%	-	1.6	0.2 %

The fabrication of the PVCP materials is done according to the protocol described in appendix D and the silicone fabrication protocol is described in appendix F. The actual composing of the phantom is described step by step:

1. Fabricate skin layer
2. Fabricate tumor/blood vessel
3. Coat tumor/blood vessel with acrylic varnish
4. Fabricate fat TMM and insert tumor/blood vessel inside
5. Release inner mould from outer fat tissue
6. Coat this fat TMM on the inside with acrylic varnish
7. Fabricate fibroglandular TMM and pour into hole inside fat outer layer while inserting tumor/blood vessel inside
8. Coat the fibroglandular TMM with acrylic varnish
9. Top the phantom with a layer of fat TMM

For fabricating he tumors and blood vessel an arbitrary approach was taken. Blood vessels were made by pouring the PVCP in thin lines over a plate, after which the best one was chosen (figure 6.10).

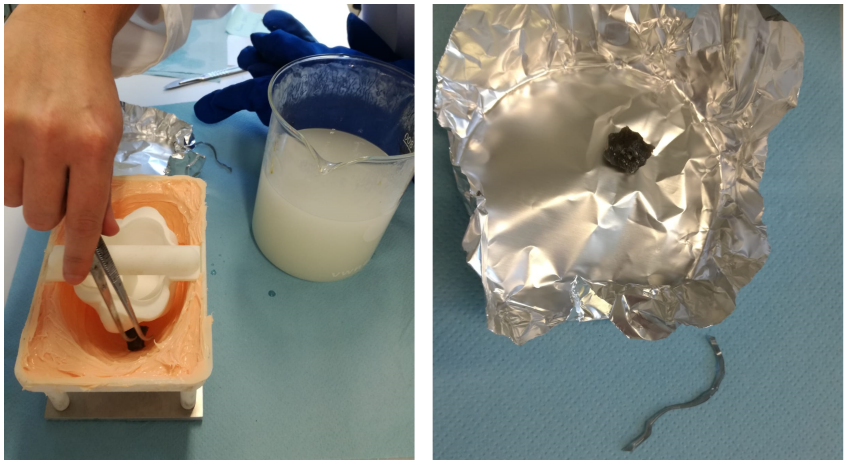

Figure 6.10: The tumor and blood vessels located in fat TMM are shown. The process of inserting the tumor is also shown.

The tumors were cut in a arbitrary shape, after which two were chosen, one of which can be seen in figure 6.10. The blood vessel is 2-3 mm in diameter, the tumor located

in the fat tissue is 1-2 cm in diameter and the tumor located in fibroglandular tissue has a volume region of 1-2 cm in diameter and blood vessels of approximately 2 mm in diameter attached to this. The insertion of the the tumor in fat TMM is also shown in figure 6.10.

Characterisation

Characterisation of the phantom is done using the methods as described in chapters 4 and 5. SoS and AA are determined using the modified insertion technique. The development of speckle is checked using the method described in section 5.1. Optical properties are estimated using the IAD method. To perform these characterisation measurements test samples of the TMMs were made. Acoustic test blocks of fat, fibroglandular and tumor/blood TMM were made and optical samples were made of all four tissue mimicking materials, including skin.

Imaging

The photoacoustic phantom is imaged using three different imaging modalities, MRI, US B-mode and PAT.

The phantom is placed in a dual phased array DPA Knee coil (Easaote SpA) in a 0.25T MRI scanner (G-scan Brio, Easote SpA) to obtain MR images. Multiple sequences are tested to see the image contrast. From these, the best sequence is chosen to visualise the phantom. With this the location of the tumors/blood vessels can be validated.

The US B-mode images were made using the clinical US system (Ecube, Alpinion). The linear L3-12 probe was used to image at a frequency of 6.0 MHz. Some handheld images were made using a gel for acoustic coupling, see figure 6.11.

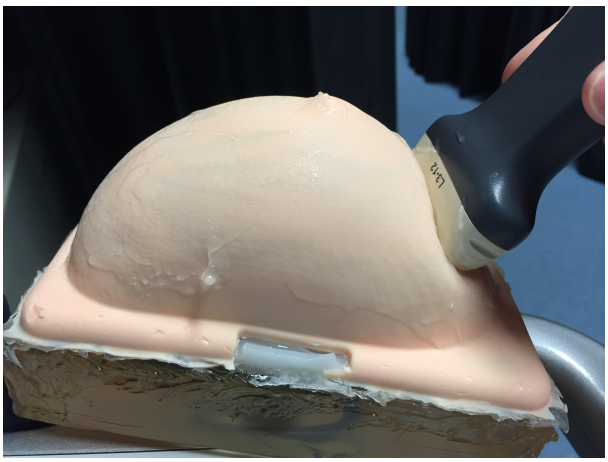

Figure 6.11: The photoacoustic breast phantom is imaged using handheld B-mode imaging with a L3-12 probe from the Alpinion system.

Besides, a 3D scan through the phantom was made using the setup shown in figure 6.12.

The probe is mounted in an aquarium and the phantom is secured to a 3D moving stage. In this way the phantom is moved relative to the probe. The phantom is moved for several positions of the phantom in x- and y-direction, in such a way that the complete phantom is imaged with overlapping parts to position the images correctly with respect to each other. Then an image is made at ten different z-positions for each x- and y-position.

Figure 6.12: The setup for 3D scanning the photoacoustic breast phantom using B-mode images. A linear L3-12 probe from the Alpinion system is mounted and the phantom moves relative to this probe using a 3D moving stage.

The phantom is imaged in the PAM 2 system to assess its performance as photoacoustic phantom. The PAM 2 system is visible in figure 6.13.

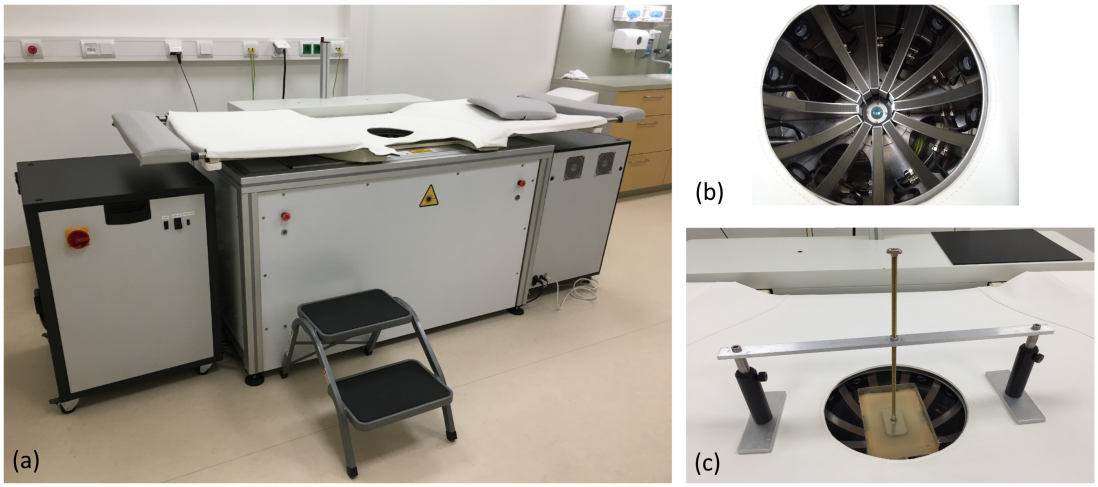

Figure 6.13: The PAM 2 system with the setup for imaging the phantom. (a) Complete system with bed in which the hole is visible. (b) Water tank with optical fibers ultrasound detectors. (c) Setup for submerging the phantom in the water tank.

It consists of a bed with a hole in which a water tank is located. On the outside of this water tank fibers and detectors are located to provide for illumination and detection of US signals, respectively. To place the breast phantom inside the water tank a setup is fabricated (figure 6.13. It consists of two posts placed in post holders. To these posts a horizontal bar is attached, which has a rod in the middle. This rod is attached to an aluminium plate which is fixated to the phantom by pouring a layer of commercial PVCP soft around it.

The imaging bowl has a diameter of 35 cm and is filled with water, which has a temperature of 21-23 °C during the measurements. Inside the bowl are illumination points and detectors arms, installed in an interleaved setup. The PAM 2 uses an Nd:YAG and Alexandrite combined Q-switched laser to illuminate the breast (Qcombo, Quanta System, Milan, Italy) using excitation wavelengths of 1064 and 755 nm respectively. Illumination is performed from the side and bottom of the tank, through a 50-50 energy division. The US pulses are detected by a system of detector arms having an array of piezcomposite elements detecting signals with center frequency of 1 MHz. Averaged photoacoustic data is acquired to perform image reconstruction with. For this a fiiltered backprojection method was implemented. The images are visualised using a local maximum intensity projection.

6.4.2 Results

The results of fabricating the phantom are to be seen in figure 6.14. The tumor and blood vessel are well seen in the fatty outer layer. The scattering of the fat TMM is a lot lower than that of the fibroglandular TMM, while the optical scattering coefficients of tissue are not that different. The final result shows the phantom with commercial PVCP poured on top to fixate the phantom to a hanging system for doing PAT measurements.

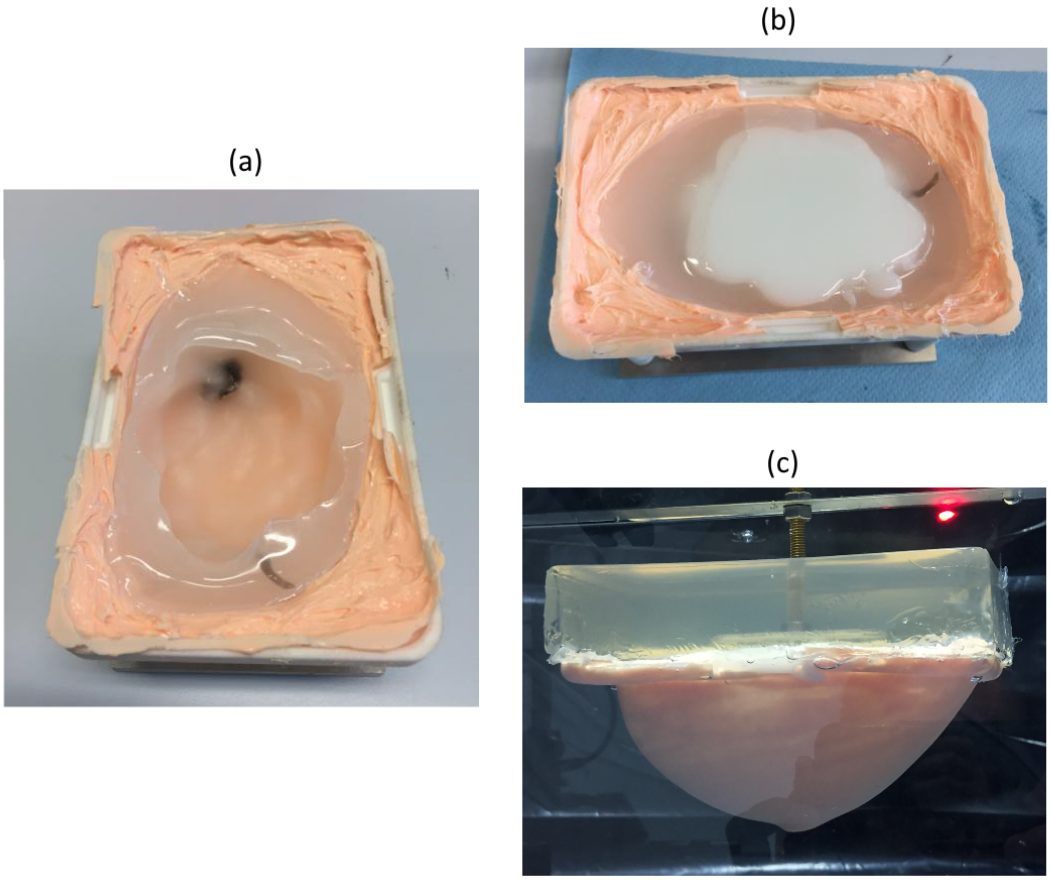

Figure 6.14: Intermediate and end results of photoacoustic phantom. (a) Shows the fat outer layer attached to the skin and one of the tumors and a blood vessel inside. In (b) the fibroglandular layer including a second tumor was poured inside. (c) shows the final phantom from the side submerged in a water tank. A commercial PVCP layers was poured on top to attach it to a hanging system.

Characterisation

The acoustic attenuation as function of frequency with power law fits for fat, fibroglandular and tumor TMM is given in figure 6.15.

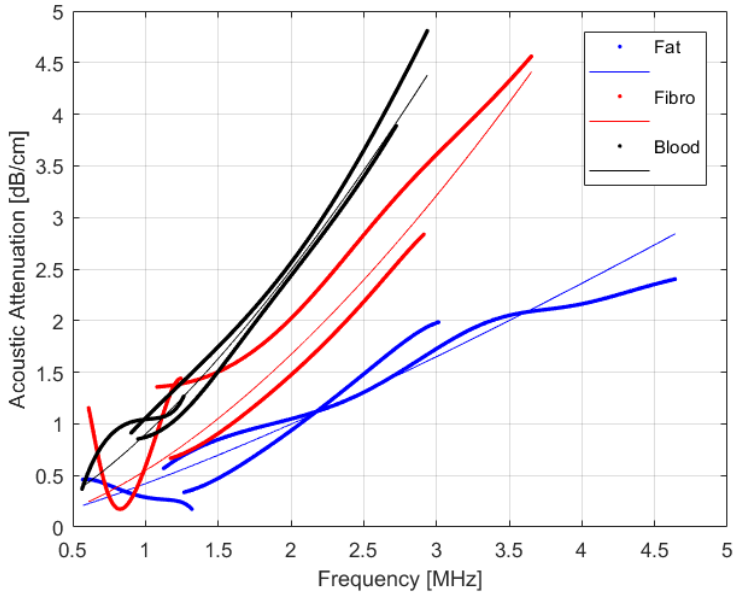

Figure 6.15: Acoustic attenuation of fat, fibroglandular and blood TMM plotted as function of frequency with power law functions fitted through the data. The thick lines are the data points, while the thin lines are the power law fits.

The resulting acoustic properties of the TMMs present in the photoacoustic phantom are given in table 6.4.

Table 6.4: Acoustic properties of photoacoustic breast phantom.

Material	**SoS**	**AA**	**Power law function**		**Impedance**
	[m/s]	**[dB/cm/MHz]**	**a**	**b**	**[MRayls]**
Fat TMM	1447 ± 1	-	0.42 ± 0.005	1.24 ± 0.01	1.55 ± 0.06
Fibro TMM	1511 ± 0	-	0.55 ± 0.008	1.61 ± 0.015	1.79 ± 0.05
Blood TMM	1511 ± 3	-	0.90 ± 0.005	1.47 ± 0.006	1.82 ± 0.05
Skin TMM	-	-	-	-	-
Fat tissue	1440 ± 19.9	1-1.8	-	-	1.31
Fibro tissue	1524 ± 27	2-2.7	-	-	1.59
Blood tissue	1582 ± 5	0.15 ± 0.01	-	-	1.67
Skin tissue	1607 ± 32	1.22 ± 0.83	-	-	1.85

The optical absorption and reduced scattering coefficients of all four TMMs are shown in figure 6.16.

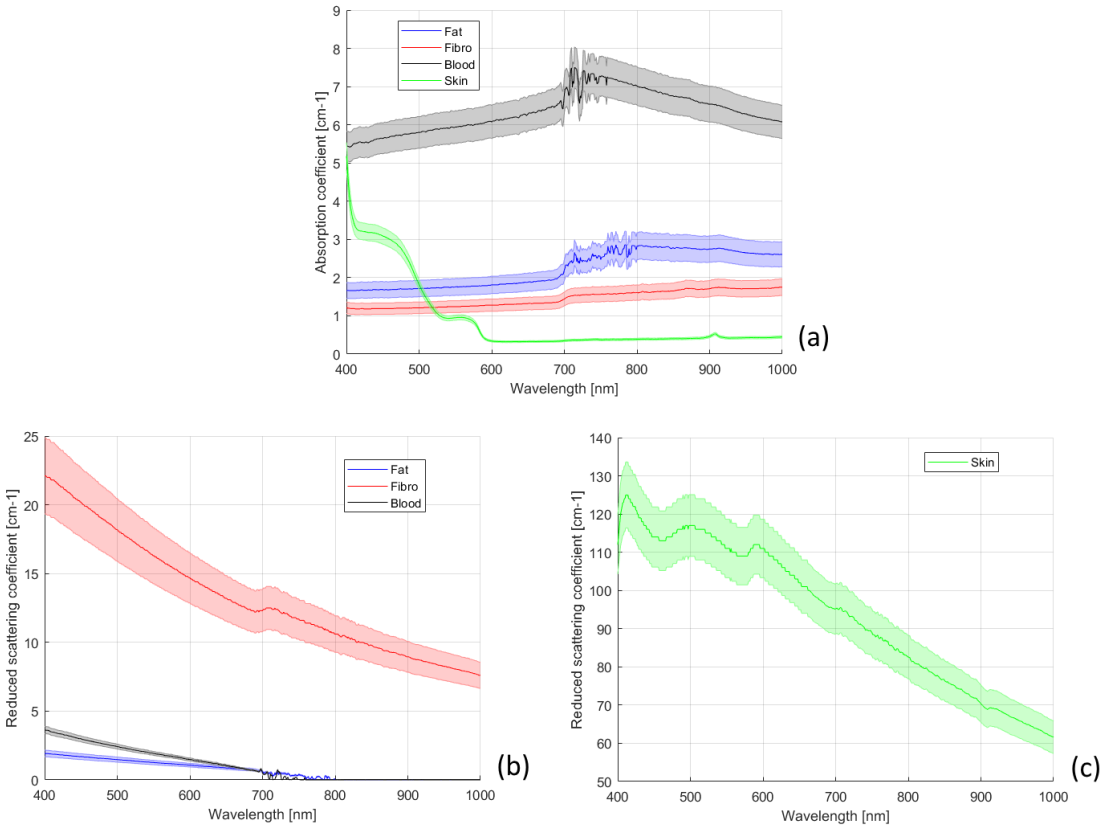

Figure 6.16: Spectra of optical properties of four TMMs. (a) Absorption spectra of all materials, (b) reduced scattering coefficients of fat, fibroglandular and tumor TMM and (c) reduced scattering coefficient of skin TMM.

The resulting optical properties of the TMMs present in the photoacoustic phantom are given in table 6.5.

Table 6.5: Optical properties of photoacoustic breast phantom.

Material	$\boldsymbol{\mu_a}$ $[\mathbf{cm^{-1}}]$	$\boldsymbol{\mu_s'}$ $[\mathbf{cm^{-1}}]$
Fat TMM	2.75 ± 0.3	0.1 ± 0.05
Fibro TMM	1.60 ± 0.2	10.9 ± 1.4
Blood TMM	7.11 ± 0.5	0
Skin TMM	0.39 ± 0.04	84.7 ± 5.9
Fat tissue	0.03	8.8 ± 0.7
Fibro tissue	0.06	11.6 ± 0.6
Blood tissue	6.6 ± 3.3	9.1 ± 6.3
Skin tissue	0.3 ± 0.2	16.1 ± 8.0

Imaging

In figure 6.17 a slice imaged with the T2-relaxation sequence is shown. In this image the fatty outer layer shows up bright, while the fibroglandular inner layer is seen to be darker. The tumor TMM, which can be seen within the white circles, has even lower intensity values. The tumors are not that well visible, due to low contrast. The blood vessel should be located somewhere in the left part of this image, but is not visible in one of the slices. The skin is not giving acoustic contrast to either the background or the fat TMM. The cauliflower based boundary between fat and fibroglandular tissue shows well in this image.

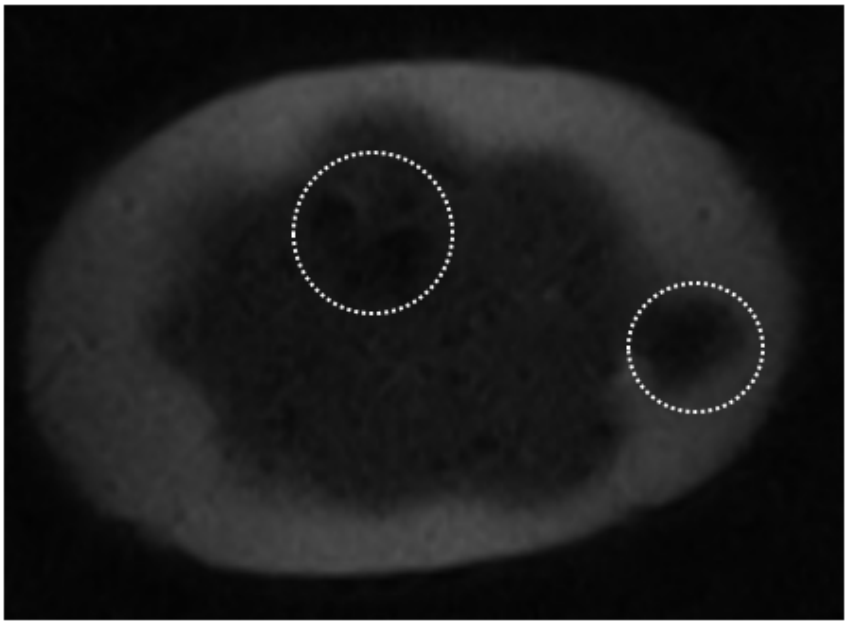

Figure 6.17: A slice imaged with the 0.5T MRI using a T2 sequence. The tumors are circled in white.

The B-mode US images obtained are shown in figure 6.18. The two tumors and blood vessels are clearly visible in these images due to high acoustic contrast. The skin is shown as a bright region in the top part of these images. More scattering particles are embedded in the fibroglandular TMM than in fat TMM, therefore the first shows up brighter and the cauliflower based boundary is well visible.

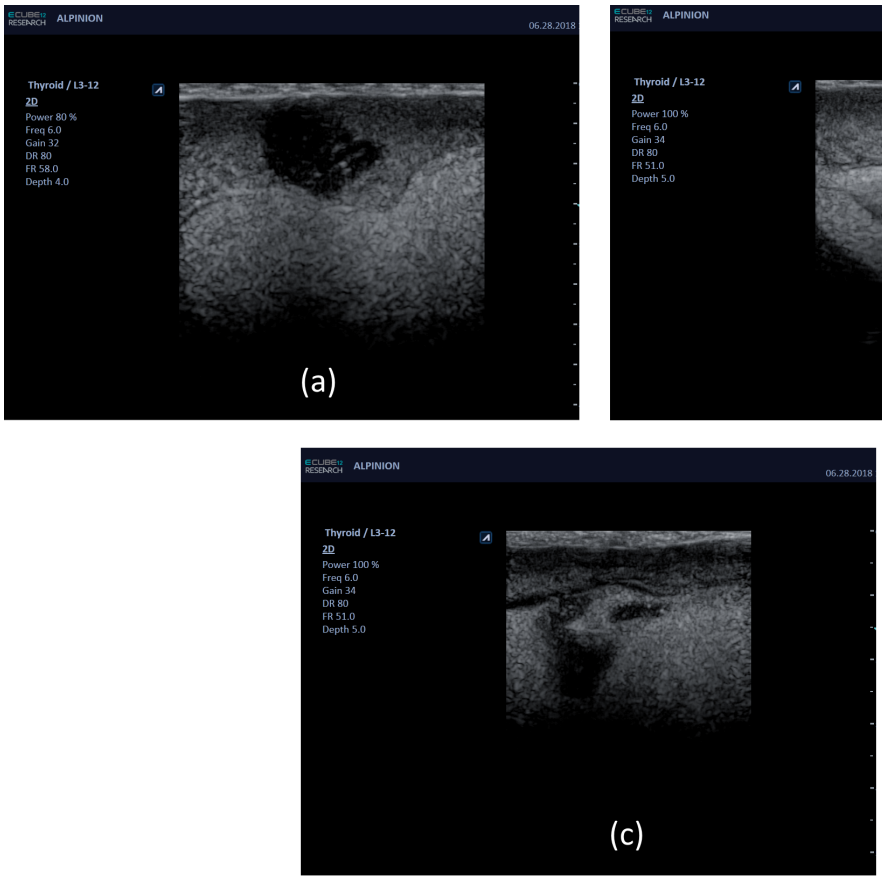

Figure 6.18: US B-mode images using handheld positioning. In these images the skin is well visible by the brigh region in the top part of the images. The cauliflower based boundary between fat and fibroglandular layers is clearly found due to a difference in scattering intensities between fat and fibroglandular regions. No US scattering particles were embedded into the tumors and blood vessel, thus they are seen as black regions in the images. (a) Shows the tumor in fat tissue, in (b) the blood vessel is circled in red and in (c) the tumor with attached blood vessels in fibroglandular tissue shows up.

PAT images were made using the PAM 2 system. These images can be seen in figure 6.19. This consists of images reconstructed at 755 nm, since this is closest to the wavelength (= 785 nm) for which the phantom was optically tuned. In these images the blood vessel and both tumors show up nicely. Some reconstruction artefacts can be seen however in the images, which may be due to the aluminium plate that is placed in the top part of the phantom, as could be seen in figure **??**c. Besides some shadows in the reconstruction are still visible due to SoS mismatches between reconstruction and reality. This is especially seen in the reconstruction of the blood vessel. The skin does show up in the x-y projection, but it is not as clearly visible as in images made of test subjects. Besides, the nipple is not visible. The tumor structures are not visible as solid structures, which is probably due to the fact that low frequency signals are generated by larger volumes and these signals are not detected accurately by the 1 MHz detector arms. The sharp edges present in the tumor are however showing up which results in the images shown.

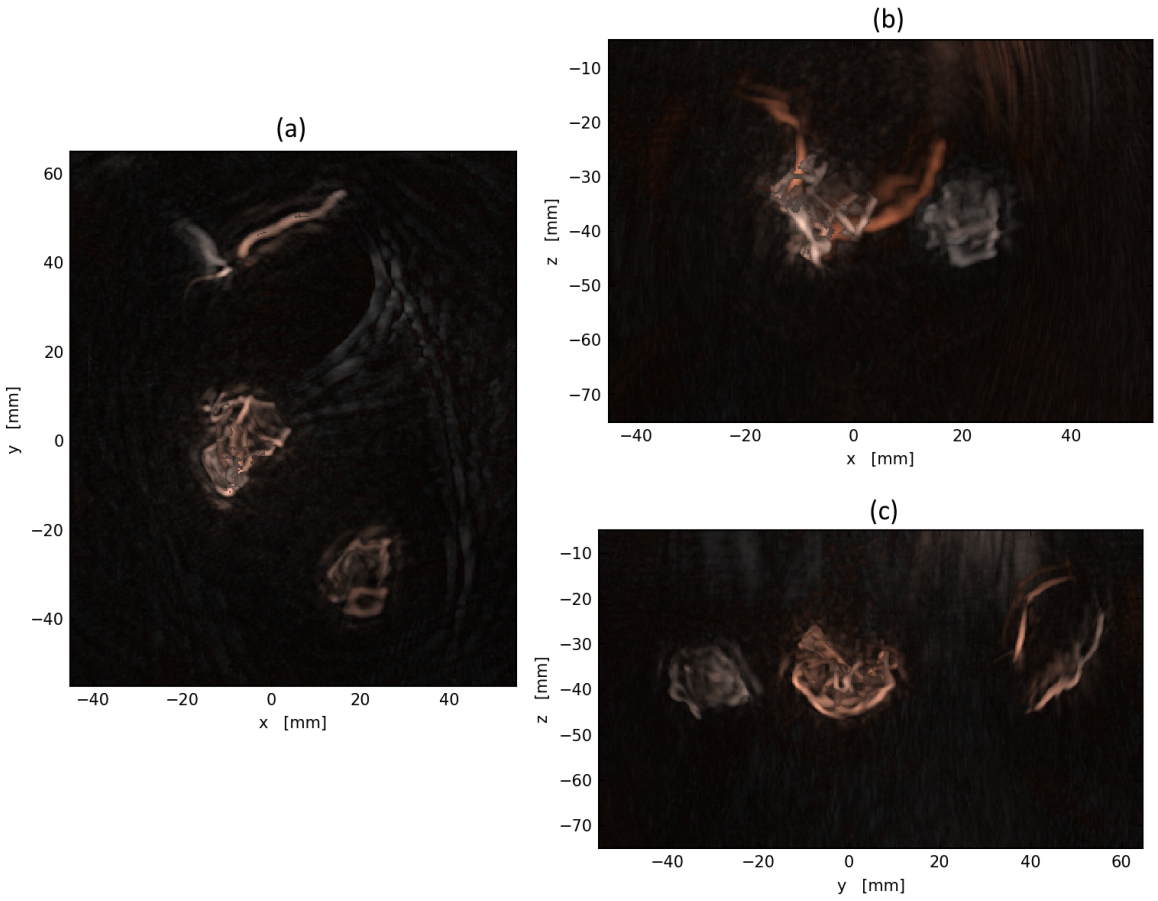

Figure 6.19: Local maximum intensity projections from three different views using the PAM 2 system. The orange colour indicates deeper lying structures, while white/gray is more superficial. In (a) the x-y plane, (b) the x-z plane and (c) the y-z plane are shown.

6.4.3 Discussion

During fabrication of the photoacoustic phantom two problems occurred. The first problem was the dissolving of TiO_2 in the PVCP mixture. Because the volume in which this was dissolved was too large, no homogeneous distribution was obtained, which resulted in a low reduced scattering coefficient for fat TMM. The problem was solved for fibroglandular TMM. The second problem was the release of skin from fat layer during loosening of the inner mould. This results in water that could flow into the phantom while it is submerged in water. The influence of water is that high, but is present in acoustic or photoacoustic imaging.

6.4.4 Conclusions

The photoacoustic breast phantom was fabricated succesfully, although some problems occured. The complete fabrication protocol was tested and can be optimised based on

experiences obtained. The irregular shaped boundary between fat and fibroglandular tissue is well visible in images, as are the absorbing structures. The acoustic and optical properties of the materials are similar to those of tissue, except for the values obtained for skin TMM. This material has a reduced scattering coefficient that is a lot higher and an absorption coefficient at 785 nm that is a lot lower than in tissue.

6.5 Conclusions

In this chapter two research questions were answered: *How can a semi-anthropomorphic breast phantom be designed?* and *What is the performance of the breast phantom?* It was decided that semi-anthropomorphic breast phantom is a 3D breast phantom consisting of four different materials with an irregular boundary between fat and fibroglandular tissue. To develop this, a 3D printed mould system was made consisting of an outer mould based on segmented MR skin data and an inner mould based on a smoothened cauliflower to resemble this boundary.

A skin layer is applied in the outer mould, after which fat TMM is poured in between the skin and inner mould. Once the inner mould is removed fibroglandular TMM can be poured into this space and tumors and a blood vessel were inserted in both fat and fibroglandular layers. An acrylic varnish layer was applied in between the material types to prevent plasticizer diffusion.

To answer the second research question the phantom materials were characterised acoustically and optically and imaged using three different imaging modalities: MRI, US and PAT. Skin was not tuned, resulting in acoustic and optical properties not comparable to tissue values. The acoustic properties of the other three materials are comparable to tissue values. Optical absorption is higher than tisue values for fat and fibroglandular tissue, while optical scattering is lower for fat tissue and comparable to literature values for fibroglandular tissue. Blood optical properties were comparable to tissue values.

Contrast between different layers was very good in US images, such that different structures could be distinguished easily. This contrast was lower in MRI, in which the blood vessel and the skin were not seen. PAT resulted in images clearly showing the three absorbing structures, but the expected signal of the skin was not present in this images.

All in all, a well-characterised photoacoustic phantom was fabricated using a newly developed mould system. In essence the phantom performs well, but some improvements need to be made.

7 | Conclusions & recommendations

In this chapter conclusions are drawn and an answer to the main research question is formulated. Besides some recommendations for further research are given.

7.1 Conclusions

In this research a semi-anthropmorphic photoacoustic breast phantom was fabricated, with well characterised acoustic and optical properties. A protocol for fabricating tissue mimicking materials (TMM) using a custom made polyvinyl chloride plastisol (PVCP) was developed and tested elaborately. Moulds for fabricating a semi-anthropomorphic breast phantom were developed. Existing characterization techniques were implemented for using these to find the relevant properties of the phantom materials.

7.1.1 Phantom material

Literature reviewing and experimentally characterizing candidate phantom materials, resulted in custom PVCP being most suitable as photoacoustic breast phantom material. The material is a combination of the plasticizers di(2-ethylhexyl) adipate (DEHA) and benzyl butyl phthalate (BBP), together with calcium-zinc heat stabilizer and dissolved PVC resin. The ratio of plasticizer combination and PVC resin concentration affect the acoustic and optical properties. Additives to tune acoustic and optical properties further are glass beads, titanium dioxide(TiO_2) and black plastic colouring (BPC) to increase acoustic and optical scattering, and optical absorption respectively.

7.1.2 Design

From online available 3D digital phantoms obtained from magnetic resonance imaging (MRI) of female breasts the complexity of breast tissue became known. The breast mainly consists of a complex architecture of fat and fibroglandular tissue, surrounded by a skin layer. Fat is located primarily in the outer part, while fibroglandular tissue is found in the central part of the breast. Therefore a 3D printed mould system was developed to fabricate a semi-anthropomorphic phantom in which this geometry is present. The outer mould is based on segmented skin data from one of the digital phantoms and the inner mould is based on a smoothened 3D cauliflower structure to represent the irregular boundary between these tissue layers.

7.1.3 Photoacoustic phantom fabrication

The photoacoustic phantom that was fabricated consists of skin, fat, fibroglandular and tumor/blood TMMs. The skin was made from silicon using 90% m/m component A, 9% m/m component B, 0.5% m/m thickener, 0.54% m/m white pigment paste and 0.08% m/m orange pigment paste. A thin layer was applied to the outer phantom mould and it was completed once it solidifed. Fat TMM was poured in between the skin layer and the inner mould. The inner mould was released when the fat layer solidified, the gap was filled with fibroglandular tissue. During the release of the inner mould, the skin and fat materials were released from each other at some positions. A tumor (diameter 1-2 cm) and a blood vessel (diameter 2-3 mm) were inserted into the fat layer and a second tumor (arbitrary size) was inserted in the fibroglandular layer. The fat, fibroglandular and tumor/blood TMMs were all made from different compositions of PVCP. Fat TMM consist of 58% v/v DEHA and 42% v/v BBP, while fibroglandular and tumor TMM were made using 100% v/v BBP. Fat and fibroglandular both contain 10% m/m PVC resin, while this amount was 15% m/m in tumor/blood. 1% v/v heat stabilizer was added to all materials. For acoustic scattering the fat and fibroglandular materials contain respectively 6 and 30 mg/mL glass beads. Optical scattering is increased by adding 1 mg/mL TiO_2 to fat TMM, and 1.6 mg/mL to fibroglandular and tumor/blood TMM. Optical scattering particles in fat TMM were not well distributed throughout the material due to a fabrication error. BPC was added only to the tumor/blood material in a concentration of 0.2% v/v.

7.1.4 Characterisation

An adapted insertion technique was used for acoustic characterisation of the phantom materials. A setup and moulds were constructed. The speed of sound (SoS) values of fat, fibroglandular and tumor/blood are respectively 1447, 1511 and 1511 m/s. Power law fits of acoustic attenuation (AA) are resulting in 0.42, 0.55 and 0.90 dB/cm at 1 MHz for these materials. Acoustic impedances of the three tissue types are 1.24, 1.61 and 1.82 MRayls. The fat and fibroglandular TMMs both have fully developed acoustic speckle.

The inverse adding doubling (IAD) method was used to obtain the optical absorption (μ_a) and reduced scattering coefficients (μ_s') of all four tissue types at 785 nm. This results in values for μ_a of 2.75, 1.60, 7.11 and 0.39 cm^{-1} for fat, fibroglandular, tumor/blood and skin respectively. For these tissue types μ_s' is 0.1, 10.9, 0 and 84.7 cm^{-1}.

The acoustic properties are comparable to literature values of these tissue properties. SoS of fibroglandular TMM is only slightly lower. The optical scattering of fat, fibroglandular and tumor/blood TMM is a bit lower than literature values, although in the same order of magnitude. Optical absorption of fat and fibroglandular tissue is significantly higher than tissue values. Optical absorption of tumor/blood is comparable to literature values. The optical scattering of skin is a lot higher, while optical absorption of skin at 785 nm is a lot lower than desired. More tuning regarding this is therefore still required.

7.1.5 Imaging

The phantom was imaged using three different imaging modalities: MRI, ultrasound (US) and photoacoustic tomography (PAT). The phantom was not tuned for MR imaging and the contrast in these images is low. In a T2 sequenced image cross sections of both tumors are visible, but the blood vessel remains unseen. The boundary between fat and fibroglandular layers is well visible. US B-mode imaging shows good acoustic contrast due to the speckle difference between the tissue types. Both tumors and the blood vessel are found by scanning through the phantom. Also a gap filled with water in between skin and fat TMM was showing up on the images. Using PAT the three structures gave a well-distinguishable photoacoustic signal, but some artefacts in image reconstruction are present. The skin and nipple give way-less signal than in measurements on human test subjects however.

7.1.6 Overall conclusion

The main research question of this thesis is: *How is a semi-anthropomorphic breast phantom for photoacoustic applications fabricated?* An answer to this question arises from the conclusions given above. The phantom is fabricated using four TMMs, fat, fibroglandular, skin and tumor/blood. The geometry of the phantom consists of an outer skin layer, then a fat layer and an inner fibroglandular layer, with a irregular boundary in between fat and fibroglandular layer. Tumors and a blood vessel are inserted for photoacoustic contrast. By implementing characterization techniques for acoustic and optical properties the phantom was acoustically and optically tuned to breast tissue. For validating the performance and structures of the phantom it was imaged using three imaging modalities.

7.2 Recommendations

Several recommendations to this research will be discussed, based on finding and experiences during the experiments.

7.2.1 Skin optical properties

The skin TMM optical properties are not mimicking tissue skin the way it was fabricated. Optical absorption was too low at 785 nm, while optical scattering was too high. It should be tested whether the optical scattering can be lowered to realistic values when no pigment paste is added. If this is possible, different colours of pigment paste should be tested on their optical absorption at 785 nm. If it is not possible to optimise these properties, simulations should be performed to check whether the skin is of significant influence on the photoacoustic signal. When this is the case, a different material for mimicking skin tissue should be investigated. PVCP can be suitable to mimic this skin, but speed of sound as high as skin can probably not be obtained.

7.2.2 Overcoming fabrication problems

Two problems occured during fabrication of the photoacoustic phantom. The first being the low optical scattering in fat TMM, caused by improper mixing of TiO_2 through the PVCP solution. In fat TMM TiO_2 was mixed through a large volume (550 mL) of PVCP, which has resulted in bad dissolving of the particles. The problem was solved in fibroglandular TMM by dissolving TiO_2 in a small volume (50 mL) first and then mixing this through the stock solution again.

The second problem in the fabrication process is the release of skin from fat layer when the inner mould was taken from the phantom. When the phantom is submerged in water, water can float in this gap, showing up on US images. This can be fixed by glueing the top boundary between fat and skin using silicon glue. This is only possible if the region is not in the imaging volume.

7.2.3 Phantom complexity

It can be discussed what complexity in geometry is needed for fabricating an anthropomorphic breast phantom. To find an answer to this simulations should be performed to compare image quality between a simulation using the phantom geometry and the 3D digital phantom geometry. From these simulations it can be determined whether more complexity is needed to accurately mimic the behaviour of light and ultrasound in breast tissue.

7.2.4 Blood vessel network

In photoacoustic imaging (PAI) absorption by hemoglobin in blood creates contrast. When a deeper lying tumor needs to be identified, large superficially lying blood vessels disturb the photoacoustic signal generated by the tumor. To mimic this in a phantom a blood vessel network comparable to networks found in tissue should be implemented in the phantom. Besides, by creating the possibility to have a liquid flowing through these blood vessels the phantom can be used for validation of quantitative PAI. By changing the absorption coefficients of the fluid at different wavelengths which is corresponding to a certain oxygen saturation, information on the saturation level can be obtained from the photoacoustic image.

Some possibilities for fabricating blood vessels have already been explored, however temperature resistance of the materials forming blood vessel walls is a big hurdle. It would be ideal to 3D print a complex blood vessel network, but many 3D printable materials are not capable of dealing with the heat when pouring hot PVCP on top. Besides the material should either be acoustically transparent or should be able to dissolve in a fluid that is not harmful to the phantom. Another fabrication method could be to use latex as vessel walls. This was used at the university of Bern, as they latex coated arbitrary vessels structures made with glycerine soap. This glycerine soap was later dissolved after which a hollow latex tube remained.

7.2.5 Preventing plasticizer migration

To prevent plasticizer migration a layer of acrylic varnish was applied in between the fat and fibroglandular materials. It is however not known well what the performance of this layer is. A rectangular test sample, consisting of these two PVCP layers with a layer of acrylic varnish in between, was made, but results are not convincing. The acrylic varnish did not cover the surface boundary well in this test block and it seems as if diffusion still took place. The data are however highly distorted due to air bubble in between both layers. Besides, in the phantom the varnish layer did cover the boundary between both layers well. The performance of acrylic varnish should therefore be determined again by repeating the experiment with the rectangular block or by doing 3D speed of sound imaging of the phantom through timie using an ultrasound computed tomography (UCT) setup.

If the acrylic varnish does not perform well, prevention of plasticizer migration could be done in other ways as well, namely by using methods for treating the surface of the material. This could be done by coating the surface, exposing it to UV light or using a plasma oven. However these methods still need to be explored completely on its applicability to the fabricated PVCP materials.

7.2.6 Phantom size

The breast phantom that was fabricated in this research is relatively small compared to the average breast that is imaged in breast cancer imaging. It was chosen to use a small breast, because a lot of experiments had to be performed first. The smaller volume the breast consists of means less material that is needed and therefore lowering the costs. To be able to validate imaging of very deep lying structures it is however important to fabricate larger breast phantoms. To do this, the developed moulds can be easily upscaled.

Bibliography

[1] World Health Organization. Breast cancer. `http://www.who.int/cancer/prevention/diagnosis-screening/breast-cancer/en/`. Accessed: 13-02-2018.

[2] World Cancer Research Fund International. Breast cancer statistics. `https://www.wcrf.org/int/cancer-facts-figures/data-specific-cancers/breast-cancer-statistics`. Accessed: 13-02-2018.

[3] M. Heijblom. *Clinical experiences with photoacoustic breast imaging - the appearance of suspicious lesions*. PhD thesis, 2014.

[4] H. Vainio and F. Bianchini. *Screening Techniques*, volume 7, chapter Ch2: Screening Techniques, pages 25–37. IARC Press, 1st ed. lyon, france edition, 2002.

[5] K.M. Harris and V.G. Vogel. Breast cancer screening. *Cancer and Metastasis Reviews*, 16:231–262, 1997.

[6] A. Pinto, F. Pinto, A. Faggian, G. Rubini, F. Caranci, L. Macarini, E.A. Genovese and L. Brunese. Sources of error in emergency ultrasonography. *Critical Ultrasound Journal*, 5, 2013.

[7] J. Folkman. Fighting cancer by attacking its blood supply. *Scientific American*, 275(3):150–154, 1996.

[8] N. Nishida, H. Yano, T. Nishida, T. Kamura and M. Kojiro. Angiogenesis in cancer. *Vascular Health and Risk Management*, 2(3):213–219, 2006.

[9] S. Manohar and D. Razanski. Photoacoustics: a historical review. *Adavances in Optics and Photonics*, 8(4):586–617, 2016.

[10] M.H. Xu and L.H.V. Wang. Photoacoustic imaging in biomedicine. *Review Scientific Instruments*, 77(4):041101, 2006.

[11] L. Wang. Tutorial on photoacoustic microscopy and computed tomography. *IEEE Journal of Selected Topics in Quantum Electronics*, 14(1):171–179, 2008.

[12] C. Jia, W.C. Vogt, K.A. Wear, T.J. Pfefer and B.S. Garra. Two-layer hetereogeneous breast phantom for photoacoustic imaging. *Journal of Biomedical Optics*, 22(10):106011, 2017.

[13] S.E. Bohndiek, S. Bodapati, D. van de Sompel, S.-R. Kothapalli and S.S. Gambhir. Development and application of stable phantoms for the evaluation of photoacoustic imaging instruments. *PLOS One*, 8(9):e75533, 2013.

[14] M. Fonseca, B. Zeqiri, P.C. Beard and B.T. Cox. Characterisation of a phantom for multiwavelength quantitative photoacoustic imaging. *Physics in Medicine and Biology*, 61(13):4950–4973, 2016.

[15] B. Cox, J.G. Laufer, S.R. Arridge and P.C. Beard. Quantitative spectroscopic photoacoustic imaging: a review. *Journal of Biomedical Optics*, 17(6):061202, 2012.

[16] H. Zolfagharnasab, S. Bessa, S.P. Oliveira, P. Faria, J.F. Teixeira, J.S. Cardoso and H.P. Oliveira. A regression model for predicting shape deformaiton after breast conserving surgery. *Sensors*, 18(1):E167, 2018.

[17] I.E. Khuda. A comprehensive review on design and development of human breast phantoms for ultra-wide band breast cancer imaging systems. *Engineering Journal*, 21(3):183–206, 2017.

[18] W. Huang, A. Tudorica, S. Chui, K. Kemmer, A. Naik, M. Troxell and M. Holtorf. Variations of dynamic contrast-enhanced magnetic resonance imaging in evaluation of breast cancer therapy response: a multicenter data analysis challenge. The Cancer Imaging Archive. `http://doi.org/10.7937/K9/TCIA.2014.A2N1IXOX`.

[19] E.N. Marieb. *Human Anatomy & Fysiology*, chapter Ch27: The Reproductive System, pages 1018–1063. Pearson, 9th edition edition, 2013.

[20] Y. Lou, W. Zhou, T.P. Matthews, C.M. Appleton and M.A. Anastasio. Generation of anatomically realistic numercial phantoms for photoacoustic and ultrasonic breast imaging. *Biomedical Optics*, 22(4):041015, 2017.

[21] T.L. Szabo. *Diagnostic Ultrasound Imaging: Inside Out*. Academic Press, 1st edition edition, 2004.

[22] M.O. Culjat, D. Goldenberg, P. Tewari and R.S. Singh. A review of tissue substitutes for ultrasound imaging. *Ultrasound in Medicine and Biology*, 36(6):861–873, 2010.

[23] K.A. Wear, T.A. Stiles, G.R. Frank, E.L. Madsen, F. Cheng, E.J. Feleppa, C.S. Hall,B. Soo Kim, P. Lee, W.D. O'Brien, M.L. Oelze, B.I. Raju, K.K. Shung, T.A. Wilson and J.R. Yuan. Interlaboratory comparison of ultrasonic backscatter coefficient measurements from 2 to 9 mhz. *Journal of Ultrasound in Medicine*, 24(9):1235–1250, 2005.

[24] W.C. Vogt, C. Jia, K.A. Wear, B.S. Garra and T. Joshua Pfefer. Biologically relevant photoacoustic imaging phantoms with tunable optical and acoustic properties. *Journal of Biomedical Optics*, 21(10):101405, 2016.

[25] T.A. Tuthill, R.H. Sperry and K.J. Parker. Deviations from rayleigh statistics in ultrasonic speckle. *Ultrasonic Imaging*, 10(2):81–89, 1988.

[26] F. Duck. *Physical Properties of Tissue: a Comprehensive Reference Book*. Academic Press, 1st edition edition, 2007.

[27] C.M. Moran, N.L. Bush and J.C. Bamber. Ultrasonic propagation properties of excised human skin. *Ultrasound in Medicine and Biology*, 21(9):1177–1190, 1995.

[28] M. Weichenthal, P. Mohr and E.W. Breitbart. The velocity of ultrasound in human primary melanoma tissue - implications for the clinical use of high resolution sonography. *BMC Dermatology*, 1(14), 2001.

[29] C. Escffier, B. Querleux, J. de Rigal and J.L. Leveque. *In vitro* study of the velocity of ultrasound in the skin. *Bioengineering Skin*, 2:87–94, 1986.

[30] S. Yongchen, D. Yanwu, T. Jie and T. Zhensheng. Ultrasonic parameters in human tissues. *Ultrasonics symposium*, pages 905–908, 1986.

[31] J.F. Greenleaf and R.C. Bahn. Clinical imaging with transmissive ultrasonic computerized tomography. *IEEE Transactions on Biomedical Engineering*, 28(2):177–185, 1981.

[32] C. Li, N. Duric, P. Littrup, L. Huang. In vivo breast sound speed imaging with ultrasound tomography. *Ultrasound in Medicine and Biology*, 5(10):1615–1628, 2009.

[33] H.G. Nasief, I.M. Rosado-Mendez, J.A. Zagzebski and T.J. Hall. Acoustic properties of breast fat. *Journal of Ultrasound in Medicine*, 34(11):2007–2016, 2016.

[34] B. Rajagopalan, J.F. Greenleaf, P.J. Thoma, S.A. Johnson and R.C. Bahn. *Ultrasonic tissue characterization II*, chapter Variation of acoustic speed with temperature in various excised human tissues studied by ultrasound computerized tomography, pages 227–233. 1979.

[35] A.L. Scherzinger, R.A. Belgam, P.L. Carson, C. R. Meyer, J.V. Sutherland, F.L. Bookstein and T.M. Silver. Assessment of ultrasonic computed tomography in symptomatic breast patients by discriminant analysis. *Ultrasound in Medicine and Biology*, 15(1):1–28, 1989.

[36] J. Wiskin, D.T. Borup, S.A. Johnson and M. Berggren. Non-linear inverse scattering: high resolution quantitative breast tissue tomography. *Journal of Acoustical Society of America*, 131(5):3802–3813, 2012.

[37] J. Wiskin, D. Borup, K. Callahan, Y. Parisky, J. Smith, M.P. André and S. Johnson. *Acoustical Imaging*, chapter Inverse Scattering Results, pages 61–68. 2011.

[38] M.E. Anderson, M.S. Soo and G.E. Trahey. In vivo breast tissue backscatter measurements with 7.5- and 10-mhz transducers. *Ultrasound in Medicine and Biology*, 27(1):75–81, 2001.

[39] P.D. Edmonds, C.L. Mortensen, J.R. Hill, S.K. Holland, J.F. Jensen, P. Schattner, A.D. Valdes, R.H. Lee and F.A. Marzoni. Ultrasound tissue characterization of breast biopsy specimens. *Ultrasonic iimaging*, 13(2):162–185, 1991.

[40] M. Weichenthal, P. Mohr and E.W. Breitbart. The velocity of ultrasound in human primary melanoma tissue - implications for the clinical use of high resolution sonography. *BMC Dermatology*, 1(1), 2001.

[41] L.V. Wang and H.I. Wu. *Biomedical Optics: Principles and Imaging*, chapter Appendix A: Definitions of Optical Properties, page 343. John Wiley & Sons, Inc., 1st edition edition, 2007.

[42] F.L. Pedrotti, L.S. Pedrotti and L.M. Pedrotti. *Introduction to Optics*. Pearson Education, 3rd edition edition, 2007.

[43] J.L. Sandell and T.C. Zhu. A review of *in-vivo* optical properties of human tissues and its impact on pdt. *Journal of Biophotonics*, 4(11-12):773–787, 2011.

[44] S.L. Jacques. Optical properties of biological tissues: a review. *Physics in Medicine and Biology*, 58(11):R37–R61, 2013.

[45] V.G. Peters, D.R. Wyman, M.S. Patterson and G.L. Frank. Optical properties of normal and diseased human breast tissues in the visible and near infrared. *Physics in Medicine and Biology*, 35(9):1317–1334, 1990.

[46] B. Brooksby, S. Jiang, H. Dehghani, B.W. Pogue, K.D. Paulsen, C. Kogel, M. Doyley, J.B. Weaver and S.P. Poplack. Magnetic resonance-guided near-infrared tomography of the breast. *Review of Scientific Instruments*, 75(12):5262–5270, 2004.

[47] S.L. Jacques. Over de organisatie. `https://omlc.org/software/mc/mcxyz/`. Accessed: 25-05-2018.

[48] M.O. Culjat, D. Goldenberg, P. Tewari and R.S. Singh. A review of tissue substitutes for ultrasound imaging. *Ultrasound in Medicine and Biology*, 36(6):861–873, 2010.

[49] B.W. Pogue and M.S. Patterson. Review of tissue simulating phantoms for optical spectroscopy, imaging and dosimetry. *Journal of Biomedical Optics*, 11(4):041102, 2006.

[50] T.J. Hall, M. Bilgen, M.F. Insana and T.A. Krouskop. Phantom materials for elastography. *IEEE Transactions on Ultrasonics, Ferroelectrics, and Frequency Control*, 44(6):1355–1365, 1997.

[51] E.L. Madsen, J.A. Zagzebski, R.A. Banjavie and R.E. Jutila. Tissue mimicking materials for ultrasound phantoms. *Medical Physics*, 5(5):391–394, 1978.

[52] J.R. Cook, R.R. Bouchard and S.Y. Emelianov. Tissue-mimicking phantoms for photoacoustic and ultrasonic imaging. *Biomedical Optics Express*, 2(11):3193–3206, 2011.

[53] J. Laufer, E. Zhang and P. Beard. Evaluation of absorbing chromophores used in tissue phantoms for quantitative photoacoustic spectroscopy and imaging. *IEEE Journal of Selected Topics in Quantum Electronics*, 16(3):600–607, 2010.

[54] A.I. Farrer, H. Odéen, J. de Bever, B. Coats, D.L. Parker, A. Payne and D.A. Christensen. Characterization and evaluation of tissue-mimicking gelatin phantoms for use with mrgfus. *Journal of Therapeutic Ultrasound*, 3(1):9, 2015.

[55] L.M. Cannon, A.J. Fagan and J.E. Browne. Novel tissue mimicking materials for high frequency breast ultrasound phantoms. *Ultrasound in Medicine & Biology*, 37(1):122–135, 2011.

[56] T. Kondo and M. Kitatuji. New tissue mimicking materials for ultrasound phantoms. *IEEE Ultrasonics Symposium*, 3:1664–1667, 2005.

[57] E.L. Madsen, M.A. Hobson, G.R. Frank, H. Shi, J. Jiang, T.J. Hall, T. Varghese, M.M. Doyley and J.B. Weaver. Anthropomorphic breast phantoms for testing elastography systems. *Ultrasound in Medicine & Biology*, 32(6):857–874, 2006.

[58] W. Xia, D. Piras, M. Heijblom, W. Steenbergen, T.G. van Leeuwen and S. Manohar. Poly(vinyl alcohol) gels as photoacoustic breast phantoms revisited. *Journal of Biomedical Optics*, 16(7):075002, 2011.

[59] A. Kharine, S. Manohar, R. Seeton, R.G.M. Kolkman, R.A. Bolt, W. Steenbergen and F.F.M. de Mul. Poly(vinyl alcohol) gels for use as tissue phantoms in photoacoustic mammography. *Physics in Medcine and Biology*, 48(3):357–370, 2003.

[60] S. Sethuraman, S. Aglyamov, J.Amirian, R. Smalling and S. Emelianov. Intravascular photoacoustic imaging to detect and differentiate atherosclerotic plaques. *Ultrasonics Symposium*, 1:133–136, 2005.

[61] M. Nambu, T. Watari, T. Sakamoto and K. Akojima. Method for applying electromagnetic wave and ultrasonic wave therapies, 1990. US Patent No. 4,958,626.

[62] K. Zell, J.I. Sperl, M.W. Vogel, R. Niessner and C. Haisch. Acoustical properties of selected tissue phantom materials for ultrasound imaging. *Physics in Medicine and Biology*, 52(20):N475–N484, 2007.

[63] C.M. Hassan and N.A. Peppas. *Biopolymers - PVA Hydrogels Anionic Polymerisation Nanocomposites*, chapter Structure and Applications of Poly(vinyl alcohol) Hydrogels Produced by Conventional Crosslinking or by Freezing/Thawing Methods, pages 37–65. Advances in Polymer Science, 2000.

[64] C. Avigo, N. Di Lascio, P. Armanetti, C. Kusmic, L. Cavigli, F. Ratto, S. Meucci, C. Masciullo, M. Cecchini, R. Pini, F. Faita and L. Menichetti. Organosilicon phantom for photoacoustic imaging. *Journal of Biomedical Optics*, 20(4):046008, 2013.

[65] G.M. Spirou, A.A. Oraevsky, I. Alex Vitkin and W.M. Whelan. Optical and acoustic properties at 1064 nm of polyvinyl chloride-plastisol for use as a tissue phantom in biomedical optoacoustics. *Physics in Medicine & Biology*, 50(14):N141–N153, 2005.

[66] N. Hungr, J.-A. Long, V. Beix and J. Troccaz. A realistic deformable prostate phantom for multimodal imaging and needle-insertion procedures. *Medical Physics*, 39(4):2031–2041, 2012.

[67] D. Sikaria, S. Musinksy, G.M. Sturgeon, J. Solomon, A. Diao, M.E. Gehm, E. Samei, S.J. Glick and J.Y. Lo. Second generation anthropomorphic physical phantom for mammography and dbt: Incorporating voxelized 3d printing and inkjet printing of iodinated lesion inserts. *Medical Imaging*, 9783:978360, 2016.

[68] A.T. Mobashsher and A.M. Abbosh. Three-dimensional human head phantom with realistic electrical properties and anatomy. *IEEE Antennas and wireless propagation letters*, 13:1401–1404, 2014.

[69] B.L. Oliveira, D. O'Loughlin, M. O'Halloran, E. Porter, M. Glavin and E. Jones. Microwave breast imaging: experimental tumour phantoms for the evaluation of new breast cancer diagnosis sytems. *Biomedical Physics and Engineering*, 2018.

[70] E. Maneas *et al.* Anatomically realistic ultrasound phantoms using gel wax with 3d printed moulds. *Physics in Medicine and Biology*, 63(1):015033, 2018.

[71] S.J. Arconada-Alvarez, J.E. Lemaster, J. Wang and J.V. Jokerst. The development and characterization of a novel yet simple 3d printed tool to facilitate imaging of photoacoustic contrast agents. *Photoacoustics*, 5:17–24, 2017.

[72] D.I. Nikitichev, A. Barburas, K. McPherson, J.M. Mari, S.J. West and A.E. Desjardins. Construction of 3-dimensional printed ultrasound phantoms with wall-less vessels. *Journal of Ultrasound in Medicine*, 35:1333–1339, 2016.

[73] J.G. Mainprize, A.K. Carton, R. Klausz, Z. Li, D.M. Hunter, *et al.* Development of a physical 3d anthropmorphic breast texture model using selective laser sintering rapid prototype printing. *Proceedings of SPIE*, 10573:105730A, 2018.

[74] T. Rydholm, A. Fhager and P.M. Meaney. A first evaluation of the realistic supelec-breast phantom. *IEEE Journal of electromagnetics, RF, and microwaves in Medicine and Biology*, 1(2):59–65, 2017.

[75] M.J. Burfeindt, T.J. Colgan, R. Owen Mays, J.D. Shea, N. Behdad, B.D. van Veen and S.C. Hagness. Mri-derived 3d printed breast phantom for microwave breast imaging validation. *IEEE Antennas and Wireless Propagation Letters*, 11:1610–1613, 2012.

[76] W. Xia, D. Piras, J. van Hespen, W. Steenbergen and S. Manohar. A new acoustic lens material for large area detectors in photoacoustic breast tomography. *Photoacoustics*, 1(2):9–18, 2013.

[77] Kaye & Laby. The speed and attenuation of sound. `http://www.kayelaby.npl.co.uk/general_physics/2_4/2_4_1.html`. Accessed: 04-07-2017.

[78] M. Greenspan. *Amercican Institute of Physics (AIP) Handbook*, chapter Acoustic properties of liquids, pages 3–87. 3rd edition edition, 1972.

[79] Stratasys. Object connex 3. `http://www.stratasys.com/3d-printers/objet260-connex3`. Accessed: 04-07-2017.

[80] P. Hiremath, P.T. Akkasaligar and S. Badiger. *Advancements and Breakthroughs in Ultrasound Imaging*, chapter Speckle Noise Reduction in Medical Ultrasound, pages 201–241. 2011.

[81] N. Dutta. Carcinoma of breast. `http://www.ultrasound-images.com/breast/`. Accessed: 04-07-2017.

[82] S.A. Prahl, M.J.C. van Gemert and A.J. Welch. Determining the optical properties of turbid media by using the adding-doubling method. *Applied Optics*, 32(4):559–568, 1993.

[83] S.A. Prahl. Inverse adding-doubling, 2007. `https://omlc.org/software/iad/`. Accessed: 04-07-2017.

[84] W. Heller. Remarks on refractive index mixture rules. *J. Phys. Chem.*, 69(4):1123–1129, 2012.

[85] R. Michels, F. Foschum and A. Kienle. Optical properties of fat emulsions. *Optics Express*, 16(8):5907–5925, 2008.

[86] H. Azhari. *Basics of Biomedical Ultrasound for Engineers*. 2010.

[87] K.K. Shung. *Diagnostic Ultrasound*. 2nd edition edition, 2015.

Appendices

A | Appendix A: Acoustic properties of breast tissue

Table A.1: Acoustic properties of breast tissue

Source	**Tissue type**	**Speed of Sound [m/s]**	**Acoustic Attenuation [dB/cm]**	**Density $[kg/m^3]$**	**Backscat. Coef. $[Sr^{-1}cm^{-1}]$**
Duck (1990) [26]	Skin Skin breast/foot Fat Blood	 1420 1584	9.2 ± 2.2@$5MHz$ 4.5@$2.9MHz$		
Moran (1995) [27]	Skin (epidermis) Skin (dermis)	1645 1595	$\alpha = 0.44 \pm 0.26$ $n = 1.55 \pm 0.12$ $\alpha = 0.264 \pm 0.17$ $n = 1.69 \pm 0.084$		$\mu = (5.01 \pm 25.76) * 10^{-8}$ $n = 3.77 \pm 1.5$ $\mu = (1.79 \pm 19.5 * 10^{-6}$ $n = 2.76 \pm 1.4$
Weichenthal (2001) [28] (ref Escoffier (1986) [29])	Skin breast	1642			
Weichenthal(2001) [28]	Skin	1580			
Sun Yongchen (1986) [30]	Fat	1436			0.911
Greenleaf (1981) [31]	Fat	1400-1450			
Li (2009) [32]	Fat Parenchyma	1422 ± 9 1487 ± 21			
Nasief (2016) [33]	Fat		$\alpha = 1.28$ $n = 0.73 \pm 0.23$@$7MHz$		$\mu = (0.6 \pm 0.25) * 10^{-4}$ $n = 2.49$
Rajagopalan [34]	Fat Parenchyma	1480.7 ± 2.5 1539.4 ± 4.5			
Scherzinger (1989) [35]	Fat Parenchyma	1451 ± 36 1549 ± 28	-1.5 ± 1.0 2.7 ± 1.1		
Wiskin (2012) [36] (ref Wiskin (2011) [37])	Fat	1430-1460			

textbfSource	**Tissue type**	**Speed of Sound [m/s]**	**Acoustic Attenuation [dB/cm]**	**Density $[kg/m^3]$**	**Backscat. Coef. $[Sr^{-1}cm^{-1}]$**
Wiskin(2012) [36]	Fat	1400-1411			
	Fat	1443			
	Fat	1473			
	Ductal tissue	1556			
	Fibroglandular	1520			
Anderson (2001) [38]	Fat				$2.59 * 10^{-3}$@$7.2MHz$ $n = 3.49$
	Fibroglandular				$7.08 * 10^{-3}$@$10.3MHz$ $n = 3.43$
					$78.9 * 10^{-3}$@$7.2MHz$ $n = 2.28$
					$146 * 10^{-3}$@$10.3MHz$ $n = 3.25$
Azhari (2010) [86]	1575	0.15	1.055		
Goss (1986)	1586				
Szabo [21]	1584	0.14	1060		
Shung [87]				10^{-5}	
Lou (2017) [20]	Skin	1650		1.150	
	Fat	1470		0.937	
(ref Szabo [21])	Fibroglandular	1515		1.040	
Vogt(2016) [24] (ref Duck (1990) [26]), Edmonds (1991) [39])	Fat	1430-1480	1-18 @1-10 MHz		
	Parenchyma	1460-1520	2-25 @1-10 MHz		
	Blood	1560	0.1-0.2 @ 1-10 MHz		

APPENDIX A. APPENDIX A: ACOUSTIC PROPERTIES OF BREAST TISSUE

B | Appendix B: Optical properties of breast tissue

Table B.1: Optical properties of breast tissue

Source	**Tissue type**	μ_a $[cm^{-1}]$	μ_s' $[cm^{-1}]$	**g**	**n**	**Wavelength [nm]**
Sandell (2011) [43]	Skin	0.16-0.23	6.80-9.84			800
Jacques (2013), eq. 1 [44]	Skin		24.23			
	Glandular		12.25			785
	Adipose		8.38			
	Blood		16.3			785
Jacques (2013), eq. 2 [44]	Skin		24.23			
	Glandular		11.88			785
	Adipose		8.17			
Peters (1990) [45]	Adipose	0.75 ± 0.08	7.9 ± 1.1			900
	Glandular	0.62 ± 0.05	9.9 ± 2.0			
	Adipose	0.70 ± 0.08	8.6 ± 1.3			700
	Glandular	0.47 ± 0.11	14.2 ± 3.0			
	Adipose			0.98		850
	Glandular			0.965		
Brooksby (2004) [46]	Adipose	0.03	9.3			785
	Glandular	0.06	11.2			785
Lister [?]	Blood				1.37	
Lou (2017) [20]	Skin	0.08	5	0.99	1.40	760
	Fat	0.05	8	0.95	1.40	
	Fibroglandular	0.04	6.65	0.95	1.40	
	Blood	9	4.5	0.975	1.38	
Vogt(2016) [24]	Fat	0.05-0.3	3-8			600-900
	Parenchyma	0.1-0.3	5-15			
	Blood	2-10	10-15			

C | Appendix C: Commercial PVCP protocol

The materials needed for fabricating commercial PVCP are as follows:

- Glass beaker
- Vacuum system (figure C.1)
- Au-bain-marie heating system (figure C.2)
- PVCP firm or soft (LureFactors)
- Glass beads (Sigma-Aldrich)
- Magnetic plate (IKA RCT Standard)
- Magnetic stirrer

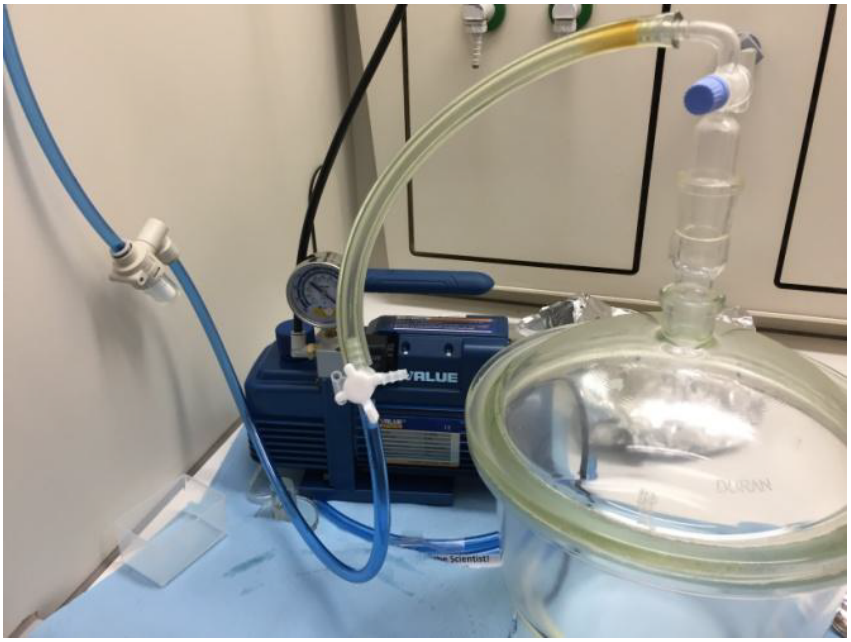

Figure C.1: The vacuum system that was purchased, installed and tested.

The detailed protocol for preparing commercial PVCP is as follows:

1. Preheat heating system.
2. Shake the PVCP bottle well and pour the needed volume in a glass beaker.
3. Weigh off the desired amount of glass beads and add to volume.
4. Stir the mixture for 5 minutes using a magnetic stirrer on a magnetic plate.
5. Submerge the PVCP in the oil once it has reached 160 °C.

6. Cover the beaker with aluminium foil and stir regularly.

7. Determine the volume that is desired to make: this volume is named V

8. Prepare the mixture of liquid components:

9. PVCP undergoes a first transition after about 5-10 minutes, in which it goes from a opaque liquid fluid to a translucent gel-like structure.

10. PVCP undergoes a second transition after another 5-10 minutes, in which it goes from the translucent gel-like structure to a translucent viscous fluid.

11. When the second transition has finished, take off the spatula and place the beaker in vacuum dessicator to degas.

12. After about 5-10 minutes the vacuum pump is switched off and the PVCP is re-heated. It is covered with aluminium foil again, but not stirred.

13. By gently checking the PVCP surface with a spatula, it is determined when the PVCP is hot enough to be poured into the moulds. This is the case after a few minutes, the PVCP is taken from the oil and poured into the mould(s).

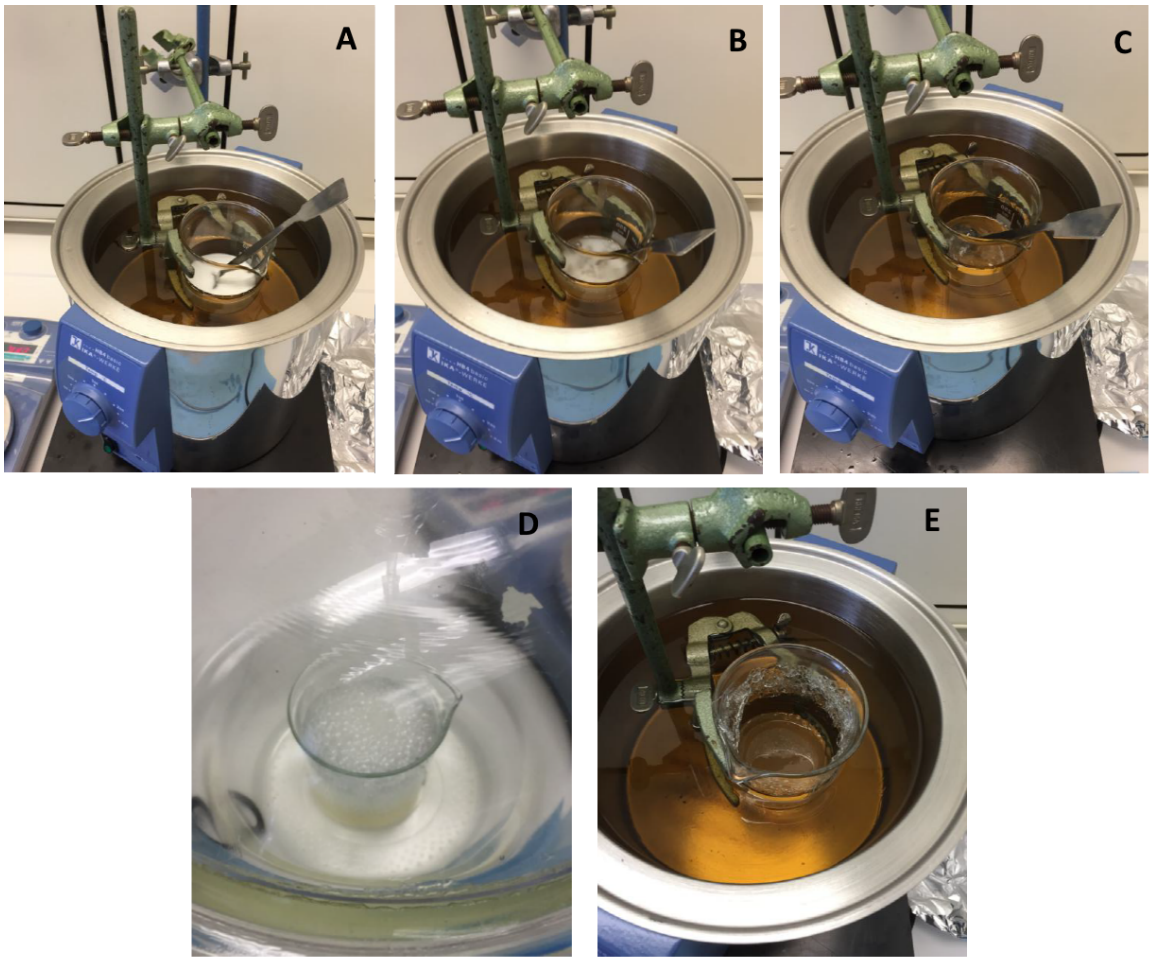

Figure C.2: Different steps during the PVCP fabrication process. (A) Liquid and cold PVCP is submerged in oil, (B) PVCP undergoes first transition, (C) PVCP undergoes second transition, (D) PVCP is degassed and (E) PVCP is reheated before it is poured into the mould.

D | Appendix D: Custom PVCP protocol

The materials needed for fabricating PVCP are as follows:

- Magnetic plate (IKA RCT Standard)
- Magnetic stirrer
- Glass beakers
- Vacuum system
- Au-bain-marie heating system)
- p_1% v/v DEHA (Sigma-Aldrich). This percentage is named p_1.
- p_2% v/v BBP (Sigma-Aldrich). This percentage is named p_2.
- 1% v/v calcium-zinc heat stabilizer (M-F Manufacturing
- p_3 % m/m PVC resin (Geon 121A). This percentage is named p_3.
- c_1 mg/mL glass beads (Sigma-Aldrich). This concentration is named c_1.
- c_2 mg/mL TiO_2 (Sigma-Aldrich). This concentration is named c_2.
- p_4% v/v Black Plastic Colouring (BPC, LureParts). This percentage is named p_4.

The detailed protocol for preparing custom PVCP is as follows:

1. Determine the volume that is desired to make: this volume is named V
2. Prepare the mixture of liquid components:
    a) Weigh empty glass beaker which is sufficiently large (600 mL glass for $V < 300$, 1000 mL glass for $V > 300$). The weight is ..... g
    b) Measure $\frac{0.99}{100} p_1 V =$ ..... mL DEHA in measuring cylinder and pour into glass beaker.
    c) Measure $\frac{0.99}{100} p_2 V =$ ..... mL BBP in measuring cylinder and pour into glass beaker.
    d) Add $0.01V =$ ..... mL heat stabilizer to this using a pipet
    e) Weigh filled glass beaker: ..... g. The mass of the mixture, $m_mix =$ .....g
    f) Calculate the amount of PVC resin to be added: $\frac{p3}{100-p3} m_{mix}$
    g) Weigh off this PVC resin amount in a second glass beaker.
    h) Stir plasticizer mix together and pour about half on resin while stirring.

i) Mix this together until it is quite a homogeneous mixture. Then pour the resin-plasticizer mix back into the remaining plasticizer mix.

j) Again mix this together until the mixture is quite homogeneous.

3. The solution is further mixed and degassed:

   a) Place the magnetic stirrer inside the solution, place the glass beaker on the magnetic plate and stir for 30 minutes at 500 rpm: ..:.. - ..:..

   b) Place the solution inside the dessicator and degas for 60 minutes: ..:..-..:.. Be aware that the solution does not overflow.

4. The additives are added:

   a) Pour 50 mL of the solution in a new glass beaker. Weigh off $0.001c_2V =$ ..... g TiO_2 and add to this small volume.

   b) Stir this mixture for 10 minutes at 500 rpm on magnetic plate: ..:..-..:..

   c) Pour the small volume back into the large stock volume and stir for another 5 minutes at 500 rpm on magnetic plate: ..:..-..:..

   d) Weigh off $0.001c_1V =$ ..... g glass beads and add to mixture.

   e) Stir the mixture for 5 minutes at 500 rpm on magnetic plate: ..:..-..:..

   f) Add $\frac{p_4}{100}V =$ ..... mL BPC to the mixture using a pipet.

   g) Stir the mixture for 5 minutes at 500 rpm on magnetic plate: ..:..-..:..

   h) Take magnetic stirrer off.

5. The PVCP is heated:

   a) Preheat oil in au-bain-marie system 10 minutes before finishing step 4.

   b) Submerge PVCP in oil when it has reached at least 160 $°C$. Cover the glass beaker with aluminium foil and stir regularly using a spatula.

   c) PVCP undergoes a first transition after about 5-10 minutes, in which it goes from a opaque liquid fluid to a translucent gel-like structure.

   d) PVCP undergoes a second transition after another 5-10 minutes, in which it goes from the translucent gel-like structure to a translucent viscous fluid.

   e) When the second transition has finished, take off the spatula and place the beaker in vacuum dessicator to degas.

   f) After about 5-10 minutes the vacuum pump is switched off and the PVCP is reheated. It is covered with aluminium foil again, but not stirred.

   g) By gently checking the PVCP surface with a spatula, it is determined when the PVCP is hot enough to be poured into the moulds. This is the case after a few minutes, the PVCP is taken from the oil and poured into the mould(s).

E | Appendix E: IAD programme

The IAD programme converts an .rxt file with the measured total diffuse reflectance and transmittance to a .txt file consisting of the estimated optical parameters. Within the .rxt file characteristics of the measurements are defined by the list below. The details in this list are from our own performed measurements. The sample properties should be altered depending on the measured sample.

IAD1 # Must be first four characters

Basic test of two measurement functionality
These are accurate values for total reflectance transmittance
for a sample between glass sides for g=0 and various mus and mua

1.485 # Index of refraction of the sample
1.50 # Index of refraction of the top and bottom slides
0.8 # [mm] Thickness of sample
1.0 # [mm] Thickness of slides
3 # [mm] Diameter of illumination beam
0.98 # Reflectivity of the reflectance calibration standard

1 # Number of spheres used during each measurement

Properties of sphere
60 # [mm] Sphere Diameter (8 in * 25.4 mm/in)
16 #[mm] Sample Port Diameter
16 # [mm] Entrance Port Diameter
2.00 # [mm] Detector Port Diameter
0.98 # Reflectivity of the sphere wall

Properties of sphere (unused)
60 # [mm] Sphere Diameter (8 in * 25.4 mm/in)
16 # [mm] Sample Port Diameter
16 # [mm] Entrance Port Diameter
2.00 # [mm] Detector Port Diameter
0.98 # Reflectivity of the sphere wall

2 # Number of measurements, M_R, M_T

F | Appendix F: Silicon skin protocol

The materials needed for fabricating silicon skin are:

- Mixing beakers
- Spatula
- 90 % m/m silicon component A
- 9 % m/m silicon component B
- % m/m thickener
- % m/m orange pigment paste
- % m/m white pigment paste

The detailed protocol for preparing silicon skin is as follows:

1. Determine the total amount that is desired to make.
2. Weigh off ..... g of component A in mixing beaker and stir.
3. Weigh off ..... g of component B in the same mixing beaker and stir again.
4. Add ..... g of thickener to this and stir again.
5. Weigh off ..... g of orange pigment paste in the second mixing beaker.
6. Weigh off ..... g of white pigment paste in the second mixing beaker.
7. Add the silicon mixture to the pigment pastes and stir well for 3 minutes.
8. Silicon is ready to be applied on the desired surface.